Variational approach to solving the phonon Boltzmann transport equation for analyzing nanoscale thermal transport experiments

by

Vazrik Chiloyan

Submitted to the Department of Mechanical Engineering

in partial fulfillment of the requirements for the degree of

Doctor of Philosophy in Mechanical Engineering

at the

MASSACHUSETTS INSTITUTE OF TECHNOLOGY

February 2018

Author ..... Signature redacted .....

Department of Mechanical Engineering

January 15, 2018

Certified by ..... Signature redacted .....

Gang Chen

Carl Richard Soderberg Professor of Power Engineering

Thesis Supervisor

Accepted by ..... Signature redacted .....

Rohan Abeyaratne

Chairman, Department Committee on Graduate Students

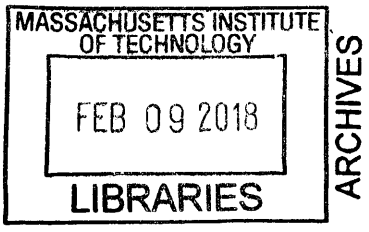

Variational approach to solving the phonon Boltzmann transport equation for analyzing nanoscale thermal transport experiments

by

Vazrik Chiloyan

Submitted to the Department of Mechanical Engineering on January 15, 2018
in partial fulfillment of the requirements for the degree of
Doctor of Philosophy in Mechanical Engineering

Abstract

Over time, technology has shrunk to smaller length scales, and as a result the heat transport in these systems has entered the nanoscale regime. With increasing computational speed and power consumption, there is a need to efficiently dissipate the heat generated for proper thermal management of computer chips. The ability to understand the physics of thermal transport in this regime is critical in order to model, engineer, and improve the performance of materials and devices. In the nanoscale regime, thermal transport is no longer diffusive, and the Fourier heat conduction equation, which we commonly utilize at the macroscale, fails to accurately predict heat flow at the nanoscale. We model the heat flow due to phonons (crystal lattice vibrations), the dominant heat carriers in semiconductors and dielectrics, by solving the Boltzmann transport equation (BTE) to develop an understanding of nondiffusive thermal transport and its dependence on the system geometry and material properties, such as the phonon mean free path.

A variety of experimental heat transfer configurations have been established in order to achieve short time scales and small length scales in order to access the nondiffusive heat conduction regime. In this thesis, we develop a variational approach to solving the BTE, appropriate for different experimental configurations, such as transient thermal grating (TTG) and time-domain thermoreflectance (TDTR). We provide an efficient and general methodology

to solving the BTE and gaining insight into the reduction of the effective thermal conductivity in the nondiffusive regime, known as classical size effects.

We also extend the reconstruction procedure, which aims to utilize both modeling efforts as well as experimental measurements to back out the material properties such as phonon mean free path distributions, to provide further insight into the material properties relevant to transport. Furthermore, with the developed methodology, we aim to provide an analysis of experimental geometries with the inclusion of a thermal interface, to provide insight into the role the interface transmissivity plays in thermal transport in the nondiffusive regime. Lastly, we explore a variety of phonon source distributions that are achieved by heating a system, and show the important link between the system geometry and the distribution of phonons initiated by the heating. We show the exciting possibility that under certain nonthermal phonon distributions, it is possible to achieve enhanced thermal transport at the nanoscale, contrary to the current understanding of size effects only leading to reduced thermal conductivities at the nanoscale for thermal phonon distributions.

Thesis Advisor: Gang Chen

Thesis committee:

Gang Chen (Mechanical Engineering)
Department head of Mechanical Engineering, Carl Richard Soderberg Professor of Power Engineering

Nicholas X. Fang (Mechanical Engineering)
d'Arbeloff Career Development Associate Professor of Mechanical Engineering

Keith A. Nelson (Chemistry)
Haslam and Dewey Professor of Chemistry

Dedication

To my beloved family.

Acknowledgements

I have so many people to thank who have helped me along my PhD journey. I want to start by thanking my advisor, Professor Gang Chen, for all of his support throughout my PhD. He has always pushed me to think deeply about research questions, and really tackle problems that can make an impact in the scientific community. If it weren't already clear from this thesis, my approach to science is very mathematical, but Gang would always push me to connect the mathematics with the underlying physics of the transport in order to really improve our understanding of thermal transport in materials. I am grateful for having him to always ground me and push me to focus on the important scientific questions we can answer with the mathematical tools we developed. I would like to thank my committee members, Professor Keith Nelson and Professor Nick Fang. Having the expertise that Keith brought to my committee on thermal transport and spectroscopy was invaluable, and I had the wonderful opportunity to collaborate with him and his group members numerous times in my PhD years. Seeing him present at conferences was always inspiring because the passion he would showcase for the scientific breakthroughs he would present on really demonstrated to me that there are still scientists out there that really believe in the beauty of science and want to share it with others in the world. I am also very grateful to have had Nick in my committee. His deep, thoughtful questions during committee meetings really pushed me to develop a stronger understanding of nanoscale thermal transport. He would always impress me with the clever suggestions he would have even if he were seeing me present on a topic for the first time.

Next I would like to thank the many members of the S3TEC center, which was headed by my advisor Gang. The S3TEC center brought together some of the brightest and friendliest scientists and allowed for wonderful collaborative opportunities. It was through regular phonon spectroscopy S3TEC meetings that I met Keith and many of his students, and opened up the way for collaboration on studying the transient thermal grating experimental geometry. It was through the S3TEC meetings I had the pleasure of meeting Dr. Alex Maznev. Alex served as a true role model for me as a scientist. His ability to understand thermal transport on a theoretical level, yet be a talented experimentalist, was truly impressive. I would often test my ideas against Alex because if he could not find a flaw in it, I knew it had to be a good idea! I had countless meetings with Alex and he really helped me elevate the level of my work and do my best in not

only developing rigorous models, but also to be able to explain my work to as broad of an audience as possible.

I am deeply thankful for my friends and lab mates Samuel Huberman and Dr. Lingping Zeng. Sam is one of the greatest friends one could ask for during the journey of a PhD. We have shared many ups and downs as we worked together to develop an understanding of nanoscale thermal transport, but we always supported and encouraged each other. Many of the projects I developed in the last year of my PhD came out of spontaneous brainstorming we would do, and simple questions that Sam would pose would develop into completely unexpected scientific possibilities. Working with Sam will definitely be the aspect of the PhD I will miss most. I am also grateful to call Lingping both a colleague and a friend. Lingping was in the tail end of his PhD when I had started the PhD work in this thesis, yet he would always offer his time and knowledge to help my projects progress. He helped both Sam and I even when he had critical deadlines to meet to graduate, and when I was first trying to convince others of my variational work, he would always stick by my side and encourage me to keep pushing forward and not to let minor setbacks keep me from pursuing my ideas.

I also want to thank my lab mates who have since graduated but were always encouraging to me: Dr. Ken McEnaney, Dr. Dan Kraemer, Dr. Poetro Sambegoro, Dr. Maria Luckyanova, and Dr. Kimberlee Collins. I am especially indebted to Kim as she got me interested in nanoscale thermal conduction. While she was working on meeting final deadlines to graduate, she still managed to take time to send me relevant papers and ideas she thought that I should pursue. This dedication to helping a younger lab mate like myself was something I truly admired, and even when I found myself buried in work near the end of my PhD, I worked to always help my lab mates when asked because of how I benefitted from Kim. I also want to thank all of my current NanoEngineering lab mates. I have learned a lot from all of the conversations and group meetings I have shared with all of you, and hope that I have been able to pass on some knowledge myself to you all.

I want to thank the MIT Shotokan Karate club for being a wonderful home to me. Practicing and teaching Shotokan Karate throughout my PhD years was how I was able to stay happy and productive even during the toughest times of my research. I have so many wonderful memories with my Karate friends from MIT, BU, Tufts, Wellesley, and from Japan. I especially want to thank my dear friend Anselmo Cassiano Alves. He always reminds me to enjoy the

journey itself, not just the success we seek at the end of it. I have enjoyed each and every moment together, and look forward to what new things we accomplish in the future. I want to thank my friends in the MIT Armenian Society as well. I had the pleasure of being both the president as well as a contributing member of the MIT Armenian society and felt very lucky to be able to share my culture and history with MIT. We spent hours together planning social events, lectures, panel discussions, and really helped make an impact on campus and make our presence known. I will cherish these memories forever. I also want to thank my friends from my undergraduate dorm at MIT, New House 4. Their support and care throughout my PhD years was always greatly appreciated.

I want to thank my friends at Signet Education. Signet has been like a second home to me, and allowed me to tutor math and physics students around the world. Signet gave me the opportunity to share my math and science passion, to empower students, and show them the beauty that exists in the process of learning. To be able to have met such wonderful, dedicated individuals who enjoy helping people believe in the power of education and the joy that comes with learning has been so wonderful. I also want to thank my high school mentors, Ms. Karen Trenholm and Mr. Charles Garabedian. They instilled a passion for math in me, and taught me to never be afraid to ask questions and really aim to develop a deep understanding. It is thanks to them that when I pursue knowledge in research, I am never satisfied till I truly understand the subtleties of the topic.

Last but not least, I want to thank my beloved family: my twin brother Garen, my younger brother Varant, my mother Vartouhie and my father Vartan. Whenever I would get home from a long day, my brothers would have jokes to tell me and help me shake off the difficulties of the day. They have supported me unconditionally, and have always been there whenever I have needed them. I am also eternally grateful for the love and support from my parents. My parents came to the US when I was 4 years old in search of a better life with more opportunities for me and for my brothers. They left behind their family, friends, and everything that was familiar to them to give me the opportunities I have now. They taught me the value of education and to enjoy the beauty of the learning process. Whenever I faced difficulties during my PhD, I would always think of the sacrifice they made to make all of this possible, and find the will to push ahead. It is thanks to them that I am the man that I am today, and I love them with all my heart.

Contents

List of Figures

Chapter 1
Introduction

The Fourier heat conduction equation has been widely utilized to understand and characterize thermal transport in materials at the macroscopic scale. For large scale applications where the typical length scales and typical time scales are much longer than the characteristic mean free path (MFP) and relaxation times of the heat carriers, such as electrons and phonons, the Fourier heat conduction equation is valid. However, with the shrinking size of devices produced by modern technology [1,2], the need to understand beyond the thermal diffusion regime has never been more important.

Beyond developing an understanding, the need to control thermal transport to improve the thermal efficiency of devices is critical. The efficiency of thermoelectric devices [3,4], which convert heat to electricity, directly depends on the thermal conductivity of the material. An effective approach has been to introduce boundaries and to tune the scattering of the heat carriers in order to reduce the thermal conductivity. While there are a variety of heat carriers to consider, such as phonons (lattice vibrations), electrons, magnons, we focus here on the study of thermal transport in dielectric materials [5], in which the thermal transport is dominated by phonons. Grain boundaries [6], for example, have been introduced in order to scatter the phonons, and reduce the thermal conductivity, while keeping the electrical transport unaffected in order to obtain a high thermoelectric efficiency.

The goal of this work is to provide an efficient approach to solving the necessary equations to understand thermal transport by phonons in crystalline materials. This aims to provide insight into the effect of small length scales and short time scales on the thermal conductivity of materials. With this information, we aim to gain insight into the microscopic details of thermal transport and extract the MFPs of phonons in various materials.

1.1 Size effects and the effective thermal conductivity

Size effects have been observed experimentally in various heat transfer configurations. The thermal conductivity in kinetic theory is given by $k = \frac{1}{3}\int C_\omega \mathrm{v}_\omega \Lambda_\omega \, d\omega$, where C_ω is the heat capacity, v_ω is the group velocity, and Λ_ω is the MFP of phonons. When the length scales in an experimental configuration, such as the width of boundaries of the material or the size of the heating region, become comparable to the characteristic MFPs of phonons in a material, phonons with longer MFPs will be scattered at interfaces and boundaries. This yields an effective reduction of the MFP of these phonons, and equivalently a reduction in the thermal conductivity, which serves as a definition of the classical size effects. Size effects can be observed in both diffusive transport, as well as in nondiffusive transport. The characteristic of nondiffusive transport is one where the temperature profile no longer matches the Fourier heat conduction solution with a bulk value of thermal conductivity.

One simple picture that demonstrates the reduction of the thermal conductivity with the decreasing size of the geometry of a system can be given by heat transport between a hot surface and a cold surface, as depicted in Fig. 1-1. In the diffusive limit, phonons undergo many scattering events at their respective MFP Λ between the surfaces. In the ballistic limit, the distance between the surfaces is now smaller than the MFP of the system, so one can consider that the effective MFP of the phonon has been reduced as it will scatter now much earlier than it typically would have, and thus with a decrease in the MFP, the kinetic theory predicts a decrease in the effective thermal conductivity, hence demonstrating size effects.

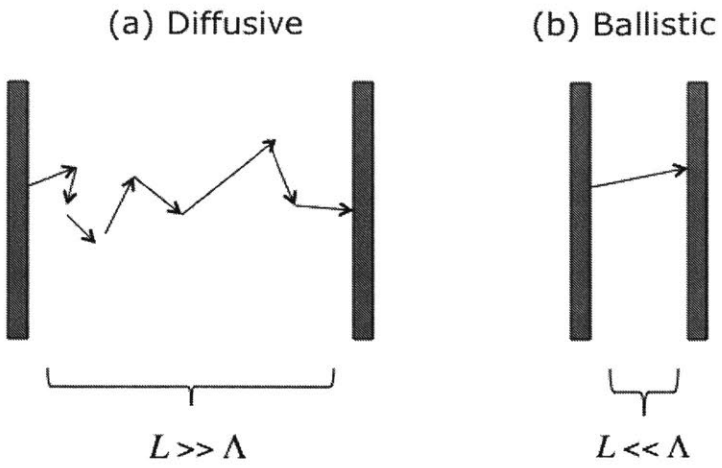

FIG. 1-1. Cross plane thermal transport between a hot and cold surface in the (a) diffusive regime as well as in the (b) ballistic regime.

One of the first observations of size effects was for thermal transport in nanowires and thin films. Studies on the Temperature dependence and also on the length and diameter of the silicon nanowires gave insight into the strong reductions in the thermal conductivity compared to bulk due to the boundary scattering experienced by phonons [7–9]. A variety of studies measured the thermal transport along silicon thin films, demonstrating a large reduction of the thermal conductivity compared to the bulk value of thermal conductivity [10–12]. Figure 1-2 below shows experimental results and predictions for the thermal conductivity of silicon thin films as a function of the film thickness, where the results were reported in Ref. [12]. Studies were also performed to look at the temperature dependence, as the MFP of phonons generally decrease with increasing temperature, and this can be reflected in the thermal conductivity [12,13]. There was a corresponding push on the theoretical side to accurately model thermal transport along these films, which included Monte Carlo (MC) simulations [14], as well as analogies to radiative heat transfer to solve the BTE [5,15]. The literature at this time could only handle solving the gray BTE, one in which the spectrum of MFPs and group velocities of the phonons were neglected and a single averaged value was utilized.

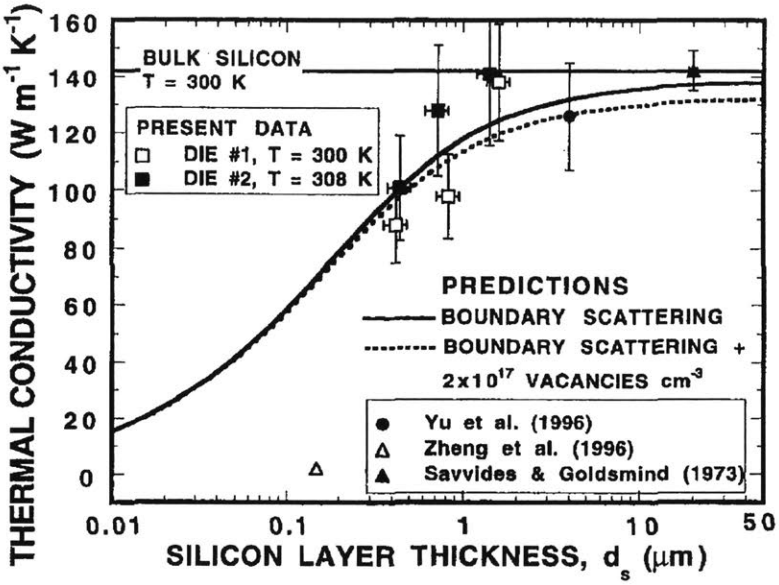

FIG. 1-2. Thermal conductivity of silicon thin films as a function of film thickness. Figure adapted from Ref. [12].

The results of Fig. 1-2 showed the reduction by more than an order of magnitude for the thermal conductivity of silicon thin films when the thickness was reduced to only tens of nanometers.

More recently, table-top experiments have been developed in order to generate length scales that are comparable to the MFPs using heating profile patterns [16] or material thickness [17] in order to observe this reduction in thermal conductivity. One example of experiments involving nondiffusive transport is in the thermal transient grating (TTG) experiment [16–19], in which laser beams are crossed in order to generate a sinusoidal heating profile on a suspended membrane, as shown in Fig. 1-3. Subsequent probe beams are utilized to measure the temperature dynamics of the system. From the thermal decay, the thermal conductivity can be extracted. From experiments on silicon [16] and GaAs [19], nondiffusive transport has been observed, whose signature is given by a thermal conductivity that depends on the grating period.

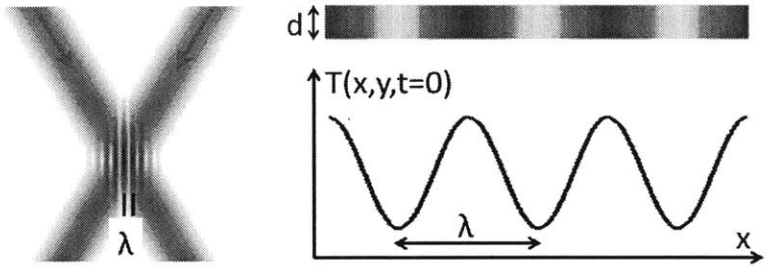

FIG. 1-3. Schematic of thin film TTG experimental configuration. Figure adapted from Ref. [20].

The onset of nondiffusive transport occurs on the order of a few micron for silicon [16]. Figure 1-4 shows the dependence on the thermal decay rate, given by $\gamma = \alpha q^2$, where α is the thermal diffusivity, and $q = 2\pi / \lambda$ is the grating wavevector. Diffusive transport is when the grating period is large, i.e. q is small, and the dependence of the thermal decay rate is linear with the square of the grating wavevector. In this regime, the slope is given by the thermal diffusivity. However, for smaller grating periods, the system deviates from linear behavior, demonstrating that the thermal diffusivity now has length dependence and the transport is in the nondiffusive regime.

FIG. 1-4. Experimental measurement of the thermal decay rate of silicon, showing the dependence upon the square of the grating wavevector. Figure adapted from Ref. [16].

The development of picosecond thermoreflectance measurements provided the nanoscale thermal transport community with the ability to resolve thermal transport on the nanoscale. The configuration of this system made it more suitable for measuring cross plane transport, while the TTG provided sensitivity to in-plane transport. The thermal diffusion length, given by $L \sim \sqrt{\alpha t}$, and with $t \sim 100\,\text{ps}$ and a thermal diffusivity of many materials being on the order of $\alpha \sim 10^{-6} - 10^{-5}\,\text{m}^2/\text{s}$, yields diffusion lengths on the order of tens to hundreds of nanometers. A thin metal film is deposited on top of a substrate and serves as an absorber of optical light. A pump laser beam, used to heat the system, and a probe laser beam, used to detect the changes in reflectivity of the metal surface, are used to detect changes in the system and extract the temperature response based on a model of the temperature dependence of the reflectivity of the metal [21,22]. Time-domain thermoreflectance (TDTR) was first utilized to measure the thermal conductivity of glass [21]. Around this time it was also utilized to measure the thermal conductivity of thin metal films deposited on top of substrates without any complications of the coupled transport from the substrate, thus providing a method to measure the metal conductivity directly [23].

More recently, the time-domain thermoreflectance (TDTR) [24–29] and frequency-domain thermoreflectance (FDTR) [30,31] have been utilized extensively in order to probe and observe nondiffusive transport by using ultrafast time scales or ultrashort length scales and gain key insight into the material's MFP spectrum. In particular, modulation frequency dependence of the thermal conductivity was observed with the FDTR [32] for certain materials like SiGe. Size effects from the beam spot were observed for silicon [33], and nanostructured patterns such as line heaters and nanodots were fabricated to be able to push the length scales of the geometry to even smaller lengths to probe strongly nondiffusive transport [27,29].

The Boltzmann Transport Equation (BTE) models thermal transport due to phonons in systems for which the length scales of the given geometry can become comparable to the characteristic MFP values of the material. It does not capture coherent transport, in which the wave nature of phonons becomes important, and so will capture transport in which the scattering of phonons makes them lose their phase information and the phonons can be modeled as bundles of energy with a particular group velocity and MFP [34]. At room temperature, thermal transport is incoherent and the BTE performs well in capturing the details for transport for many dielectric materials such as silicon, SiGe. Being able to accurately and efficiently solve the BTE

is critical to gaining an understanding of nondiffusive thermal transport and modeling the relevant experimental geometry. In many situations, the end goal of solving the BTE is to obtain the dependence of the experimental observable, such as the thermal decay rate in the TTG set up, as a function of the material properties. Furthermore, this yields the effective thermal conductivity of the system as a function of its intrinsic material properties and geometry of the system. The thermal conductivity accumulation function has been utilized as an elegant metric for understanding which MFP phonons contribute predominantly to thermal transport in a material [6,35,36]. Recently, algorithms were developed in order to reconstruct the MFP distribution [29,37]. This provides the ability to reconstruct the material properties from experimental measurements.

When the length scales in a system become comparable to the MFPs in a material, the effective thermal conductivity is reduced compared to its bulk, diffusive limit value [38,39], and thermal conductivity in the nondiffusive regime is given by $k = \frac{1}{3}\int C_\omega \mathrm{v}_\omega \Lambda_\omega S_\omega \, d\omega$, where $S_\omega = S(\Lambda_\omega / L)$ is the suppression function used to quantify this reduction or suppression of thermal conductivity, which is assumed to depend on the MFP to length scale ratio, where the length scale can be the film thickness, the grating period in a TTG measurement, the beam spot size in a TDTR measurement, etc. The variables C_ω, v_ω, Λ_ω are the volumetric spectral heat capacity, the group velocity, and the MFP, respectively. The suppression function provides the ability to extend the notion of thermal conductivity beyond the diffusive regime in which it is defined from Fourier's law [37,38]. By measuring the thermal conductivity at various lengths for the grating in TTG, and having solved the BTE to obtain the suppression function for the given geometry, the reconstruction process extracts the accumulated thermal conductivity. Figure 1-5 shows the accumulated thermal conductivity that is obtained from numerical data from Monte Carlo simulations, as well as the properties obtained from the reconstruction process, to demonstrate the accuracy and sensitivity of the approach [37].

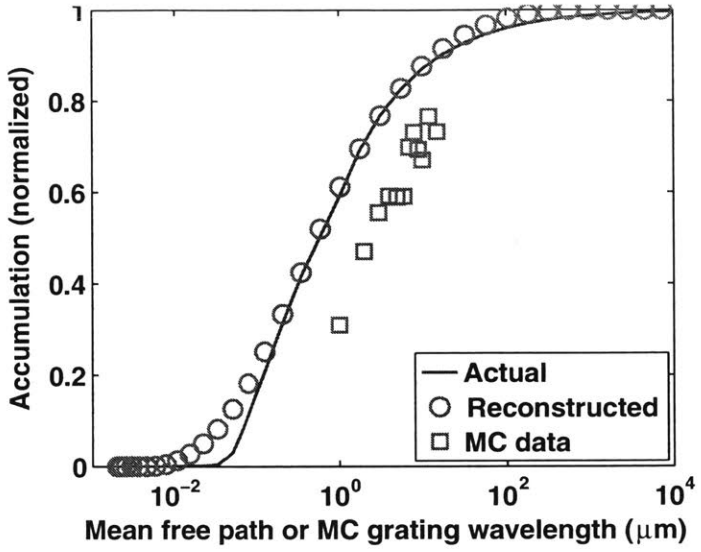

FIG. 1-5. Reconstructed thermal conductivity accumulation function. Figure adapted from Ref. [37].

With the combination of experimental measurements of nondiffusive transport, as well as accurate modeling of the heat transfer configuration with the BTE, the nondiffusive transport data can be successfully used to extract the MFP distribution of materials. Typically, density functional theory (DFT) is utilized to extract the material properties of heat capacity, group velocity, and the MFP spectrum[40,41]. However, DFT is computationally limited to single crystalline structures, and this limits the broad set of materials of interest to thermal engineers. With the reconstruction procedure, the material properties can be obtained through the use of experiments and are useful for understanding thermal transport[6].

1.2 A variational approach to solving and understanding nondiffusive transport

The BTE is notoriously difficult to solve. Given the large phase space of the spatial and temporal variables, as well as the spectral properties of the phonons, efficient numerical solutions of the BTE are difficult to develop. Solutions to the BTE have been developed for simple geometries [42,43], or under the simplification of a single MFP in the gray BTE [39,44]. Numerical techniques for the direct solution of the BTE or via Monte Carlo simulation have been developed [18,20,26,44–51], but they are difficult to apply to existing experimental geometries and can be computationally expensive. More specifically, solutions to the spectral BTE, which considers the wide range of MFPs and the spectrum of properties for phonons, were solved using the Fourier transform as well as finite difference techniques [47,48,52,53]. By solving the BTE with appropriate boundary conditions and initial conditions for the TTG configuration, an integral equation was obtained for the temperature profile, which was solved numerically. On the other hand, rather than a finite difference numerical solution to the BTE, efficient Monte Carlo simulations have been successful at accurately simulating heat transport in these experimental geometries [20,26,27,54,55]. By simulating deviational phonons, i.e. phonons that represent the energy above the reference background, this significantly reduced the computational cost of simulating large spatial domains, and made MC simulations a tractable approach to studying thermal transport [50,51].

The limitation with such numerical approaches to studying thermal transfer is that while it provides numerical curves for the temperature output as a function of say the grating period in the TTG, it does not provide a functional form to understand how the material properties affect the thermal transport. In this work, we have developed a method to solve the BTE which yields accurate, analytical solutions to the BTE, by using a trial solution supplied by the Fourier heat conduction solution and utilizing the variational approach to optimize this trial solution. The BTE has been solved using the variational principle previously [34], but this has been at the scale of the BTE itself. The novelty of our new approach is that we solve the BTE to yield the temperature equation, accurate in the nondiffusive range, and the variational approach is applied

at this scale in order to utilize the solution from the Fourier temperature field. While the variational temperature profile utilized could be the result from the ballistic limit, as we aim to understand the nondiffusive transport observed in experiments, we utilize the Fourier temperature field with the thermal conductivity as the variational parameter.

The BTE under the relaxation time approximation (RTA) in terms of the nonequilibrium phonon energy density is given by [5,52,56]:

$$\frac{\partial g_\omega}{\partial t} + \vec{\mathrm{v}}_\omega \cdot \vec{\nabla} g_\omega = \frac{1}{\tau_\omega}\left[\frac{C_\omega}{4\pi}\Delta T - g_\omega\right] + Q_\omega \tag{1.1}$$

In Eq. (1.1), g_ω is the phonon energy density per unit frequency interval per unit solid angle above the equilibrium spectral energy density at background temperature T_0, related to the phonon distribution function f_ω and density of states $D(\omega)$ as $g_\omega = \frac{\hbar\omega D(\omega)}{4\pi}\left(f_\omega - f_0(T_0)\right)$. $\vec{\mathrm{v}}_\omega$ is the group velocity and τ_ω is the relaxation time. The form of the BTE of Eq. (1.1) is in the linear response regime where we assume the temperature rise due to the heating is small compared to the background room temperature. The spectral heat capacity is given by $C_\omega = \hbar\omega D(\omega)\frac{df_0}{dT_0}$, and the equilibrium distribution is given by Bose-Einstein statistics as $f_0(T_0) = \frac{1}{\exp\left(\frac{\hbar\omega}{k_B T_0}\right) - 1}$. We utilize the subscript ω as a short hand notation to denote a phonon of a given branch and frequency. The spectral volumetric heat generation term can be written as $Q_\omega = p_\omega Q$, where Q is the macroscopic volumetric heat generation rate, and p_ω represents the degree to which a phonon mode is excited by the heating. These values are normalized such that the sum over the branches and phonon frequencies add up to unity, i.e. $\int d\omega p_\omega = 1$. The spatial distribution of Q_ω is given by the macroscopic heat generation rate Q, while p_ω only depends on the physics of the heating process.

The energy density of the system U can be obtained by summing the nonequilibrium phonon energy distribution over the solid angle and the phonon dispersion, given as $U = \int d\omega \int d\Omega g_\omega$ and the heat flux $\boldsymbol{q}$ similarly by summing over the phonon energy distribution multiplied by the

phonon group velocity, given as $\vec{q} = \int d\omega \int d\Omega g_\omega \vec{v}_\omega$. The RTA is an approximation to the scattering of phonons with phonons. While more recently, there have been developments to more complex scattering kernels that can capture the scattering for materials for which the RTA is a poor approximation [57–60], the RTA has been shown to be accurate for silicon near room temperature [61–63].

By summing the BTE of Eq. (1.1) over all phonon modes, we obtain:

$$\frac{\partial U}{\partial t} + \vec{\nabla} \cdot \vec{q} = \int d\omega \int d\Omega \frac{1}{\tau_\omega} \left[\frac{C_\omega}{4\pi} \Delta T - g_\omega \right] + Q \tag{1.2}$$

Thus the energy conservation equation is recovered if the following relationship is enforced between the temperature and nonequilibrium phonon energy distribution:

$$\int d\omega \int d\Omega \frac{1}{\tau_\omega} \left[\frac{C_\omega}{4\pi} \Delta T - g_\omega \right] = 0 \tag{1.3}$$

Equation (1.3) is how we obtain a temperature integral equation, as the nonequilibrium phonon energy distribution g_ω is a functional of the temperature, and depends on the temperature in a nonlocal way. Solving the BTE of Eq. (1.1) requires the ability to solve the partial differential equation as a function of the material properties and as a function of the input heating and temperature response, and applying scattering boundary conditions at surfaces in the system. The ability to obtain an analytical solution for the energy distribution function is difficult, limited to regular geometries. From there though, very few analytical solutions exist of the integral equation itself, limited to only diffusive in-plane transport in a thin film [5,17,42,43].

Traditionally, the BTE has been solved numerically, and then the temperature decay is fitted to the solution from the Fourier conduction equation in order to extract an effective thermal conductivity [48,52]. Knowing the solution to the BTE in the diffusive limit, thanks to the solution to the Fourier heat conduction equation, means that we have more information about the transport in the system and need not solve the integral equation given by Eq. (1.3) in such a brute force approach. Rather than directly solving the BTE, we utilize the solution to the Fourier equation as a trial function, and use the variational technique to optimize this solution. This reduces the two-step process of doing an exact numerical solution and then fitting to the Fourier solution into a single one, where we immediately utilize the Fourier trial function and optimize it to extract the effective thermal conductivity. This has been shown to yield highly accurate

solutions to the BTE analytically [64,65]. By obtaining analytical formulas for the effective conductivity in various geometries, this allows for a deeper insight into the material properties that affect transport, and to more accurately generate algorithms that can reconstruct the material properties given experimental measurements which extract the effective thermal conductivity.

The variational approach utilized here for the BTE is analogous to the variational method in quantum mechanics, used for improving one's trial solution for the ground state energy of a given system [66,67]. The variational principle has been applied to the BTE previously in calculating the cross plane heat flux in a thin film [68]. Allen [68] utilized a specific error metric, one that tries to best enforce uniform heat flux through the slab to ensure energy conservation, to approximately calculate the thermal flux between a hot wall and cold wall. Furthermore, variational techniques have been applied to solving the BTE at the initial stage of the partial differential equation itself [69,70]. In this approach, first described by Ziman [34], the partial differential equation for the phonon distribution function is solved utilizing the variational principle, and the variational parameter is calculated by optimizing the entropy. In this work, we develop the application of the variational principle upon the integral equation for the temperature profile, derived from the BTE, and solve for the variational parameter by minimizing the residual error in the equation. Although we anticipate that this approach can be applied also directly to the BTE, the technique developed here is applied at the stage of the temperature equation for two reasons. One being that analytically solving the BTE up to the temperature equation decreases inaccuracies that can build up from utilizing approximations earlier on in the solution. Second, the temperature equation allows for the direct utilization of the Fourier heat conduction solution as the trial function, with the effective thermal conductivity (or other properties such as interfacial resistance or boundary temperature slip) as the parameters used to minimize the error of the variational trial function. Thus this methodology offers an efficient, approximate approach to solving the BTE to study nanoscale thermal transport.

1.3 Organization of thesis

The organization of this thesis is as follows: in Chapter 2 we formally introduce the variational approach to solving the BTE for analyzing nondiffusive thermal transport, and apply it to the TTG experimental configuration in the one-dimensional limit as a simple example to demonstrate the details of the variational approach. In Chapter 3, we apply the variational approach to the full experimental TTG geometry, both in transmission mode as well as reflection mode to be able to offer the opportunity to study both optically transmissive as well as opaque materials. In Chapter 4, we utilize the understanding gained from solving the forward problem of outputting temperature distributions given material properties, to be able to generate a new attack on the inverse problem of extracting the material properties from experimental measurements. In chapter 5, we use the variational approach to study the TDTR / FDTR geometry as the study of nondiffusive transport would not be complete without an understanding of thermal transport across interfaces. In Chapter 6, we explore the effect of the phonon source distribution on size effects to demonstrate that systems in which the heating excites a thermal distribution of phonons can behave very differently in the nondiffusive regime compared to systems where the heating excites phonons with distributions that are nonthermal extremes. In Chapter 7, we provide some major conclusions of this work and future steps to take to extend our understanding of thermal transfer in the nondiffusive regime further with this developed formalism.

Chapter 2

Variational approach to solving the BTE

In this chapter, we elaborate on a new universal variational approach to solving the BTE introduced in the previous chapter. This variational approach enables extraction of phonon mean free path (MFP) distributions from experiments exploring nondiffusive transport by providing insight into the way material properties and the system geometry affect the effective thermal conductivity. By utilizing the known Fourier heat conduction solution as a trial function for the temperature from the BTE, we present a direct approach to calculating the effective thermal conductivity from the BTE. We demonstrate this technique on the transient thermal grating (TTG) experiment, which is a useful tool for studying nondiffusive thermal transport and probing the mean free path (MFP) distribution of materials. In this chapter we focus on the one-dimensional limit of the TTG to illustrate the approach in detail without the complications of boundary scattering, before moving on to applying the variational approach to the full TTG configuration in Chapter 3.

2.1 The suppression function and its limitations

By utilizing the suppression function for a given experimental geometry, one can obtain the material's phonon MFP distribution from the experimentally measured thermal conductivity through MFP reconstruction [17,27,29,37]. To obtain the effective thermal conductivity, the thermal signal from the experiment is fitted to the results of Fourier's law. The suppression function is calculated through modeling of the given experimental geometry with the BTE. However, one key assumption in this method is the universality of the suppression function, i.e. the ability to express the suppression function as $S = S(\Lambda_\omega / L)$ so that it depends only on the ratio of MFP to a characteristic length for a given experimental configuration, but not otherwise on the material properties. This assumption allows one to obtain effective thermal conductivities

by solving for the suppression function from the gray BTE, i.e. the BTE equation with a single MFP [52]. This assumption has been shown to be not strictly valid in the past [48,52] and will be further shown in this chapter.

The BTE is notoriously difficult to solve, especially for complex geometries, which presents difficulty in calculating the effective thermal conductivity of materials in a given experimental geometry. So far almost exclusively, numerical solutions are implemented that directly attempt to solve the BTE, and are then fitted to the Fourier heat conduction solution to extract the effective thermal conductivity and corresponding suppression function for the experimental geometry. Experimental methods have also been utilized that rely on first-principles material property data to obtain a calibrated suppression function [27]. The key insight in our work here is to utilize the temperature distribution obtained from the Fourier heat conduction equation directly in the BTE for the given experimental geometry to facilitate, hence significantly simplify, its solution. Furthermore, we develop a variational approach to yield solutions to the spectral BTE, thus the work here is not limited by any approximations on the dependence of a phonon's velocity and MFP on its frequency. By utilizing the temperature field derived from the Fourier heat conduction equation and the variational method, we obtain solutions that are both simple yet can reproduce the exact numerical results from the BTE in terms of obtaining the effective thermal conductivity. Our approach provides a more direct, universal methodology for extracting the effective thermal conductivity and corresponding suppression function to enable the extraction of intrinsic material properties such as the phonon MFP distribution from nondiffusive experiments.

We begin with a model problem of the one-dimensional TTG experimental geometry as an example to demonstrate the variational process formally. In the TTG experiment, two laser beams are crossed in order to generate a sinusoidal heating profile on a sample, with a spatial periodicity of length λ. Once heated, the sample is allowed to relax and the thermal decay profile is measured to yield information about the transport within the material. At grating periods on the order of micrometers, nondiffusive transport has been observed [16,18,19]. Given the success of this experiment in probing nondiffusive transport and the opportunity to yield MFP data using reconstruction techniques that have been developed [37], the ability to model this experiment is critical. Furthermore, the relative simplicity of the geometry makes it more accessible for theoretical modeling.

The TTG in the one-dimensional case has been previously studied in a two-fluid framework, and with simplifying assumptions about the scattering of high and low frequency phonons, an analytical suppression function has been calculated [18] and utilized in MFP reconstruction [37], but there is a concern that this model is only valid at the onset of nondiffusive transport. Collins *et al.* solved the problem with a numerical approach to obtain the exact solution both in the gray case as well as the full spectral case for the BTE for Si and PbSe [52]. Deviation of the two-fluid model from the exact numerical solution was shown for PbSe [52]. Hua and Minnich obtained the Fourier transform of the thermal decay analytically, and were able to recover the two-fluid model suppression function in the weakly nondiffusive limit [48]. However, there is no closed form expression for the thermal decay rate γ and the suppression function S that matches numerical results.

Utilizing the notation by Collins *et al.*, we begin with the spectral BTE in one dimension under the relaxation time approximation [52] :

$$\frac{\partial g_\omega}{\partial t} + \mu \mathrm{v}_\omega \frac{\partial g_\omega}{\partial x} = \frac{g_0 - g_\omega}{\tau_\omega} \tag{2.1}$$

where g_ω is the phonon energy density per unit frequency interval per unit solid angle above the reference background energy, related to the distribution function and density of states as $g_\omega = \frac{\hbar\omega D(\omega)}{4\pi}\left(f_\omega - f_0(T_0)\right)$. μ is the direction cosine, v_ω is the group velocity, τ_ω is the relaxation time, and g_0 is the equilibrium energy density, given by $g_0 \approx \frac{1}{4\pi} C_\omega (T - T_0)$ in the linear response regime, where the spectral heat capacity is given by $C_\omega = \hbar\omega D(\omega)\frac{df_0}{dT_0}$, and the equilibrium distribution is given by Bose-Einstein statistics as: $f_0(T_0) = \left[\exp\left(\frac{\hbar\omega}{k_B T}\right) - 1\right]^{-1}$.

The linear response regime assumes that heating in the material is small enough so that the temperature rise is small compared to the background room temperature, i.e. $|T - T_0| << T_0$, where T_0 is the background room temperature. In the TTG experiment, the temperature initially has a sinusoidal profile and in general obeys $T(x,t) = T_0 + h(t)T_m e^{iqx}$ in complex form where T_m is the initial amplitude of the spatial variation, $q = 2\pi/\lambda$ is the grating wavevector, and $h(t)$ is the

non-dimensional, normalized temperature that describes the decay of the initial temperature profile. The non-dimensional temperature satisfies $0 \le h(t) \le 1$, $h(t=0)=1$ and $h(t \to \infty)=0$ to describe the decay of the initial temperature profile. Similarly, the distribution function will also obey this spatial variation $g_\omega(x,t,\mu)=e^{iqx}\tilde{g}_\omega(t,\mu)$ as well as the equilibrium distribution $g_0(x,t)=e^{iqx}\frac{C_\omega T_m}{4\pi}h(t)$, thus relating the equilibrium energy distribution to the temperature profile.

Integrating Eq. (2.1) with respect to frequency and the solid angle yields the equilibrium condition in the spectral case described previously and given by Eq. (1.3) [5]:

$$0=\int_0^{\omega_m}\int\frac{g_0-g_\omega}{\tau_\omega}d\Omega d\omega \tag{2.2}$$

Solving Eq. (2.1) yields the nonequilibrium energy density in terms of the temperature as:

$$\tilde{g}_\omega(t,\mu)=\frac{C_\omega T_m}{4\pi}\exp\left(-\frac{t}{\tau_\omega}(1+iqv_\omega\tau_\omega\mu)\right)+\frac{C_\omega T_m}{4\pi}\frac{1}{\tau_\omega}\int_0^t dt'h(t')\exp\left(-\frac{t-t'}{\tau_\omega}(1+iqv_\omega\tau_\omega\mu)\right) \tag{2.3}$$

where we have used the initial condition that the system is initially an equilibrium thermal distribution, i.e. $\tilde{g}_\omega(t=0,\mu)=\tilde{g}_0(t=0)=\frac{C_\omega T_m}{4\pi}$.

Inserting the solution into the equilibrium condition of Eq. (2.2) in the spectral case [5] to close the problem yields the integral equation for the non-dimensional temperature obtained previously [48,52]:

$$h(t)\int_0^{\omega_m}\frac{C_\omega}{\tau_\omega}d\omega=\int_0^{\omega_m}\frac{C_\omega}{\tau_\omega}b_\omega(t)d\omega+\int_0^t h(t')\int_0^{\omega_m}\frac{C_\omega}{\tau_\omega^2}b_\omega(t-t')d\omega dt' \tag{2.4}$$

where we have defined for simplicity $b_\omega(t)\equiv\exp\left(-\frac{t}{\tau_\omega}\right)\mathrm{sinc}(qv_\omega t)$. This integral equation is easily solved with a Laplace transform, and the temperature profile can be solved for with an inverse transform as obtained by Hua and Minnich [48]. Other methods to solving the BTE is to either obtain a numerical solution by solving the integral equation by finite differences [26,52], or by utilizing Monte Carlo techniques [37,50,51].

2.2 Variational solution to the 1D TTG

We depart from these established approaches by treating the unknown temperature distribution as a variational function and rewrite Eq. (2.4) by shifting all terms to one side of the equation to define:

$$H(t) = \int_0^{\omega_m} \frac{C_\omega}{\tau_\omega} b_\omega(t) d\omega - \bar{h}(t) \int_0^{\omega_m} \frac{C_\omega}{\tau_\omega} d\omega + \int_0^t \bar{h}(t') \int_0^{\omega_m} \frac{C_\omega}{\tau_\omega^2} b_\omega(t-t') d\omega dt' \tag{2.5}$$

If the function we guess for the temperature profile is the exact temperature profile that solves the BTE, then this function will be identically zero everywhere. The function H represents the error in energy conservation, and can be thought of as an artificial heat source/sink (up to constant factors such as 4π and T_m) as it has been defined from the temperature integral equation which comes from the equilibrium condition of the BTE [5]. In the exact case it should be zero everywhere, but since our trial function will not be the exact solution, we would like to optimize the function that makes $H(t)$ as close to zero as possible to minimize the error in our trial solution.

The optimization procedure can be done in several ways. One method is to mathematically define an error metric and minimize the error in order to calculate the variational parameter. Some common examples of error metrics are least squares $Er(\gamma) = \int_0^\infty H^2(t) dt$ and least absolute error $Er(\gamma) = \int_0^\infty |H(t)| dt$. Another approach is to require certain physical conditions to be met, and we can impose one physical condition for every variational parameter available in the trial solution. A simple, intuitive physical constraint is to impose that energy conservation should hold when considering the entire decay time. Doing so yields the following statement of energy conservation:

$$CT_m = iq \int_0^\infty Q(t) dt \tag{2.6}$$

The left hand side of Eq. (2.6) represents the energy per unit volume initially deposited by the heating lasers, while the right hand side represents the total energy flux over all time, where Q is the heat flux in the x-direction in complex form consistent with our complexified temperature. The heat flux is calculated by utilizing the spectral energy density solved from Eq. (2.1).

Calculating the flux and inputting the variational solution into Eq. (2.6), we utilize this physical condition to solve for the variational parameter, imposing that the trial function will satisfy energy conservation over the entire decay time just as the exact solution does. The key point is to optimize the trial function, either by imposing physical conditions to be met or mathematical error functions to be minimized and there are various ways to do so. We will show that both approaches provide good agreement with the exact numerically solved effective thermal conductivity.

Typically in the variational approach, one uses a trial function that is known from intuition about the system, and the trial function is optimized to minimize the chosen error function. The accuracy of the variational approach hinges upon the utilization of an appropriate trial function, which can be difficult to deduce. In solving the BTE with this variational approach, the Fourier heat conduction solution provides this trial function, especially since our goal is to extract the effective thermal conductivity (or in other cases properties such as interfacial thermal resistance, diffusivity, etc.) of the system.

For the one-dimensional TTG, the exact temperature solution of the Fourier heat conduction equation is $T(x,t)=T_0+T_m e^{iqx}e^{-\alpha q^2 t}$ where α is the thermal diffusivity. Therefore, we take for the trial function $\bar{h}(t)=e^{-\gamma t}$ with $\alpha_{eff}=\gamma/q^2$. While other trial functions can be inputted to approximately solve the BTE, the elegance of this approach is that it immediately utilizes the Fourier heat conduction temperature field appropriately modified as an input, and optimizes to find the modified properties such as effective thermal conductivity that solves the BTE with minimized error, converting the difficult task of solving an integral equation for the temperature distribution into a simple task of performing integration. This provides a more direct approach to obtaining the effective thermal conductivity and no longer needs to fit the derived solution to an exponential as the trial function itself takes this functional form. We note that in other heat transfer configurations, there can be multiple parameters in the trial solution, such as temperature slip that can occur due to the boundary resistance as well as effective thermal conductivity in the nondiffusive regime, but the Fourier heat conduction solution provides the starting point. In chapter 5, we will show the variational approach in which the thermal conductivity as well as the interface conductance will be used as variational parameters. Here, we demonstrate the technique on this simple case where only one variational parameter will be needed for simplicity.

Using the trial function, we can solve the condition of Eq. (2.6) to obtain for the thermal decay rate:

$$\gamma = \frac{\int_0^{\omega_m} d\omega \frac{C_\omega}{\tau_\omega}\left[1 - \frac{1}{\eta_\omega}\arctan(\eta_\omega)\right]}{\int_0^{\omega_m} d\omega C_\omega \frac{1}{\eta_\omega}\arctan(\eta_\omega)} \tag{2.7}$$

where we have defined the non-dimensional Knudsen number $\eta_\omega = q\Lambda_\omega = 2\pi\Lambda_\omega / \lambda$ where λ is the grating period. We utilize the normalized effective thermal conductivity for simplicity, defined as $\frac{k_{eff}}{k_{bulk}} = \frac{C\gamma}{q^2 k_{bulk}}$, where C is the heat capacity obtained by integrating the spectral heat capacity $C = \int C_\omega d\omega$. The bulk thermal conductivity is given by $k_{bulk} = \frac{1}{3}\int C_\omega v_\omega \Lambda_\omega d\omega$. In Fig. 2-1, we compare results obtained for Si and PbSe, for which previous approaches for obtaining the effective thermal conductivity include assuming a constant MFP distribution [52], an exact numerical solution [48,52], and the two-fluid model[18]. The spectral numerical results are obtained by fitting the exact solution of Eq. (2.2), obtained by finite differences, to the Fourier exponential profile [52]. The spectral variational results are plotted from Eq. (2.7) using the physical condition of Eq. (2.6). The least squares results are obtained numerically by inputting a set of values for the effective thermal conductivity into the function H, calculating the least squares integral for H as the error metric, and finding the appropriate value of the effective conductivity which minimizes the error. The gray variational results are obtained by taking the gray limit of Eq. (2.7), extracting a gray suppression function, and inputting into the effective thermal conductivity, i.e. $k_{eff,gray} = \frac{1}{3}\int_0^{\omega_m} C_\omega v_\omega \Lambda_\omega S_{gray}(\eta_\omega) d\omega$. Note that this gray approximation is identical to the 'frequency integrated gray medium' approach performed numerically by Collins *et al.* [52]. Silicon is known to have a wide range of MFPs, and shows that the gray solution derived suppression function does a poor job in reproducing the exact numerical results. We also look at PbSe, which has a narrower range of MFPs. We utilize the same material properties for Si and PbSe as utilized by Collins *et al.* for comparing between the numerical spectral solution and the variational solution developed here. Note that the optimized solution, both from the least squares method and from imposing a physical condition method, agree excellently with the exact numerical solution, which demonstrates the predictive power of the

variational approach and the freedom to perform the optimization in different ways. Here the two-fluid model deviates from the exact solution at smaller grating periods. The gray suppression function performs better for this material due to its narrower range of MFP's as compared to silicon [52].

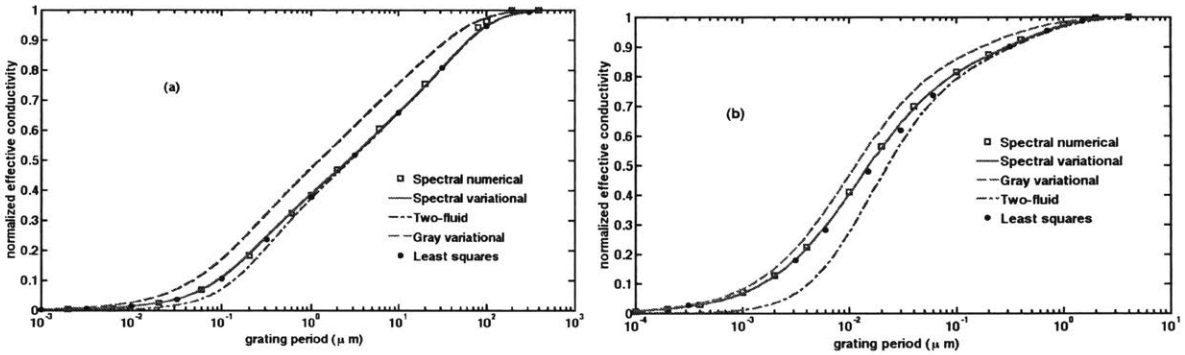

FIG. 2-1. 1D TTG effective thermal conductivity of (a) silicon and (b) PbSe. Here the effective thermal conductivity is plotted to compare the variational technique with the exact numerical technique and various approximations. The variational technique for the full spectral BTE, both with the physical condition of Eq. (2.5) and with least squares optimization, demonstrates excellent agreement with the exact numerical solution.

From the definition of the effective thermal conductivity and the thermal decay rate of Eq. (2.7), we extract a suppression function:

$$S_\omega = \frac{\frac{3}{\eta_\omega^2}\left[1-\frac{\arctan(\eta_\omega)}{\eta_\omega}\right]}{\int_0^{\omega_m} d\varpi \frac{C_\varpi}{C}\frac{\arctan(\eta_\varpi)}{\eta_\varpi}} \tag{2.8}$$

We note that although the numerator is dependent only on the ratio of MFP to the grating spacing and hence universal, the denominator depends in general on the material properties of the system. This result is significant not only because it shows the suppression function is not universally dependent on a ratio of MFP to a length in the system, but also because we now have a way to properly address this problem analytically and more generally, numerically. The numerator is equal to the suppression function previously derived by Maznev *et al.* [18] and has

been called the weakly quasiballistic suppression function [48]. Hua & Minnich have shown that there is in fact a correction to the suppression function in the full form, but their expression depends on the thermal decay time which intrinsically depends on the temperature solution to the BTE [48]. Our optimized solution provides the suppression function and illuminates its dependence on the grating period as well as its material property dependence. Furthermore, we can determine the validity domain of the two-fluid model by comparing the denominator of the optimized expression to unity. Thus, the following quantitative metric is obtained for the validity of the two-fluid model, $\left|\int_0^{\omega_m} d\omega \frac{C_\omega}{C} \frac{\arctan(\eta_\omega)}{\eta_\omega} - 1\right| << 1$. One could Taylor expand the suppression function of Eq. (2.8) for large values of the grating period relative to MFP to get an expression that is a first order correction to the two-fluid approximation for the thermal decay rate. In Fig. 2-2, we show the denominator of Eq. (2.8) for both Si and PbSe. We find that the two-fluid model can predict the effective thermal conductivity of Si with less than 5% error for grating spacings of 1 micron or higher. For PbSe, the two-fluid model has less than 5% error for grating spacings of 0.1 micron or higher. The cutoff grating spacing is larger for Si than for PbSe because Si has a MFP distribution that has a larger maximum MFP value than for PbSe, as shown in Fig. 2-1, hence demonstrates earlier deviation from the exact result.

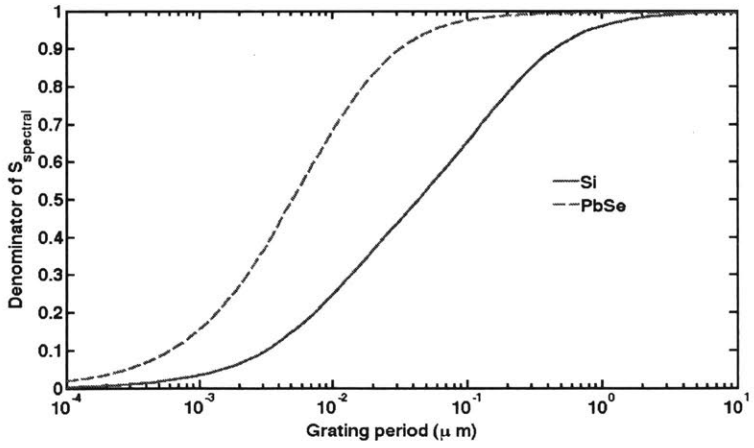

FIG. 2-2. Denominator of optimized spectral suppression function for Si (red) and PbSe (blue), yielding a metric for the validity of the two-fluid model.

The variational method can, of course, be applied to the gray case, for which we extract a suppression function that only depends on the Knudsen number. We take Eq. (2.8) and assume a constant MFP distribution to obtain:

$$S_{gray}(\eta_\omega) = \frac{3}{\eta_\omega^2}\left[1 - \frac{\arctan(\eta_\omega)}{\eta_\omega}\right]\left\{\frac{\eta_\omega}{\arctan(\eta_\omega)}\right\} \tag{2.9}$$

The term in the curly brackets is the additional factor we have obtained compared to the two-fluid model. The gray suppression function demonstrates a weaker suppression (higher effective thermal conductivity) than the two-fluid model due to this additional factor. The gray suppression function of Eq. (2.9) excellently reproduces the results of the normalized gray medium effective diffusivity obtained numerically previously by Collins *et al.* [52]. However, we have shown that indeed this approach of inputting the gray suppression function into the effective thermal conductivity expression is not universal, and performs rather poorly, especially for silicon as shown by the gray variational results from Fig. 2-1.

2.3 Summary

In summary, we have developed a variational approach that yields a new way of extracting the effective thermal conductivity of the system by exploiting knowledge of the Fourier heat conduction equation solution. In general, this approach to solving the temperature equation for the spectral BTE can directly yield the effective thermal conductivity from nondiffusive phonon transport experiments without brute force numerical solution of the BTE. We demonstrated the power of this approach in this chapter by calculating the thermal decay rate as well as an analytical suppression function for one-dimensional transient grating experiments. Our spectral suppression function yields the exact suppression of thermal conductivity. We have shown that the suppression function is not universal, and utilizing the gray solution to the BTE does not perform well in reproducing the exact spectral data. Moreover, the variational approach developed here can be used as a universal technique for solving the BTE and obtaining both experimental observables, such as measured heat flux or thermal decay rate, as well as the effective thermal conductivity. We will elaborate on the variational approach for the TTG in the

next chapter, applying it to the case of two-dimensional transport as is more experimentally relevant. We will analyze the solution to the BTE for a thin film that is optically transmissive, as well as for opaque substrates.

Chapter 3

TTG for thin films and opaque substrates

In the previous chapter, we laid out the details of the variational approach for the model system of the one-dimensional grating. In this chapter, we delve further into the TTG geometry, and solve the BTE with the variational approach to model thermal transport in thin films as well as opaque substrates. These two geometries, which are operated in transmission mode [16] and reflection mode [19], respectively, more accurately resemble the true TTG geometries used to measure nondiffusive heat transfer. The one-dimensional limit of the TTG of the previous chapter is the limit of very large film thicknesses for which the laser pulse penetrates far into the material, yielding only one-dimensional in-plane transport. Now we consider the true multi-dimensional transport problem in order to calculate effective thermal conductivities that depend on multiple experimental length scales.

3.1 Thin Film TTG

In the thin film TTG geometry, the materials utilized are optically transmissive, so that the diffraction pattern of the crossed laser beams is obtained on the opposite side of the film, and the temperature of the film is obtained from this diffraction pattern [16]. In this case, the system is heated approximately uniformly across the thickness of the film, with a sinusoidal in-plane spatial profile. Here, we demonstrate the utility of the variational approach for analyzing heat transport for nanostructures in multi-dimensional geometries and in the presence of phonon scattering at boundaries, which is more relevant to realistic experimental conditions. Specifically, we analyze the relaxation of a thermal grating in a suspended thin membrane [16]. The consideration of size effects from the thin film is critical to explain the experimentally obtained thermal decay profiles, especially for very thin films [17] and can reveal the reduction of thermal conductivity and deviation from the Fourier heat conduction solution both from the

size effects of the grating spacing and the film thickness. This is a nontrivial extension to the one-dimensional TTG since the spectral BTE is considerably harder to solve in a multi-dimensional geometry [26,27] and in the presence of boundary scattering. The thin film TTG geometry has been studied previously with the Monte Carlo approach[20]. In this chapter, we demonstrate the ability of the variational approach to provide an analytical form for the temperature profile and the associated thermal decay rate. This provides the ability to study the full material and geometry dependence of the thermal transport in the TTG in the transmission mode configuration. We demonstrate that results from this variational approach are in excellent agreement with Monte Carlo simulation on Si and PbSe. The variational approach offers the ability to accurately solve the BTE and study a wide range of materials in the nondiffusive regime with a closed form expression, and computationally a much faster way to study nondiffusive transport over a broad range of length scales for the film thickness and the thermal grating period.

We begin with the spectral Boltzmann transport equation under the relaxation time approximation for the spectral energy density:

$$\frac{\partial g_\omega}{\partial t} + \vec{v}_\omega \cdot \vec{\nabla} g_\omega = \frac{g_0 - g_\omega}{\tau_\omega} \tag{3.1}$$

where g_ω is the phonon energy density per unit frequency interval per unit solid angle above the reference background energy, related to the distribution function as $g_\omega = \frac{\hbar\omega D(\omega)}{4\pi}\left(f_\omega - f_0(T_0)\right)$. v_ω is the group velocity, τ_ω is the relaxation time, and g_0 is the equilibrium energy density, given by $g_0 \approx \frac{1}{4\pi} C_\omega (T - T_0)$ in the linear response regime. In the TTG experiment, the temperature initially has a sinusoidal periodic profile as $T(x, t=0) = T_0 + T_m e^{iqx}$ in complex form where T_m is the initial amplitude of the spatial variation and $q = 2\pi / \lambda$ is the wavevector for the grating sinusoidal profile. We assume that the initial temperature profile is uniform across the thickness of the film (depicted in Fig. 3-1) as is often the case in experiment[18]. We require $T_m << T_0$ to ensure we are in the linear response regime. We expect the temperature profile to obey $T(x,z,t) = T_0 + T_m e^{iqx} h(z,t)$ where $h(z,t)$ is the non-dimensional temperature that satisfies $0 \le h(z,t) \le 1$, $h(z, t=0) = 1$ and $h(z, t \to \infty) = 0$.

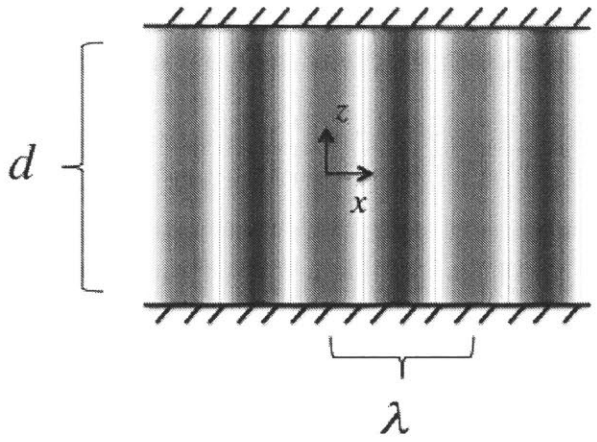

FIG. 3-1. Schematic showing the geometry and coordinate system for the thin film. The thickness of the film d is depicted separating the adiabatic top and bottom surfaces. The grating period λ shows the separation between hot spots (red) and cold spots (blue), which are uniform vertically across the membrane thickness initially ($t = 0$).

Similarly, the distribution function will be given by $g_\omega = e^{iqx}\tilde{g}_\omega$ and the equilibrium distribution by $\tilde{g}_0 = \frac{C_\omega T_m}{4\pi} h(z,t)$. The BTE now takes the form:

$$\frac{\partial \tilde{g}_\omega}{\partial t} + \mathrm{v}_\omega \left(iq\mu_x \tilde{g}_\omega + \mu_z \frac{\partial \tilde{g}_\omega}{\partial z} \right) = \frac{\tilde{g}_0 - \tilde{g}_\omega}{\tau_\omega} \tag{3.2}$$

where we have removed the y-dependence due to the translational symmetry, and define μ_x, μ_z as the direction cosines in the x (in-plane) and z (cross-plane) directions, respectively. If one measures a polar angle θ and azimuthal angle ϕ from the z-axis, then in that case the direction cosines are simply $\mu_z = \cos(\theta)$ and $\mu_x = \sin(\theta)\cos(\phi)$, but we will keep the form general. We utilize the Laplace transform in time and the initial condition of the temperature profile to reduce this partial differential equation to an ordinary differential equation:

$$\frac{\partial \hat{\tilde{g}}_\omega}{\partial u} + \frac{1 + s\tau_\omega + i\eta_\omega \mu_x}{2\mathrm{Kn}_\omega \mu_z} \hat{\tilde{g}}_\omega = \frac{\hat{\tilde{g}}_0 + \tau_\omega \frac{C_\omega T_m}{4\pi}}{2\mathrm{Kn}_\omega \mu_z} \tag{3.3}$$

where we have replaced z by a non-dimensional variable $u = 2z/d$ where d is the thickness of the thin film so that $-1 < u < 1$. Furthermore, we have defined the following non-dimensional quantities utilizing the mean free path $\Lambda_\omega = \mathrm{v}_\omega \tau_\omega$ to characterize the size effect of the grating spacing, $\eta_\omega = q\Lambda_\omega$, and the film thickness, $\mathrm{Kn}_\omega = \Lambda_\omega / d$, given by the Knudsen number. To simplify the notation, we will utilize the term $V \equiv \dfrac{1 + s\tau_\omega + i\eta_\omega \mu_x}{2\mathrm{Kn}_\omega \mu_z}$ to group the variables in a compact form. We impose adiabatic, diffuse boundary conditions at the top and bottom of the thin film,

$$\begin{aligned} \hat{\hat{g}}_\omega(u=-1, s, \mu_x, \mu_z > 0) &= \sigma_1 \\ \hat{\hat{g}}_\omega(u=1, s, \mu_x, \mu_z < 0) &= \sigma_2 \end{aligned} \tag{3.4}$$

where we define the following solid angle integrals:

$$\begin{aligned} \sigma_1 &\equiv \frac{1}{\pi}\int d\Omega\, \Theta(\mu_z)\mu_z \hat{\hat{g}}_\omega(u=-1, s, \mu_x, -\mu_z) \\ \sigma_2 &\equiv \frac{1}{\pi}\int d\Omega\, \Theta(\mu_z)\mu_z \hat{\hat{g}}_\omega(u=1, s, \mu_x, \mu_z) \end{aligned} \tag{3.5}$$

which are proportional to the spectral energy flux approaching the bottom and top walls of the thin films, respectively. Note the integrations are only over hemispheres representing flux towards the corresponding surface and not the entire solid angle. We have utilized the Heaviside step functions $\Theta(x)$ to restrict the integration region appropriately.

Solving Eq. (3.3) and applying the boundary conditions of Eq. (3.4) yields:

$$\begin{aligned} \hat{\hat{g}}_\omega(u, s, \mu_x, \mu_z) = {} & \Theta(\mu_z)\left\{\sigma_1 \exp(-V(u+1)) + \int_{-1}^{u} du' \exp(-V(u-u'))\frac{\hat{\hat{g}}_0(u', s) + \tau_\omega \dfrac{C_\omega T_m}{4\pi}}{2\mathrm{Kn}_\omega \mu_z}\right\} + \\ & \Theta(-\mu_z)\left\{\sigma_2 \exp(-V(u-1)) + \int_{1}^{u} du' \exp(-V(u-u'))\frac{\hat{\hat{g}}_0(u', s) + \tau_\omega \dfrac{C_\omega T_m}{4\pi}}{2\mathrm{Kn}_\omega \mu_z}\right\} \end{aligned} \tag{3.6}$$

where the first term describes phonons flowing towards the positive z-direction (top boundary) and the second term describes phonons flowing towards the negative z-direction (bottom boundary). Integrating the solution of Eq. (3.6) over the solid angle hemispheres at the walls from Eq. (3.5) yields coupled equations for the energy approaching the walls of the thin film,

σ_1, σ_2. Solving this coupled equation, and utilizing the even symmetry of the system about the center line $u = 0$ of the thin film yields:

$$\sigma_1 = \sigma_2 = \frac{2}{1-2F_3(2)} \int_{-1}^{1} du' \frac{\hat{\hat{g}}_0(u',s) + \tau_\omega \frac{C_\omega T_m}{4\pi}}{2\mathrm{Kn}_\omega} F_2(1+u') \tag{3.7}$$

where we have defined the following integral function for convenience:

$$F_n(u) \equiv \frac{1}{2\pi} \int d\Omega \Theta(\mu_z) \mu_z^{n-2} \exp(-Vu) \tag{3.8}$$

The symmetry of the coordinate system we have chosen requires that the temperature, and thus the equilibrium energy density, be even in the spatial variable u. Thus this completes the solution for the spectral energy density in terms of the equilibrium energy density (and thus the temperature) when combining the results of Eqs. (3.6-3.8).

Integrating Eq. (3.1) with respect to the solid angle and all phonon modes yields the equilibrium condition in the spectral case[5]. The equilibrium condition in this case can be expressed as:

$$2\int d\omega \frac{1}{\tau_\omega} \hat{\hat{g}}_0(u,s) = \int d\omega \frac{1}{\tau_\omega} \frac{1}{2\pi} \int d\Omega \hat{\hat{g}}_\omega(u,s,\mu_x,\mu_z) \tag{3.9}$$

Note that the integral over ω is a compact notation we use for simplicity where it implies a sum over all phonon polarizations and corresponding frequencies of those branches[36]. Inputting the solution of Eq. (3.6) into Eq. (3.9), and inputting the expression for the non-dimensional temperature $\hat{\hat{g}}_0(u,s) = \frac{C_\omega T_m}{4\pi} \hat{h}(u,s)$, we obtain the integral equation governing the temperature distribution:

$$\hat{h}(u,s) \int d\omega \frac{C_\omega}{\tau_\omega} = \int d\omega \frac{C_\omega}{\tau_\omega} \int_{-1}^{1} du' \frac{\hat{h}(u',s) + \tau_\omega}{4\mathrm{Kn}_\omega} \left\{ F_1(|u-u'|) + \frac{2F_2(1+u')}{1-2F_3(2)} \left[F_2(1+u) + F_2(1-u) \right] \right\} \tag{3.10}$$

Notice that this is an integral equation in the spatial variable u, which, after solving, would require an inverse Laplace transform to obtain the temporal decay of the temperature profile.

3.2 Variational solution to the thin film TTG

We seek an approximate solution of Eq. (3.10) by using a trial function obtained using the heat diffusion equation. In the thin film TTG geometry, the latter yields a very simple exponentially decaying solution of $T(\vec{r},t)=T_0+T_m e^{iqx}e^{-\alpha q^2 t}$, where α is the thermal diffusivity. Following the approach previously utilized for the one-dimensional TTG[64] in chapter 2, we take a trial solution $\bar{h}(u,t)=\exp(-\gamma t)$ where the decay rate $\gamma=q^2\alpha_{eff}$ is determined by the "effective" thermal diffusivity α_{eff}. By treating the latter as a parameter, we seek to optimize the chosen simple trial function to get the best approximate solution of Eq. (3.10).

As was demonstrated previously[64], one can take both a mathematical approach, seeking to reduce the least squares error of the error residual of the temperature equation from Eq. (3.10), or one can impose physical constraints that the trial function should satisfy. Since our trial function has only one variational parameter, it would suffice to impose a single condition to optimize the solution. The physical condition we pick is to demand energy conservation to hold over the thin film control volume considering the whole time decay. In this geometry, we take a control volume over the thickness of the film, and for convenience of a width equal to half of the grating period, centered at a peak in the temperature, where the temperature is above the average background in order to observe heat flux outwards laterally towards the troughs in the temperature spatial profile. By considering the entire decay time, energy conservation demands that the total energy initially deposited by the heating laser pulse into the control volume must be equal to the total energy that flows out of the control volume over the entire decay time. As the top and bottom surfaces of the thin film are adiabatic, we need not consider the flux in the z (cross plane) direction, q_z, and thus energy only flows out due to in-plane flux out of the control volume. Integrating over all time, and over the thickness of the thin film in the z direction, and over the width of the control volume in the x direction yields in complex form:

$$CT_m\frac{\lambda d}{\pi}=2i\int_{-\frac{d}{2}}^{\frac{d}{2}}dz\int_0^\infty dt\ \tilde{q}_x(z,t) \tag{3.11}$$

where q_x is the heat flux in the x (in-plane) direction, given by $q_x(x,z,t) = e^{iqx}\tilde{q}_x(z,t)$ due to the periodicity of the heating profile. Eq. (3.11) simply says that the total initial energy must be equal to the total flux away in the in-plane direction from peak to trough integrated over time.

Beyond a physical demand for energy conservation, Eq. (3.11) has also a mathematical benefit. In the 1D TTG model, it can be shown that imposing this physical constraint as demonstrated previously[64], makes it such that the area under the temperature decay curve from the trial exponential solution matches the area under the exact temperature decay. While this cannot be strictly proven in the thin film TTG problem due to the z dependence in the problem, the benefit of this is that a function that starts at unity will be constrained to match the area of the actual decay and for the monotonically decaying temperature profile, this will yield an excellent approximation, as will be seen in Fig. 3-2.

The heat flux is obtained by integrating the spectral energy density over the solid angle and phonon frequencies in the form $\hat{\tilde{q}}_x(u,s) = \int d\omega \mathrm{v}_\omega \int d\Omega \mu_x \hat{\tilde{g}}_\omega(u,s,\mu_x,\mu_z)$. Inputting the spectral energy density expression of Eq. (3.6) and integrating, we obtain:

$$\tilde{q}_x(u,s) = T_m \int d\omega C_\omega \; {}_\omega\!\int_{-1}^{1} du' \frac{h(u',s)+\tau_\omega}{\omega}\left\{G_1(|u-u'|) + \frac{2F_2(1+u')}{1-2F_3(2)}\left[G_2(1+u)+G_2(1-u)\right]\right\} \quad (3.12)$$

where the following solid angle functions have been introduced for convenience:

$$\begin{aligned} F_n(u) &= \frac{1}{2\pi}\int d\Omega \Theta(\mu_z)\mu_z^{n-2}e^{-Vu} \\ G_n(u) &= \frac{1}{2\pi}\int d\Omega \Theta(\mu_z)\mu_x\mu_z^{n-2}e^{-Vu} \end{aligned} \quad (3.13)$$

The in-plane heat flux can be integrated over the thickness of the film and after inputting the trial exponential function, whose Laplace transform is given by $\hat{h}(u,s) = \frac{1}{s+\gamma}$, and taking s to be zero to integrate over all time, the conservation equation of Eq. (3.11) can be solved to yield the thermal decay rate:

$$\gamma = \frac{\int d\omega \frac{C_\omega}{\tau_\omega}\left\{1 - \frac{1}{\eta_\omega}\arctan(\eta_\omega) + \Psi(\eta_\omega, \mathrm{Kn}_\omega)\right\}}{\int d\omega C_\omega \left\{\frac{1}{\eta_\omega}\arctan(\eta_\omega) - \Psi(\eta_\omega, \mathrm{Kn}_\omega)\right\}} \quad (3.14)$$

where we have defined the following functions given by solid angle integrals:

$$\Psi(\eta_\omega,\mathrm{Kn}_\omega)\equiv\psi_2-\frac{\psi_1^2}{\psi_0}$$

$$\psi_n(\eta_\omega,\mathrm{Kn}_\omega)\equiv\frac{1}{2\pi}\int d\Omega\Theta(\mu_z)\frac{\mathrm{Kn}_\omega\mu_z}{(1+i\eta_\omega\mu_x)^n}\left[1-\exp\left(-\frac{1+i\eta_\omega\mu_x}{\mathrm{Kn}_\omega\mu_z}\right)\right] \tag{3.15}$$

$$=\int_0^1 d\phi\int_0^1 d\mu\frac{\mathrm{Kn}_\omega\mu}{\left(1+i\eta_\omega\sqrt{1-\mu^2}\cos(2\pi\phi)\right)^n}\left[1-\exp\left(-\frac{1+i\eta_\omega\sqrt{1-\mu^2}\cos(2\pi\phi)}{\mathrm{Kn}_\omega\mu}\right)\right]$$

which can be viewed as generalizations of the exponential integral functions[71].

Using the relation of the thermal conductivity to the thermal decay rate from the Fourier heat conduction solution $k=\gamma C/q^2$, we obtain the effective thermal conductivity for the thin film TTG:

$$k=\frac{\frac{1}{3}\int d\omega C_\omega \mathrm{v}_\omega\Lambda_\omega\frac{3}{\eta_\omega^2}\left\{1-\frac{1}{\eta_\omega}\arctan(\eta_\omega)+\Psi(\eta_\omega,\mathrm{Kn}_\omega)\right\}}{\frac{1}{C}\int d\omega C_\omega\left\{\frac{1}{\eta_\omega}\arctan(\eta_\omega)-\Psi(\eta_\omega,\mathrm{Kn}_\omega)\right\}} \tag{3.16}$$

Note the complex material property dependence of the effective thermal conductivity, in that we have two integrals over phonon properties appearing. We take the limits of large membrane thickness and large grating spacing and verify the expected limits of the one-dimensional TTG expression[64] and the Fuchs-Sondheimer [42,43] formula:

$$k(d>>\Lambda_\omega,\lambda)=\frac{\frac{1}{3}\int d\omega C_\omega \mathrm{v}_\omega\Lambda_\omega\frac{3}{\eta_\omega^2}\left\{1-\frac{1}{\eta_\omega}\arctan(\eta_\omega)\right\}}{\frac{1}{C}\int d\omega C_\omega\frac{1}{\eta_\omega}\arctan(\eta_\omega)} \tag{3.17}$$

$$k(\lambda>>\Lambda_\omega,d)=\frac{1}{3}\int d\omega C_\omega \mathrm{v}_\omega\Lambda_\omega\left\{1-\frac{3}{2}\mathrm{Kn}_\omega\left[\frac{1}{4}-E_3\left(\frac{1}{\mathrm{Kn}_\omega}\right)+E_5\left(\frac{1}{\mathrm{Kn}_\omega}\right)\right]\right\}$$

The suppression function is defined by the relation to the effective thermal conductivity [18,52] as $k=\frac{1}{3}\int C_\omega \mathrm{v}_\omega\Lambda_\omega S_\omega\, d\omega$, where again the integral over ω implies a sum over all phonon polarizations and frequencies, in compact form [36]. The suppression function characterizes the effective reduction of the MFP of phonons due to size effects from the heat transfer geometry, which corresponds to a reduction in thermal conductivity. However, only in the large grating

period limit can a universal suppression function, necessary for MFP reconstruction from the previously developed reconstruction algorithm [37], be obtained.

The temperature decay curves for some representative thicknesses of film and grating spacings for Si and PbSe are shown in Fig. 3-2, utilizing the same material property data from the previous one-dimensional TTG studies [52,64]. The variational approach is compared against the Monte Carlo results obtained for the thin film TTG [20]. The variational approach demonstrates a predictive ability to studying the temperature decay over a broad range of grating periods, even into the strongly nondiffusive thermal transport regime, when the thermal decay deviates from exponential decay.

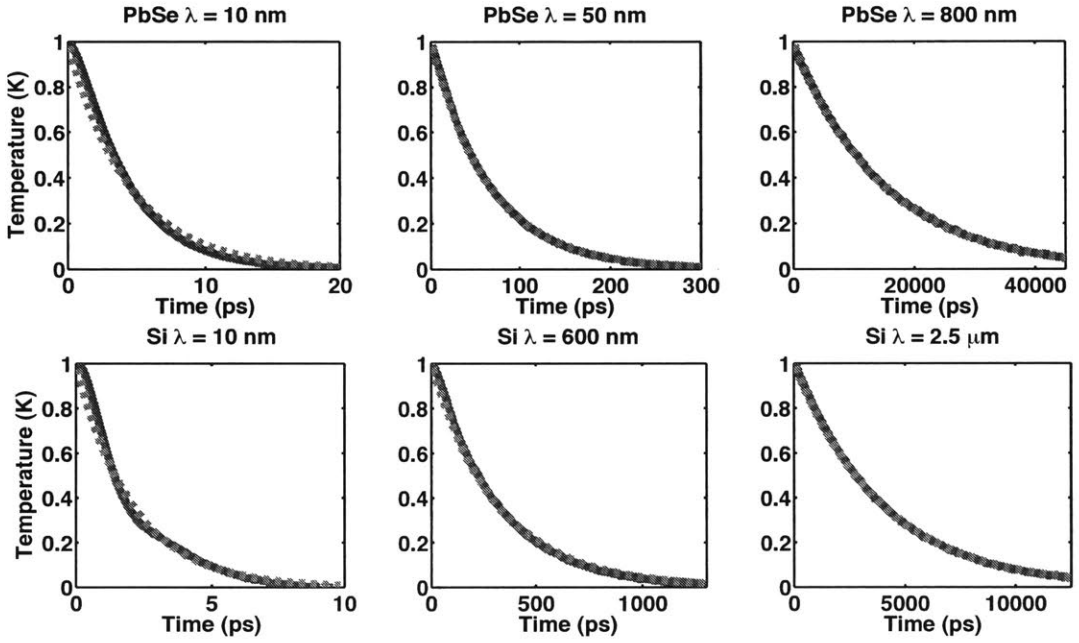

FIG. 3-2. Temperature decay dynamics for PbSe (10 nm thick film) and Si (390 nm thick film) for several grating spacings, comparing the results of the variational technique (dashed line) and Monte Carlo runs (solid line).

To get a clearer picture of the onset of nondiffusive transport, we plot the thermal decay rate against the square of the grating wavevector in Fig. 3-3. As the slope of this relation is equal to the thermal diffusivity, in the diffusive regime the dependence is linear [16,20]. For larger grating wavevectors q (i.e., at smaller periods λ), the solution visually deviates from the Fourier

heat conduction model, and this deviation occurs at TTG periods on the order of 5 microns and 50 nanometers for Si and PbSe, at membrane thicknesses of 390 nm and 10 nm, respectively. The thermal decay rate gives a quantitative method to determine when the conductivity deviates from the bulk value for a given membrane thickness. Note that this thermal conductivity obtained for large grating periods will still experience size effects from the membrane boundary scattering as predicted by the Fuchs-Sondheimer model [42,43]. This is a different metric for determining the onset of nondiffusive transport than looking at the thermal conductivity accumulation function and looking at the value for MFP's below which contribute to 50% of the thermal conductivity [6]. While the thermal conductivity accumulation function would yield a simple estimate at what length scales one would expect to observe nondiffusive transport, the utilization of the decay rate is a more rigorous method of taking into account the full effect of the geometry and heat transfer configuration of the system.

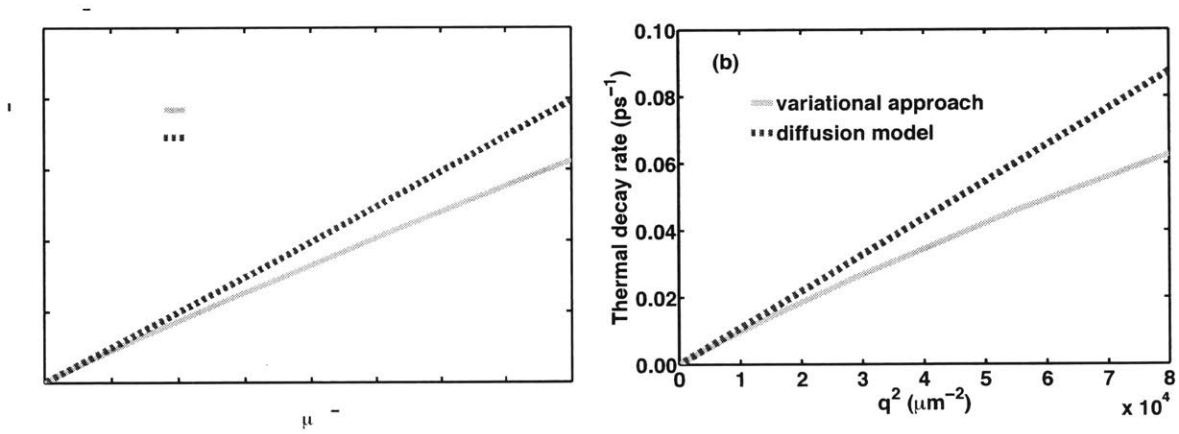

FIG. 3-3. Thermal decay rate plotted against wavevector squared for (a) Si and (b) PbSe. The deviation from the Fourier conduction model on the order of roughly 10% occurs at squared wavevector values on the order of 2 and 20,000 μm^{-2} for Si (390 nm membrane thickness) and PbSe (10 nm membrane thickness), respectively, which corresponds to on the order of 5 microns and 50 nm, respectively, to observe the onset of suppression of thermal conductivity.

The thermal decay rate from the Fourier heat conduction equation is directly related to the thermal conductivity, and utilizing this definition we extract the effective thermal conductivity as

given by Eq. (3.16). By normalizing to the bulk thermal conductivity, we compare the effective normalized thermal conductivity as a function of the grating period for various thickness films. Fig. 3-4 shows the effective thermal conductivities of Si and PbSe for various thicknesses of film, plotted against the grating period. The material properties are the same as those utilized in our previous work[64] and Collins *et al.*[52]. There is excellent agreement with the Monte Carlo results across a broad range of film thicknesses and grating periods. The Monte Carlo simulations were performed by my colleague, Dr. Lingping Zeng, and further details of this calculation can be found in Ref. [20].

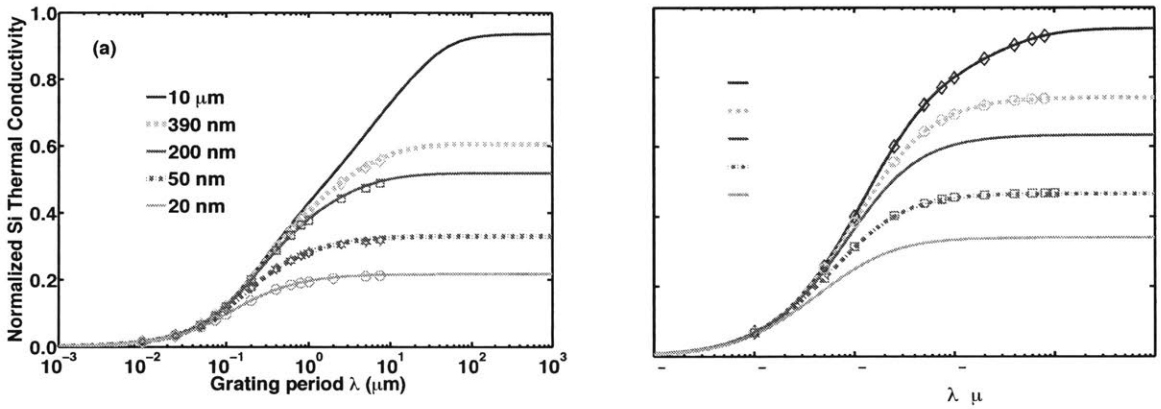

FIG. 3-4. Normalized effective thermal conductivity as a function of the grating period for various thicknesses (increasing in thickness from bottom line to top line) of the thin film for (a) Si and (b) PbSe. The variational approach (lines) yields effective conductivities that show excellent agreement with Monte Carlo simulations (symbols) over a broad range of grating periods and film thicknesses.

We can determine the grating period yielding a 5% reduction in the effective thermal conductivity compared to the Fuchs-Sondheimer (long grating period) limit. This provides a quantitative metric of the onset of nondiffusive transport for a given membrane thickness. From Fig. 3-4(a), we see that for Si, the grating period that is at the onset of nondiffusive transport occurs at approximately 40 μm , 10 μm , 7 μm , 3 μm , 2 μm for membrane thickness of 10 μm , 390 nm, 200 nm, 50 nm, and 20 nm, respectively. Similarly for PbSe, Fig. 3-4(b) shows

that the grating periods for which we can deduce the onset of nondiffusive transport occur at 300 nm, 120 nm, 90 nm, 60 nm, 50 nm for membrane thicknesses of 100 nm, 10 nm, 5 nm, 2 nm, and 1 nm, respectively. For both materials we see that the grating period for the onset of nondiffusive transport is shorter for thinner membranes, and this can be qualitatively explained by the reduction of the effective MFP of the systems due to the boundary scattering.

The variational approach demonstrates the simplicity of optimizing a trial solution from the diffusive temperature profile that the experimentalist fits to, rather than a brute force solution of the BTE followed by a fitting to a diffusive profile in order to extract material properties such as the effective thermal conductivity. This also provides the opportunity to obtain analytical solutions to the BTE for geometries that have never been obtained previously.

3.3 Reflection mode TTG

For materials that are opaque, the TTG cannot be operated in the transmission mode, but can be operated in the reflection mode, where the reflection of the probe beam is utilized in order to understand the temperature response of the surface. This is also useful for studying materials for which very thin films cannot be experimentally manufactured. The assumption made in the thin film TTG is that the heating is uniform across the thickness of the film, which requires a balance between the optical penetration depth of the heating and the thickness of the film.

The reflection geometry provides the opportunity to study once again the interplay between the in-plane length scale of the grating period and a cross plane length scale. While in the thin film TTG the cross plane length scale was determined by the thickness of the film, which serves to scatter phonons at the boundaries, the cross plane length scale in this case is the optical penetration depth. In this chapter we will explore the interplay between this variables and how the effective thermal conductivity behaves as a function of these two variables and how well the variational approach with the modified Fourier temperature distribution can perform.

In the TTG experiment, the response in reflection mode is different than in transmission mode for thin films. In this case, the diffusive temperature profile has been solved previously in order to analyze the temperature signal using TTG for opaque materials [72]. For the

experimental conditions of a spatially periodic heating, the temperature is given by $T(x,z,t)=T_0+T_0e^{iqx}h(z,t)$ in complex form, and this serves as a definition of the non-dimensional temperature h. The temperature T_0 is the background equilibrium temperature of the system, for example the room temperature. The heating by the laser is incorporated with a volumetric heat generation term, given by the functional form:

$$Q=\delta(t)e^{iqx}U_0\beta\exp(-\beta z) \tag{3.18}$$

where U_0 represents the energy per unit area deposited into the substrate by the pulse, and β is the inverse penetration depth of the heating profile. The previous derivation took into consideration different in-plane and cross-plane thermal conductivities to prove that the experimental signal is sensitive to only the in-plane thermal conductivity[72]. For simplicity, we show the derivation for an isotropic system, but the results can be extended to an anisotropic system. Given that we will utilize a single, isotropic value of conductivity, we present the Fourier heat conduction equation in this case:

$$\frac{\partial h}{\partial t}=-\alpha q^2h+\alpha\frac{\partial^2 h}{\partial z^2}+\frac{\beta U_0}{CT_0}\exp(-\beta z)\delta(t) \tag{3.19}$$

with the initial and boundary conditions given by:

$$\begin{aligned} h(z,t=0^-)&=0\\ \left.\frac{\partial h}{\partial z}\right|_{z=0}&=0\\ h(z\to\infty,t)&=0 \end{aligned} \tag{3.20}$$

which assumes an adiabatic surface at $z = 0$, and that the system starts at equilibrium prior to the energy deposited by the laser. We present the solution in the Laplace transformed domain for convenience and future utilization in the variational approach for the BTE solution:

$$\hat{h}(z,s)=\frac{\frac{\beta U_0}{CT_0}}{s+\alpha(q^2-\beta^2)}\left[\exp(-\beta z)-\frac{\beta}{\sqrt{q^2+s/\alpha}}\exp\left(-z\sqrt{q^2+s/\alpha}\right)\right] \tag{3.21}$$

We will utilize the Fourier heat conduction temperature profile in our variational solution of the BTE. Taking the inverse Laplace transform of this yields the temperature as a function of the depth into the substrate and time:

$$h(z,t)=\frac{\beta U_0}{CT_0}\exp\left(-\alpha t\left(q^2-\beta^2\right)\right)\frac{1}{2}\left\{\exp(\beta z)\operatorname{erfc}\left(\beta\sqrt{\alpha t}+\frac{z}{2\sqrt{\alpha t}}\right)+\exp(-\beta z)\operatorname{erfc}\left(\beta\sqrt{\alpha t}-\frac{z}{2\sqrt{\alpha t}}\right)\right\} \tag{3.22}$$

where the surface heating profile is:

$$h(z=0,t)=\frac{\beta U_0}{CT_0}\exp\left(-\alpha t\left(q^2-\beta^2\right)\right)\operatorname{erfc}\left(\beta\sqrt{\alpha t}\right) \tag{3.23}$$

To solve for the thermal transport in the nondiffusive regime, once again we begin with the spectral Boltzmann transport equation under the relaxation time approximation:

$$\frac{\partial g_\omega}{\partial t}+\vec{v}_\omega\cdot\vec{\nabla}g_\omega=\frac{g_0-g_\omega}{\tau_\omega}+\frac{Q_\omega}{4\pi} \tag{3.24}$$

The sinusoidal heating profile in the x-direction (in-plane), given by the pulse form $Q_\omega(x,z,t)=\delta(t)e^{iqx}\tilde{Q}_\omega(z)$, means we can expect that the spectral and equilibrium energy densities to also obey a sinusoidal profile $g_\omega=e^{iqx}\tilde{g}_\omega$ and the equilibrium distribution will simplify accordingly as $\tilde{g}_0\ \frac{C_\omega T_0}{4\pi}h(z,t)$. By inputting this in-plane sinusoidal profile and utilizing the Laplace transform (denoted by the ^ symbol) in the time domain, the BTE simplifies to:

$$\frac{\partial\hat{\tilde{g}}_\omega}{\partial z}+\hat{\tilde{g}}_\omega\frac{1+s\tau_\omega+i\eta_\omega\mu_x}{\Lambda_\omega\mu_z}=\frac{\hat{\tilde{g}}_0+\tau_\omega\frac{\tilde{Q}_\omega}{4\pi}}{\Lambda_\omega\mu_z} \tag{3.25}$$

where we have defined $\eta_\omega=q\Lambda_\omega$. For convenience, we define the parameter $V\equiv\frac{1+s\tau_\omega+i\eta_\omega\mu_x}{\Lambda_\omega\mu_z}$ to group the variables in a compact form for the following solution of the BTE:

$$\hat{\tilde{g}}_\omega(z,s,\mu_x,\mu_z)=\exp(-Vz)\hat{\tilde{g}}_\omega(z=0,s,\mu_x,\mu_z)+\int_0^z dz'\exp\left(-V(z-z')\right)\frac{\hat{\tilde{g}}_0(z',s)+\tau_\omega\frac{\tilde{Q}_\omega}{4\pi}}{\Lambda_\omega\mu_z} \tag{3.26}$$

The boundary conditions are taken to be:

$$\begin{aligned}\hat{\tilde{g}}_\omega(z=L,s,\mu_x,\mu_z<0)&=0\\ \hat{\tilde{g}}_\omega(z=0,s,\mu_x,\mu_z>0)&=\sigma\end{aligned} \tag{3.27}$$

The first boundary condition takes an imaginary blackbody wall at length L into the substrate at the background temperature to account for the semi-infinite substrate, and later we will take this

length to infinity. The second boundary condition allows for the adiabatic boundary condition of with diffuse scattering, where $\sigma = \frac{1}{\pi}\int d\Omega\Theta(\mu_z)\mu_z\hat{\tilde{g}}_\omega(z=0,s,\mu_x,-\mu_z)$, which is proportional to the specular heat flux approaching the surface. We have utilized the Heaviside step function to reduce the integration over the solid angle only to consider phonons approaching the surface. Solving the boundary conditions, and taking the artificial length L to infinity yields the formal solution to the BTE for the spectral energy density in terms of the equilibrium energy density:

$$\hat{\tilde{g}}_\omega(z,s,\mu_x,\mu_z) = -\Theta(-\mu_z)\int_z^\infty dz' \frac{\hat{\tilde{g}}_0(z',s)+\frac{\tau_\omega\tilde{Q}_\omega(z')}{4\pi}}{\Lambda_\omega\mu_z}\exp\left(-V(z-z')\right)$$
$$\Theta(\mu_z)\left\{\begin{array}{l}\int_0^z dz' \frac{\hat{\tilde{g}}_0(z',s)+\frac{\tau_\omega\tilde{Q}_\omega(z')}{4\pi}}{\Lambda_\omega\mu_z}\exp\left(-V(z-z')\right)+ \\ \int_0^\infty dz' \frac{\hat{\tilde{g}}_0(z',s)+\frac{\tau_\omega\tilde{Q}_\omega(z')}{4\pi}}{\Lambda_\omega} 2\exp(-Vz)F_2(z')\end{array}\right\} \quad (3.28)$$

where we have defined the following solid angle integral function:

$$F_n(z) \equiv \frac{1}{2\pi}\int d\Omega\Theta(\mu_z)\mu_z^{n-2}e^{-Vz} \quad (3.29)$$

The first term represents phonons moving towards the surface of heating at $z = 0$, whereas the second term represents phonons moving away from the surface.

The temperature equation can be derived by utilizing the equilibrium condition obtained by integrating Eq. (3.24) with respect to frequency and the solid angle [5]. The equilibrium condition in this case can be expressed as:

$$4\pi\int d\omega\frac{1}{\tau_\omega}\hat{\tilde{g}}_0(z,s) = \int d\omega\frac{1}{\tau_\omega}\int d\Omega\hat{\tilde{g}}_\omega(z,s,\mu_x,\mu_z) \quad (3.30)$$

Performing the solid angle integral, and inputting the expression for the non-dimensional temperature expression $\hat{\tilde{g}}_0(z,s) = \frac{C_\omega T_0}{4\pi}\hat{h}(z,s)$, we obtain the integral equation for the temperature distribution:

$$\hat{h}(z,s)\int d\omega\frac{C_\omega}{\tau_\omega} = \int d\omega\frac{C_\omega}{\tau_\omega}\frac{1}{2\Lambda_\omega}\int_0^\infty dz'\left[\hat{h}(z',s)+\frac{\tau_\omega\tilde{Q}_\omega(z')}{C_\omega T_0}\right]\left\{F_1(|z-z'|)+2F_2(z)F_2(z')\right\} \quad (3.31)$$

This is an integral equation in the spatial variable z for the non-dimensional temperature in the Laplace domain, which after solving requires an inverse Laplace transform in order to obtain the full temperature solution in the time domain. For the thermal distribution, the spectral heat generation takes the form:

$$\tilde{Q}_{\omega}(z) = \frac{C_{\omega}}{C} U_0 \beta \exp(-\beta z) \tag{3.32}$$

While other distributions can be taken, we utilize this form in order to compare to the Fourier heat conduction solution.

3.4 Variational solution to the TTG in reflection mode

We will again utilize the known Fourier heat conduction solution as a starting point for the variational trial function. The simplest trial function is to take the diffusive temperature profile and allow just the thermal diffusivity to be a variational parameter. In general, the size effects exhibited by the BTE will affect both the temporal as well as the spatial distributions of the temperature. However, the simple variational solution that varies only one parameter, the thermal diffusivity, we will show already does an excellent job in approximately solving the thermal decay from the BTE over a broad range of grating period length scales. Thus, we proceed by taking the Fourier heat conduction solution of Eq. (3.21) as a trial function and use the thermal diffusivity as the variational parameter.

To solve for the variational parameter, we will impose that the trial function must satisfy energy conservation taken over the control volume of the semi-infinite substrate over all time, quite analogous to the condition utilized for the thin film TTG geometry [65]. This mathematical condition can be obtained by integrating the BTE of Eq. (3.24) over the solid angle and frequency, and then also over the depth variable z as well as over all time to yield:

$$U_0 \frac{\lambda}{\pi} = 2i \int_0^{\infty} dz \int_0^{\infty} dt \; \tilde{q}_x(z,t) \tag{3.33}$$

This statement says that the total energy per unit area perpendicular to the z-axis deposited in the semi-infinite substrate initially (left hand side of Eq. (3.33)) must be equal to the total energy that

moves away in the in-plane direction. The in-plane heat flux is obtained by utilizing the spectral energy density of Eq. (3.28), and integrating over the frequency and solid angle, i.e. $\hat{\tilde{q}}_x(z,s) = \int d\omega \int d\Omega \; \mathrm{v}_\omega \mu_x \hat{\tilde{g}}_\omega(z,s,\mu_x,\mu_z)$, to obtain the in-plane heat flux:

$$\hat{\tilde{q}}_x(z,s) = \frac{1}{2} T_0 \int d\omega C_\omega \mathrm{v}_\omega \frac{1}{\Lambda_\omega} \int_0^\infty dz' \left[\hat{h}(z',s) + \frac{\tau_\omega \tilde{Q}_\omega(z')}{C_\omega T_0} \right] \left[G_1(|z-z'|) + 2G_2(z) F_2(z') \right] \tag{3.34}$$

where we have defined the solid angle integral function:

$$G_n(z) \equiv \frac{1}{2\pi} \int d\Omega \Theta(\mu_z) \mu_z^{n-2} \mu_x \exp(-Vz) \tag{3.35}$$

Inserting the heat flux expression of Eq. (3.34) into the energy conservation statement of Eq. (3.33), and inputting the variational trial function of the Fourier heat conduction solution of Eq. (3.21) as well as the thermal distribution for the heat generation rate, we can solve for the effective thermal conductivity after cleaning up some of the solid angle integrals. We obtain a form similar in structure to the results from the thin film TTG [65] of Eq. (3.16):

$$k = \frac{\frac{1}{3} \int d\omega C_\omega \mathrm{v}_\omega \Lambda_\omega f(\eta_\omega, \mathrm{Kn}_\omega)}{\frac{1}{C} \int d\omega C_\omega g(\eta_\omega, \mathrm{Kn}_\omega)} \tag{3.36}$$

where f and g of the kernels that characterize the size effects, given by:

$$\begin{aligned} f(\eta_\omega, \mathrm{Kn}_\omega) &= \frac{3}{\eta_\omega^2} \left\{ 1 - \frac{1}{\eta_\omega} \arctan(\eta_\omega) + \frac{\eta_\omega^2 \Psi(\eta_\omega, \mathrm{Kn}_\omega) - \mathrm{Kn}_\omega^2 \Psi(\eta_\omega, \eta_\omega)}{\eta_\omega^2 - \mathrm{Kn}_\omega^2} \right\} \\ g(\eta_\omega, \mathrm{Kn}_\omega) &= \frac{1}{\eta_\omega} \arctan(\eta_\omega) - \Psi(\eta_\omega, \mathrm{Kn}_\omega) \end{aligned} \tag{3.37}$$

We have defined the following solid angle integral functions:

$$\begin{aligned} \Psi(x,z) &\equiv \frac{1}{2} \psi_1(x,z) - \frac{1}{1+\sqrt{1+x^2}} \psi_0(x,z) \\ \psi_n(x,z) &\equiv \frac{1}{2\pi} \int d\Omega \Theta(\mu_z) \frac{1}{(1+ix\mu_x)^n} \frac{z\mu_z}{1+z\mu_z+ix\mu_x} \\ &= \int_0^1 \mu \int_0^1 d\phi \frac{1}{\left[1+ix\sqrt{1-\mu^2}\cos(2\pi\phi)\right]} \frac{z\mu}{1+z\mu+ix\sqrt{1-\mu^2}\cos(2\pi\phi)} \end{aligned} \tag{3.38}$$

If we take the limit of $\mathrm{Kn}_\omega \to 0$, i.e. the case of very long penetration depth, the solid angle integrals vanish as $\psi_n(\eta_\omega, \mathrm{Kn}_\omega \to 0) \propto \mathrm{Kn}_\omega$, and we recover the one-dimensional TTG limit as in

this case the substrate essentially starts off at a uniform temperature, and we recover the previously derived effective thermal conductivity [64]. The more interesting case for this problem is the simplification of surface heating, i.e. $\mathrm{Kn}_\omega \to \infty$. In this case, the kernel functions simplify to:

$$\begin{aligned} f\left(\eta_\omega, \mathrm{Kn}_\omega \to \infty\right) &= \frac{1}{2}\frac{3}{\eta_\omega^2}\left[1-\frac{1}{\eta_\omega}\arctan\left(\eta_\omega\right)\right]-\frac{1}{2}\frac{2}{1+\sqrt{1+\eta_\omega^2}}\frac{1}{\eta_\omega^3}\left[\left(1+\eta_\omega^2\right)^{\frac{3}{2}}-\frac{3}{2}\eta_\omega^2-\eta_\omega^3-1\right] \\ g\left(\eta_\omega, \mathrm{Kn}_\omega \to \infty\right) &= \frac{1}{2}\frac{1}{\eta_\omega}\arctan\left(\eta_\omega\right)+\frac{1}{2}\frac{2}{1+\sqrt{1+\eta_\omega^2}} \end{aligned} \tag{3.39}$$

For the general case of arbitrary penetration depth, the solid angle integral functions can be calculated analytically to obtain:

$$\psi_0(x,z)=\begin{cases} z\dfrac{1+z-\sqrt{1+x^2}}{z^2-x^2}+\dfrac{z^2}{\left(x^2-z^2\right)^{\frac{3}{2}}}\left[\begin{array}{l}\arctan\left(\sqrt{x^2-z^2}\right)+\arctan\left(\dfrac{1}{z}\sqrt{x^2-z^2}\right)\\ -\arctan\left(\dfrac{1}{z}\sqrt{1+x^2}\sqrt{x^2-z^2}\right)\end{array}\right] & z<x \\ \dfrac{\left(1+x^2\right)^{\frac{3}{2}}-x^3-1}{3x} & z=x \\ z\dfrac{1+z-\sqrt{1+x^2}}{z^2-x^2}+\dfrac{z^2}{\left(z^2-x^2\right)^{\frac{3}{2}}}\ln\left(\dfrac{1+\dfrac{1}{z}\sqrt{1+x^2}\sqrt{z^2-x^2}}{\left(1+\sqrt{z^2-x^2}\right)\left(1+\dfrac{1}{z}\sqrt{z^2-x^2}\right)}\right) & z>x \end{cases} \tag{3.40}$$

$$\psi_1(x,z)=\begin{cases} \dfrac{1}{x}\arctan(x)-\dfrac{1}{\sqrt{x^2-z^2}}\left[\begin{array}{l}\arctan\left(\sqrt{x^2-z^2}\right)+\arctan\left(\dfrac{1}{z}\sqrt{x^2-z^2}\right)\\ -\arctan\left(\dfrac{1}{z}\sqrt{1+x^2}\sqrt{x^2-z^2}\right)\end{array}\right] & z<x \\ \dfrac{1}{x}\arctan(x)-1+\dfrac{x}{1+\sqrt{1+x^2}} & z=x \\ \dfrac{1}{x}\arctan(x)+\dfrac{1}{\sqrt{z^2-x^2}}\ln\left(\dfrac{1+\dfrac{1}{z}\sqrt{1+x^2}\sqrt{z^2-x^2}}{\left(1+\sqrt{z^2-x^2}\right)\left(1+\dfrac{1}{z}\sqrt{z^2-x^2}\right)}\right) & z>x \end{cases}$$

which allows for a fully analytical effective thermal conductivity for any penetration depth into the substrate.

3.5 Different length scales have different effects

To study the effect of the optical penetration depth in the case of a diffuse surface boundary condition, we first plot the kernels f and g as a function of η_ω for varying values of Kn_ω. The 1D limit of $\mathrm{Kn}_\omega \to 0$ and the surface heating limit of $\mathrm{Kn}_\omega \to \infty$ define the envelope curves for which the kernels for arbitrary values of the penetration depth must lie between. As the Knudsen number increases, the size effect due to the optical penetration depth increases, which physically results in a decrease of the effective thermal conductivity. This occurs due to the decrease in the numerator kernel f, and the increase of the denominator kernel g. Figure 1 shows that these two envelopes of the one-dimensional limit and the surface heating limits are quite close, indicating that the effective thermal conductivity due to a diffuse boundary experiences weak effects from the optical penetration depth, as predicted by this variational approach to solving the BTE.

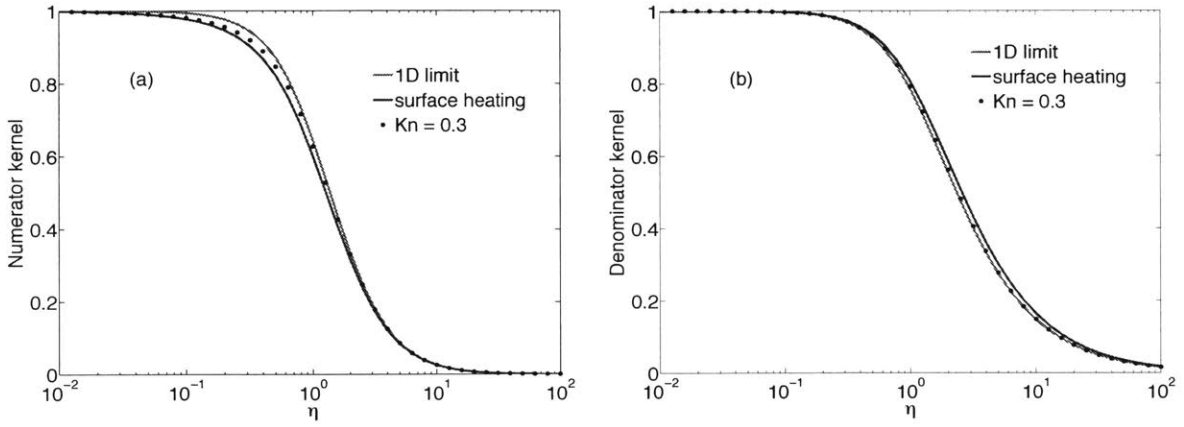

FIG. 3-5. Kernels of the effective conductivity. The numerator kernel f (a) that shows the size effects and appears beside the differential conductivity and the denominator kernel g (b) that shows the size effects and appears beside the spectral heat capacity. These indicate that the optical penetration depth does not have a large effect on the effective thermal conductivity with the diffuse surface boundary condition.

Utilizing the derived kernels to calculate the effective thermal conductivity for silicon, we show in Fig. 3-6 the effective thermal conductivity in the various limits. We utilize the optical penetration depth value of $\beta^{-1} = 500$ nm. Note that the effective thermal conductivity is quite similar in the one-dimensional limit and the surface heating limit. As expected, when the thermal grating period is much smaller than the optical penetration depth, the effective thermal conductivity takes on values of the one-dimensional limit, as the transport is mostly in-plane. In the opposite case when the grating period is much larger than the optical penetration depth, the effective thermal conductivity limits to the surface heating limit.

Figure 2 demonstrates that the variational technique does not show that the transport has a strong dependence on the optical penetration depth. Thus, the one-dimensional limit of the TTG[64] for the thermal conductivity captures the behavior of what we would expect for any material, even though the temperature profile is still two dimensional. While the effective conductivity is shown for silicon, this is true especially given the results of Fig. 3-5 so that regardless of the material, the kernels do not show strong dependence on the optical penetration depth, and thus the variational approach will not predict strong size effects from the optical penetration depth.

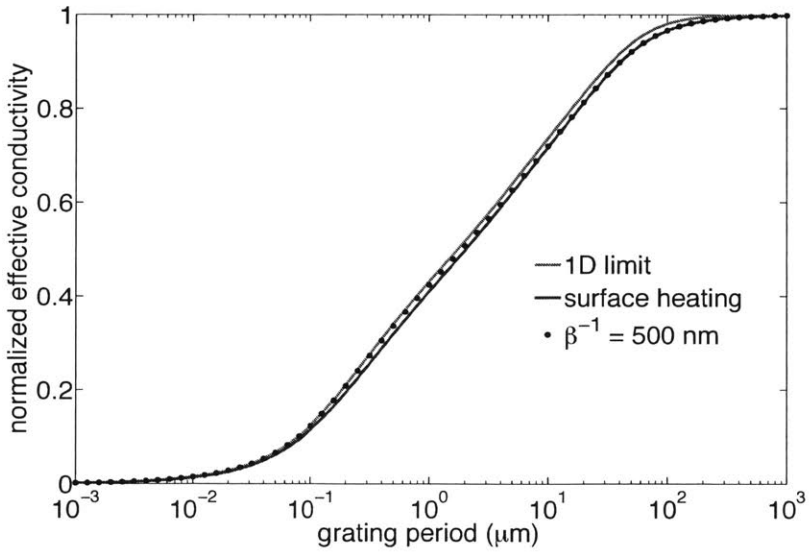

FIG. 3-6. Effective thermal conductivity for silicon in reflection mode TTG. We show the results of the diffuse surface variational technique for silicon as markers over a wide range of thermal grating periods, as well as the one-dimensional limit and the surface heating limit.

An interesting physical difference between the reflection TTG and the thin film TTG is the size effect due to the defined Knudsen number in each case. In the limit of large grating periods, the thin film TTG limits to the Fuchs-Sondheimer [42,43] problem of in-plane transport, and there is still a reduction of the effective thermal conductivity due to the finite size of the membrane. In the reflection TTG, the limit of large grating period yields the bulk thermal conductivity, regardless of the optical penetration depth. This demonstrates the limitation of a modified Fourier approach in capturing the details of a thermal decay due to a very localized heat source. The transport for short times will be nondiffusive, and after large enough time that scattering among phonons makes the decay diffusive, then the system will behave as if it has a bulk thermal conductivity. The variational method is able to capture the result that the thermal conductivity that best recovers this behavior is bulk, however it is not capable of capturing the nondiffusive effects at very short penetration depths when the time of decay is on the order of some of the relaxation times of the phonons. The variational approach is not limited to using the modified Fourier temperature profile as an input solution, and other functional forms can be inputted if one is interested in capturing the short time decay. However, in the interest of being able to extract the effective thermal conductivity, the modified Fourier profile is used, and the variational condition of Eq. (3.33) is used for consistency for all length scales rather than using different variational conditions for different length scales. Figure 3-7 shows the regime in which the variational approach is least accurate, which is for large grating periods and short optical penetration depths.

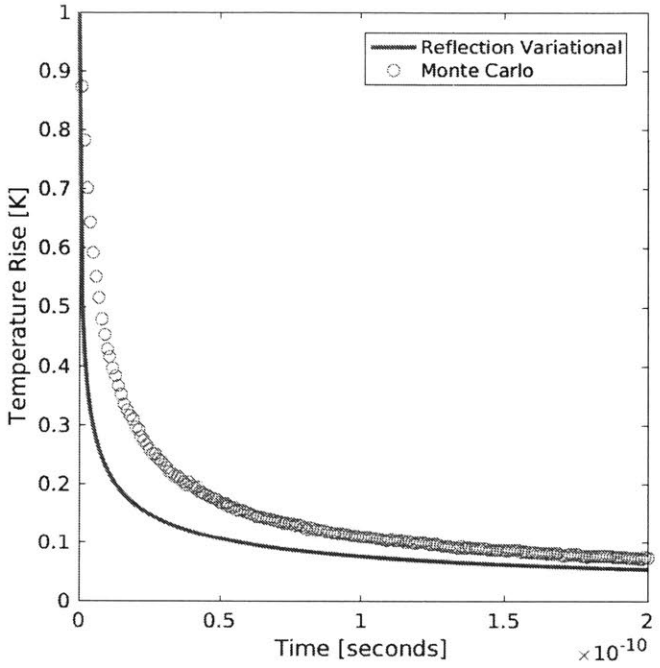

FIG. 3-7. Comparison of variational method with Monte Carlo simulations for silicon with a grating period of 10 micron and a penetration depth of 10 nm. For short times, as shown for 100 picoseconds or less, the modified Fourier profile decays too quickly as it predicts bulk thermal conductivity whereas the transport achieves diffusive behavior for longer times, as indicated by the better agreement after 100 picoseconds.

When the optical penetration depth is large compared to the grating period, the transport is effectively one-dimensional and only in-plane, and the results will be given by the 1D TTG for the effective thermal conductivity and the accuracy in this regime has been demonstrated previously [64]. However, when the grating period is very large, but the optical penetration depth is very small, the temperature response is nondiffusive for short times, and eventually becomes diffusive. The variational condition predicts that a bulk thermal conductivity captures this due to the weighting of considering all times in Eq. (3.33).

In the experiment, often the grating periods utilized are on the order of single microns [16,19], and the optical penetration depth on the order of hundreds of nanometers (500nm for Si). In this case, the agreement with the variational method utilizing the modified Fourier temperature

profile is expected to be far better. Figure 3-8 shows the comparison between experiment and the variational approach, utilizing the generated DFT properties as input into the variational formula of Eq. (3.36) [73]. The experiments were performed by my colleagues Samuel Huberman and Ryan Duncan, utilizing the table-top TTG experimental set up of Professor Keith Nelson of the Chemistry department of MIT. Further details into the experimental set up and alloy properties utilized for SiGe can be found in Ref. [73].

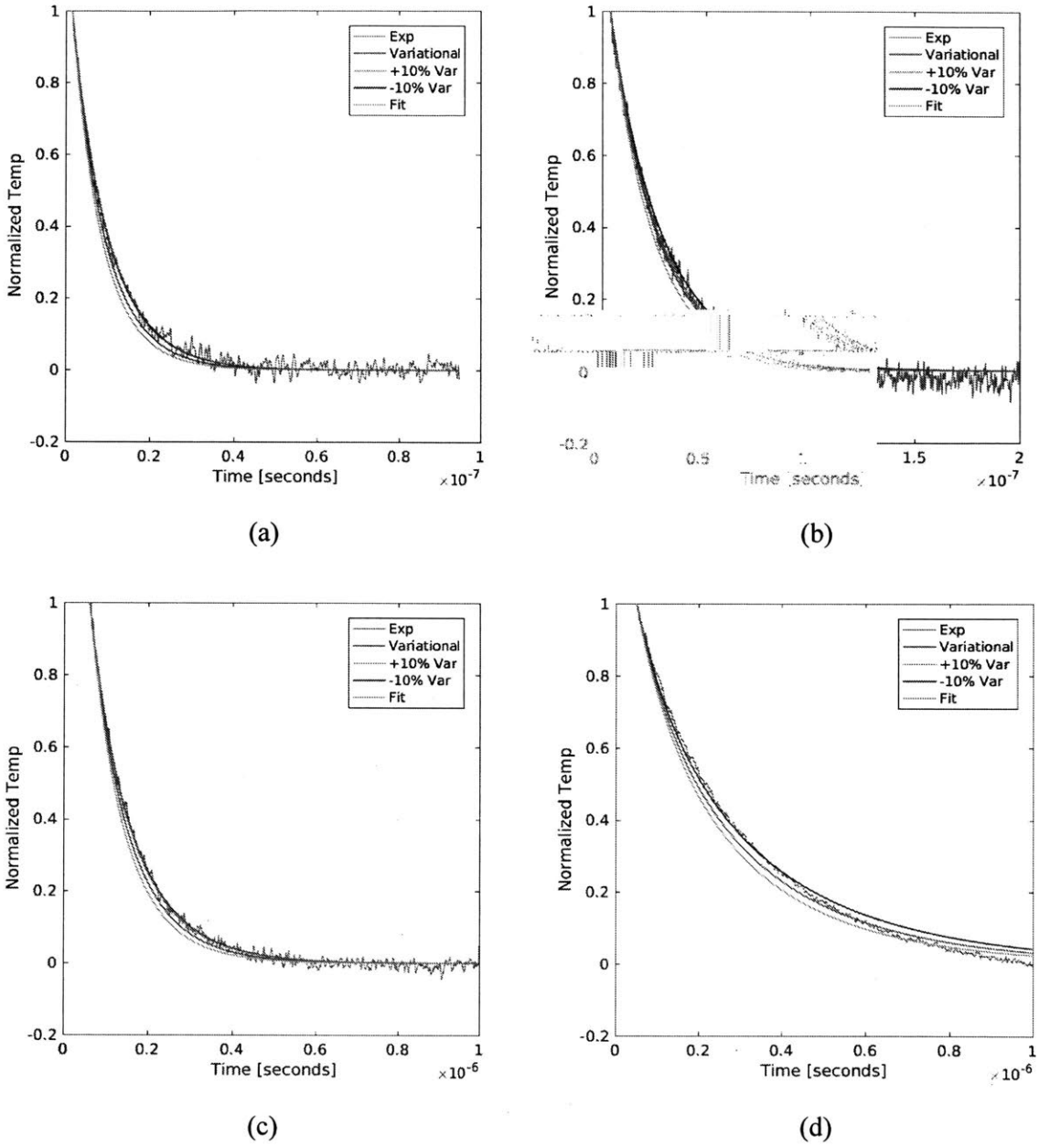

FIG. 3-8. Temperature decay from experiment compared with the variational approach in reflection mode TTG. We see the comparison between the experimental measurements as well as the variational approach for SiGe (~ 6% Ge) over several grating periods of 1 micron (a), 2.05 microns (b), 4.9 microns (c), and 10 microns (d).

From the experimental decay, by fitting to the Fourier temperature response at the surface from Eq. (3.23), we can fit to find the effective thermal conductivity. These fits are shown in Fig. 3-9 as well as the comparison to the forward calculation from the variational approach.

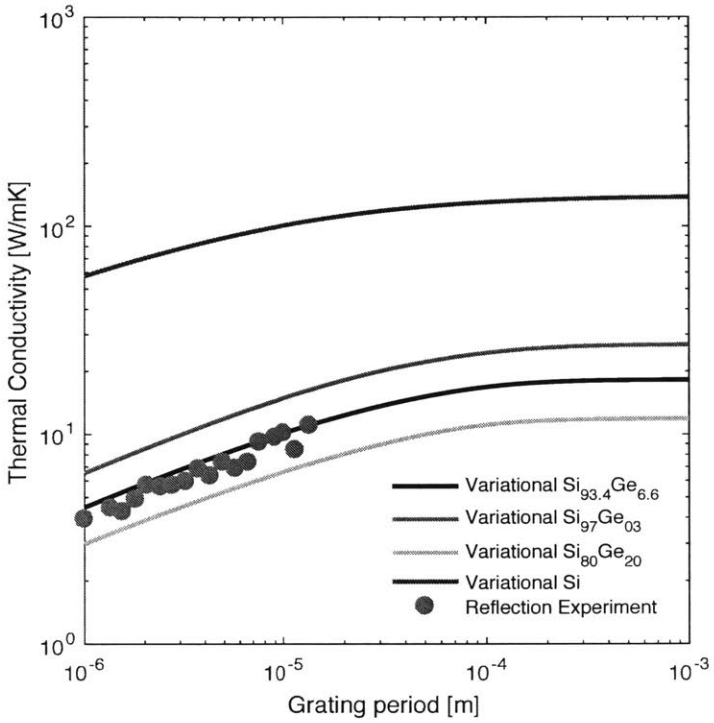

FIG. 3-9. Effective thermal conductivities extracted from reflection mode TTG experiment on SiGe. The comparison to the variational effective thermal conductivity shows excellent agreement. The experiment (green circles) shows excellent agreement with the variational for the sample of $Si_{93.4}Ge_{6.6}$, and the curves for other allows for SiGe are shown to demonstrate the sensitivity of the accuracy for the particular alloy tested.

We see excellent agreement between the fitted effective thermal conductivities as well as the results from a forward calculation utilizing the variational approach. Other alloys similar to the alloy utilized in the experiment are also shown to demonstrate the sensitivity to be able to capture the effective conductivities of a particular sample of SiGe.

This demonstrates the success of the variational approach, and Fig. 3-10 shows the progress of the modeling approach over the years for the case of 1 micron grating period. The MFP accumulation approach is one that cuts down the MFP of phonons larger than the geometrical length scale down to the experimental value. Thus this is a crude model which captures qualitatively the effect that the MFP of phonons is suppressed due to the geometry with just a simple Heaviside function cutoff. The next level sophistication was the gray suppression function model, which assumed that a suppression function existed, and that the thermal conductivity only depended on the accumulation of thermal conductivity. By solving the BTE assuming phonons only have a single MFP, and then adding up their contribution, the effective thermal conductivity is calculated. The variational approach developed here is now the most sophisticated approach and captures the output of experiment with the full phonon spectrum included.

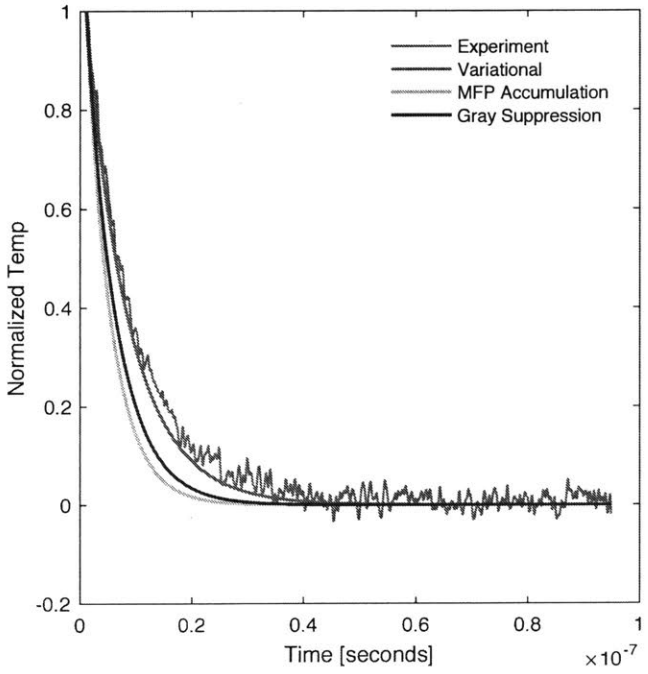

FIG. 3-10. Progression of modeling efforts to capture nondiffusive temperature response. The progression shows the increasingly more sophisticated models, starting from the MFP accumulation model, then the gray suppression function approach, and finally the current variational approach for a 1 micron grating period.

3.6 Summary

In this chapter, we have demonstrated the ability of the variational method to solve a multi-dimensional, transient heat transfer configuration over a broad range of length scales. We solved the BTE to yield the spectral energy density as a functional of the temperature in the thin film TTG geometry. By utilizing a trial solution obtained from the Fourier heat conduction model with the effective thermal conductivity treated as a variational parameter, and imposing an energy conservation condition integrated over the membrane thickness and time, the effective thermal conductivity was obtained analytically. The variational method was shown to yield the expected limits in the large grating period case and large film thickness case, converging to the one-dimensional TTG result and Fuchs-Sondheimer formula, respectively. The variational approach demonstrates a simple and direct method for obtaining an approximate solution to the BTE resulting in an accurate, analytical formula for the temperature profile, thermal decay rate, and the corresponding effective thermal conductivity.

The results of this work further enhance the understanding of nondiffusive transport in the context of temperature decay within geometries comparable to the MFP of the materials studied. Furthermore, it demonstrates the ability of the variational method beyond simple one-dimensional geometries, and the variational approach can suitably be applied to other problems involving nondiffusive phonon-mediated heat transport in nanostructures. We provide a complete expression for the thermal conductivity that shows its full dependence on the material properties and the geometry of the system. The analytical form provided gives the ability to study a wide variety of materials efficiently in order to better understand nondiffusive transport, in both the transmission mode and reflection mode configurations of the TTG. The work of this chapter also demonstrated that not all length scales result in size effects in the same way. The thin film thickness in transmission mode TTG and the optical penetration depth in reflection mode TTG provided very different effects on the effective thermal conductivity, and the ability to accurate model these configurations with the variational approach allows for such physical insight.

Chapter 4
MFP Reconstruction

In the previous two chapters, we demonstrated the capabilities of the variational approach to solving the BTE in obtaining effective thermal conductivities for the TTG geometry in its various configurations. We showed the accuracy of these analytical effective conductivities, and more importantly, the deviation from the idea of a universal suppression function to characterize thermal transport. This poses a difficulty for MFP reconstruction, as the previous algorithms were engineered with a universal suppression function in mind, where the dependence of the thermal transport on the geometry was only through the ratio of the MFP to the particular length scale. Thus, we have shown that the accumulation of thermal conductivity alone is not enough to characterize nondiffusive thermal transport in experiments with heating. We will show in this chapter that for the case of heating which results in a thermal distribution for the phonons, one must also include the accumulation of specific heat. This finding significantly impacts the fundamental understanding of how phonon spectral properties affect macroscopic transport properties. We provide an extended algorithm that aims to simultaneously reconstruct the thermal conductivity and heat capacity accumulation functions. While the simultaneous reconstruction requires more work to become readily applied to reconstruct materials for which experimental data is available on its effective thermal conductivity, it is a step forward to a more complete characterization of the material properties that affect thermal transport.

4.1 MFP reconstruction and the accumulation of thermal conductivity

The ability to control a length scale experimentally and probe thermal transport at different orders of magnitude provides a spectroscopy tool for studying nondiffusive thermal transport. The introduction of an algorithm [37] to solve the inverse problem of obtaining mean free path (MFP) properties of a material given experimental measurements provided an alternative

technique for the study and characterization of materials for which numerical studies may be too computationally intensive [41,74]. The major assumption behind the algorithm has been that the theorist must provide a universal suppression function that characterizes the effects of the geometry of the heat transfer configuration. However, the assumption of a universal suppression function has been shown to be flawed as we explained in chapter 2, and with a numerical study showing the inaccuracy of utilizing a gray suppression function in characterizing the temperature decay in the TTG [52], and more recently with an analytical expression of the effective thermal conductivity from which a universal suppression function cannot be extracted [64,65]. Thus, this warrants a need to extend the algorithm to be able to accurately obtain MFP properties of the system. Furthermore, the current algorithm is only able to reconstruct the thermal conductivity accumulation function [6], commonly deemed the MFP distribution [37], which is not sufficient to characterize nondiffusive thermal transport.

We first review the standard process for MFP reconstruction using the suppression function. The effective thermal conductivity is given by:

$$k = \frac{1}{3}\int C_\omega \mathrm{v}_\omega \Lambda_\omega S_\omega \, d\omega \tag{4.1}$$

where S_ω is the suppression function. The frequency integral actually contains a sum over branches and polarizations, embedded into the heat capacity, as it is proportional to the density of states. We utilize this simpler notation as opposed to cumbersome terms involving sums and integrals over frequencies of each branch in order to represent the integration over the full phonon dispersion. We can convert this to an integration over MFP's by utilizing a delta function as follows:

$$\begin{aligned} k &= \frac{1}{3}\int C_\omega \mathrm{v}_\omega \Lambda_\omega S_\omega \, d\omega \\ &= \frac{1}{3}\int C_\omega \mathrm{v}_\omega \Lambda_\omega S_\omega \int_0^\infty \delta(\Lambda - \Lambda_\omega) d\Lambda \, d\omega \\ &= \int_0^\infty \frac{1}{3}\int C_\omega \mathrm{v}_\omega \Lambda_\omega S_\omega \delta(\Lambda - \Lambda_\omega) d\omega \, d\Lambda \end{aligned} \tag{4.2}$$

This is very much so analogous to how we utilize a density of states to replace Brillouin zone integrations into a simple energy integration [75]. This is to replace the sum over all phonon modes into a simple one-dimensional integral over MFP values. For the standard algorithm, we essentially need a suppression function such that the suppression for a given phonon of a certain

branch and frequency only depends on that particular phonon's MFP. For now, we will consider the case where we have only experimental length scales, as it applies to the TTG, and leave the cases where one can have frequency scales (such as in TDTR/FDTR) for future work. If the suppression function is universal, i.e. $S_\omega = S\left(\Lambda_\omega / L_1, \Lambda_\omega / L_2 ...\right)$, where $L_1, L_2 ...$ are the length scales in the heat transfer configuration, and not dependent on the other MFP's of the system, then and only then can we simplify the integral we have into the form:

$$k\left(L_1, L_2 ...\right) = \int_0^\infty S\left(\frac{\Lambda}{L_1}, \frac{\Lambda}{L_2} ...\right) \frac{1}{3} \int C_\omega \mathrm{v}_\omega \Lambda_\omega \delta\left(\Lambda - \Lambda_\omega\right) d\omega d\Lambda \tag{4.3}$$

The length scales, $L_1, L_2 ...$, can be the grating period and film thickness in the TTG [16,20,65], the effective thermal penetration depth in TDTR/FDTR [24,25,31,44,76], to name a few examples. Utilizing the fact that the derivative of the step function, $\Theta\left(x\right)$, is equal to the Dirac delta function, $\delta\left(x\right)$, we obtain:

$$\begin{aligned}
k\left(L_1, L_2 ...\right) &= \int_0^\infty S\left(\frac{\Lambda}{L_1}, \frac{\Lambda}{L_2} ...\right) \frac{1}{3} \int C_\omega \mathrm{v}_\omega \Lambda_\omega \delta\left(\Lambda - \Lambda_\omega\right) d\omega d\Lambda \\
&= \int_0^\infty S\left(\frac{\Lambda}{L_1}, \frac{\Lambda}{L_2} ...\right) \frac{d}{d\Lambda} \frac{1}{3} \int C_\omega \mathrm{v}_\omega \Lambda_\omega \Theta\left(\Lambda - \Lambda_\omega\right) d\omega d\Lambda \\
&= S\left(\frac{\Lambda}{L_1}, \frac{\Lambda}{L_2} ...\right) \frac{1}{3} \int C_\omega \mathrm{v}_\omega \Lambda_\omega \Theta\left(\Lambda - \Lambda_\omega\right) d\omega \Big|_{\Lambda=0}^{\Lambda \to \infty} + \\
&\quad - \int_0^\infty \left[\frac{1}{3} \int C_\omega \mathrm{v}_\omega \Lambda_\omega \Theta\left(\Lambda - \Lambda_\omega\right) d\omega\right] \frac{d}{d\Lambda} S\left(\frac{\Lambda}{L_1}, \frac{\Lambda}{L_2} ...\right) d\Lambda \\
k\left(L_1, L_2 ...\right) &= - \int_0^\infty k_{acc}\left(\Lambda\right) \frac{d}{d\Lambda} S\left(\frac{\Lambda}{L_1}, \frac{\Lambda}{L_2} ...\right) d\Lambda
\end{aligned} \tag{4.4}$$

where we have performed an integration by parts and utilized the fact that the suppression function for very short length scales of the system (or very large MFP) is zero, and we have defined the thermal conductivity accumulation function $k_{acc}\left(\Lambda\right) \equiv \frac{1}{3} \int C_\omega \mathrm{v}_\omega \Lambda_\omega \Theta\left(\Lambda - \Lambda_\omega\right) d\omega$. This expression using the Heaviside step function Θ is the same as that provided by Eq. (4) and Eq. (5) of Ref. [36] in the sense that it counts the contribution of phonons to thermal conductivity that have MFP less than a cutoff MFP, but the expressions used in Ref. [36] utilize a derivative of the MFP with respect to frequency and require a continuous functional form or will yield

numerical errors for the derivative if the frequency mesh is broad, whereas the Heaviside step function allows for a more general mathematical expression which is valid for a discrete mesh or for a continuous frequency functional form for the material properties. However, the first approach taken to do this conversion utilized this derivative of the MFP and transformation [6,35,36], and we formalize the mathematics here to generalize the conversion.

Due to the functional form of the accumulation function, at zero argument, the accumulation function is zero, and at infinite argument, it recovers the bulk thermal conductivity. Clearly, the thermal conductivity accumulation function is a monotonically increasing function due to the property of the step function. If we discretize the system MFP values, and since we have a finite number of experimental measurements, the integral equation given by Eq. (4.4) can be written as a matrix equation, where the thermal conductivity values are a given vector, the suppression function will be a matrix which takes the vector of thermal conductivity accumulation values and maps it to the experimental values. Since the number of experimental measurements does not necessarily equal the number of MFP values we discretize, this is a non-square matrix we need to 'invert' in order to get the thermal conductivity accumulation, and thus this is an ill-posed linear algebra problem. The thermal conductivity accumulation function can be determined by utilizing the thermal conductivity extracted from experiment and the derivative of the suppression function obtained from modeling and doing linear algebra optimization to find the thermal conductivity accumulation which best satisfies the matrix equation. Note that one does not need to keep one length scale fixed and vary the other, in fact one could take an arbitrary set of data points for various length scales, so long as the length scales are small enough to probe into the nondiffusive transport regime, the thermal conductivity accumulation function can be extracted from the reconstruction algorithm [29].

In the context of the TTG, previously a suppression function for the one-dimensional limit was derived [18] by Maznev *et al.* and is of the form for the two-fluid model:

$$S_{\text{two-fluid}}(\eta_\omega) = \frac{3}{\eta_\omega^2}\left[1 - \frac{\arctan(\eta_\omega)}{\eta_\omega}\right] \tag{4.5}$$

where we use the non-dimensional number $\eta_\omega = 2\pi\Lambda_\omega / \lambda$. This suppression function was utilized for reconstruction as it satisfies the requirements for use within the algorithm [37]. So we will use numerical procedures to solve the inverse problem and obtain the material properties from Eq. (4.4) given thermal conductivity measurements and the suppression function shown.

Deriving similarly for the variational function, a deeper look at the effective thermal conductivity expression from the variational approach reveals a new aspect of the physics of transport in the nondiffusive regime. We reproduce Eq. (3.36) from Chapter 3 here, which provides the effective thermal conductivity in the TTG geometry:

$$k = \frac{\frac{1}{3}\int d\omega C_\omega \mathrm{v}_\omega \Lambda_\omega f(\eta_\omega, \mathrm{Kn}_\omega)}{\frac{1}{C}\int d\omega C_\omega g(\eta_\omega, \mathrm{Kn}_\omega)} \tag{4.6}$$

The effective thermal conductivity expression of Eq. (4.6) contains a numerator term that depends on the differential thermal conductivity, and a geometric kernel that depends on the ratio of the MFP to the grating period and also to the film thickness. Notably, the denominator integral depends on the differential heat capacity, and a geometric kernel that depends again on the ratio of MFP to grating period and to the film thickness. The kernels f and g are given by the forms we provided in Chapter 3 for the particular cases of the thin film TTG operated in transmission mode as well as in reflection mode.

This demonstrates that the accumulation of thermal conductivity, which has been deemed the 'MFP distribution' in literature [37,48], is not sufficient to characterize the material property dependence of transport in transient configurations. If we convert the frequency integration into MFP integration, we obtain:

$$k = \frac{\int_0^\infty k_{acc}(\Lambda)\frac{d}{d\Lambda} f(\eta, \mathrm{Kn}) d\Lambda}{\frac{1}{C}\int_0^\infty C_{acc}(\Lambda)\frac{d}{d\Lambda} g(\eta, \mathrm{Kn}) d\Lambda} \tag{4.7}$$

The accumulation of thermal conductivity and heat capacity are expressed mathematically as $k_{acc}(\Lambda) = \frac{1}{3}\int d\omega C_\omega \mathrm{v}_\omega \Lambda_\omega \Theta(\Lambda - \Lambda_\omega)$ and $C_{acc}(\Lambda) = \int d\omega C_\omega \Theta(\Lambda - \Lambda_\omega)$ where the Heaviside step function Θ is utilized to only include contributions from MFPs below the given value Λ. When normalized by the bulk thermal conductivity and total volumetric heat capacity respectively, these functions are cumulative distribution functions that rise from the value of 0 to 1 monotonically with increasing MFP. Equation (4.7) reveals the dependence of the effective thermal conductivity on the accumulation of thermal conductivity, and now also on the accumulation of heat capacity. This has important consequences for our understanding of the dependence of transport on a material's intrinsic properties.

In theory, one could imagine two separate materials with identical accumulation of thermal conductivity, but different accumulation of heat capacity, and the output from experiments or numerical simulations utilizing these two materials would be different in transient systems. The variational method has demonstrated that in order to understand how a phonon contributes to the output of any transient thermal transport measurement, we need to understand the contribution of that phonon to both the thermal conductivity and the heat capacity. This also highlights the importance of solving the spectral BTE, as opposed to the gray BTE. In the gray BTE solution, the heat capacity accumulation would not appear as the assumption of a single MFP would allow the kernels f and g to be taken out of the spectral integration, and thus the gray solution to the BTE would not capture the physics of the accumulation of heat capacity.

To demonstrate the importance of the denominator term, we demonstrate reconstruction using the standard algorithm as well as with the knowledge of the denominator term to reconstructing the thermal conductivity accumulation function. We can shift our equation by multiplying by the denominator to obtain:

$$0=\int_0^\infty \kappa_{acc}(\Lambda)\frac{d}{d\Lambda}f\left(\eta=\frac{2\pi\Lambda}{\lambda},\mathrm{Kn}=\frac{\Lambda}{d}\right)d\Lambda-\kappa(\lambda,d)\int_0^\infty \chi_{acc}(\Lambda)\frac{d}{d\Lambda}g\left(\eta=\frac{2\pi\Lambda}{\lambda},\mathrm{Kn}=\frac{\Lambda}{d}\right)d\Lambda \tag{4.8}$$

where we use κ to denote thermal conductivity normalized to its bulk value and χ_{acc} to denote the normalized accumulated heat capacity. In discretized form, we can define the following matrices and vectors:

$$\begin{aligned}
A_{n,j} &= w_j\left[\frac{d}{d\Lambda}f\left(\eta=\frac{2\pi\Lambda}{\lambda_n},\mathrm{Kn}=\frac{\Lambda}{d_n}\right)\right]\Bigg|_{\Lambda=\Lambda_j}\\
B_{n,j} &= w_j\kappa(\lambda_n,d_n)\left[\frac{d}{d\Lambda}g\left(\eta=\frac{2\pi\Lambda}{\lambda_n},\mathrm{Kn}=\frac{\Lambda}{d_n}\right)\right]\Bigg|_{\Lambda=\Lambda_j}\\
\left[\vec{\kappa}_{acc}\right]_j &= \kappa_{acc}(\Lambda_j)\\
\left[\vec{\chi}_{acc}\right]_j &= \chi_{xx}(\Lambda_j)
\end{aligned} \tag{4.9}$$

where the values w describe integration weights. Now this becomes a linear optimization problem where we seek to minimize the penalty function:

$$P=\left|A\vec{\kappa}_{acc}-B\vec{\chi}_{acc}\right|^2+c_1\left|\Delta^2\vec{\kappa}_{acc}\right|^2+c_2\left|\Delta^2\vec{\chi}_{acc}\right|^2 \tag{4.10}$$

where it is now very much so analogous to the previous reconstruction algorithm [37]. In the previous reconstruction algorithm, the only difference is that there is no accumulation of thermal

conductivity term, and so the term with the matrix B is given by the experiment. Also we can impose other inequality constraints where we limit the jump that can occur between adjacent values so that this linear version of the problem is now solved for functions that are simply zero and then at the end jump up to unity. The coefficients c_1, c_2 are the weights we give to smoothness for the thermal conductivity accumulation function and the heat capacity accumulation function given in terms of their numerical second derivatives, and the minimization is done in the least squares fashion for the error.

Figure 4-1 shows the capabilities of reconstructing the thermal conductivity accumulation with the previous algorithm which utilizes the suppression function. Clearly, with knowledge of experimental measurements down to 100nm as opposed to only 1 micron, the accuracy of the reconstruction improves, especially for shorter MFP values.

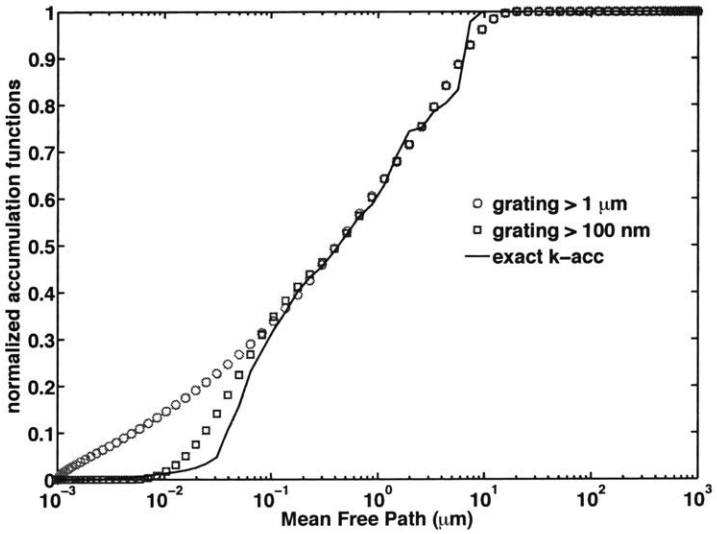

FIG. 4-1. Reconstruction of the thermal conductivity accumulation with a suppression function, using synthetic experimental data down to 1 micron, and down to 100 nm to demonstrate the importance of having short grating periods to perform accurate reconstruction.

In Fig. 4-2, we show the output of reconstructing the thermal conductivity accumulation function with the same convex optimization, but assuming that the heat capacity accumulation is a known

function. This highlights the importance of having the denominator term in the effective thermal conductivity.

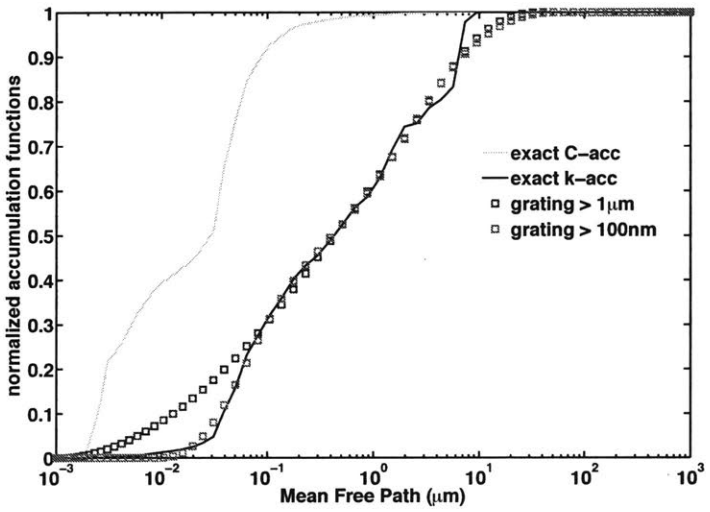

FIG. 4-2. Reconstruction of thermal conductivity accumulation with given heat capacity accumulation. Data is shown again for using synthetic experimental input down to 1 micron as well as down to 100 nm to show the importance of having short grating periods to reconstruct small MFP values of the accumulation function.

We note that with a single micron value of grating periods and higher, the improvement from knowing the heat capacity accumulation is negligible, as can be seen by comparing Fig. 4-1 and Fig. 4-2. This is due to the fact that the variation of the heat capacity accumulation for silicon occurs between 1 and 100 nm. For grating periods of 100nm and higher, we see that the reconstruction of the thermal conductivity accumulation is greatly improved for the shorter MFPs with the knowledge of the heat capacity accumulation, and is more accurately capturing the lower MFP values than the standard algorithm with the suppression function. This demonstrates the improvement offered by the variational effective conductivity.

The difficulty with implementing this generally to study a wide variety of materials is that we require an exact knowledge of the denominator, or at least an initial guess. If we have exact knowledge of the denominator, then we must know already the MFP's of the system, which makes the reconstruction process unnecessary to begin with. If we have an approximate value

for the function in the denominator based on some initial guess of the MFP's, then we can input the suppression function into the standard linear convex reconstruction algorithm and obtain the thermal conductivity accumulation function. The problem with this is that then we do not have a method of iteration! The thermal conductivity accumulation function does not give us the MFP's of the system, and they furthermore will not be able to give us a corrected guess for the denominator. Thus an iterative approach is not a logical approach in this case. Therefore the heat capacity accumulation will also require solving for, just like for the thermal conductivity accumulation function.

4.2 Simultaneous reconstruction of the thermal conductivity accumulation and heat capacity accumulation

Given measurements from the TTG measurement, the goal is to simultaneously reconstruct the accumulation of thermal conductivity and specific heat. The form of Eq. (4.7) has the heat capacity accumulation appearing in a nonlinear form due to its appearance in the denominator. There are various ways to numerically attack this inverse problem, and a nonlinear, non-convex simultaneous optimization can be performed. For simplicity, we instead proceed by recasting the problem into a linear optimization form, by first multiplying the denominator over to the other side. This is a functional equation, for which we have the kernels of the integrals analytically. As there are two functions to reconstruct, we aim to generate two discretized equations for solving. With only a single equation, the discretization has truncated the information content that the full functional form has, such as its derivatives and higher order details of shape between points. By utilizing the derivative of the equation with respect to the grating period, we generate a second equation containing information of the rate of increase of the effective conductivity. Numerically, we have:

$$\begin{aligned} 0 &= \int_0^\infty \kappa_{acc}(\Lambda)\left[\frac{\partial}{\partial\Lambda} f\left(\frac{2\pi\Lambda}{\lambda},\frac{\Lambda}{d}\right)\right]d\Lambda - \int_0^\infty \chi_{acc}(\Lambda)\left[\kappa(\lambda,d)\frac{\partial}{\partial\Lambda} g\left(\frac{2\pi\Lambda}{\lambda},\frac{\Lambda}{d}\right)\right]d\Lambda \\ 0 &= \int_0^\infty \kappa_{acc}(\Lambda)\left[\frac{\partial}{\partial\lambda}\frac{\partial}{\partial\Lambda} f\left(\frac{2\pi\Lambda}{\lambda},\frac{\Lambda}{d}\right)\right]d\Lambda - \int_0^\infty \chi_{acc}(\Lambda)\frac{\partial}{\partial\lambda}\left[\kappa(\lambda,d)\frac{\partial}{\partial\Lambda} g\left(\frac{2\pi\Lambda}{\lambda},\frac{\Lambda}{d}\right)\right]d\Lambda \end{aligned} \tag{4.11}$$

where κ_{acc} and χ_{acc} are the thermal conductivity and heat capacity accumulation functions normalized by their respective bulk values. The derivative of the effective conductivity also has physical meaning. With an incremental change in the grating period, it looks at the corresponding change in the effective conductivity, thus capturing how phonons that begin to experience size effects at that grating period change in their contribution to the effective transport. The one difficulty with this linear reconstruction approach is that in casting the nonlinear problem as a linear one, there is the introduction of the trivial zero solution. There are still the same constraints placed on the accumulation functions [37], in that it must be monotonically increasing, but in the initial attempts at reconstruction, the solutions demonstrated a strong pull towards the zero solution while still maintaining the constraints as best as possible. To alleviate this, the reconstruction is done in two steps. In the first step, the reconstruction is done utilizing the large grating period limit where the denominator of Eq. (4.6) approaches unity faster than the numerator approaches the bulk thermal conductivity. Thus a suppression function given by the kernel of the numerator, f of Eq. (4.6), can be utilized as a first pass using the previous algorithm [37]. The reconstruction in this case will be valid for larger MFPs, but the accuracy drops for shorter MFPs for which the large grating approximation was taken. Alternatively, one could also take a suppression function obtained from a gray solution, where by taking the gray limit of Eq. (4.6), the suppression function that is identified is $S_\omega = f(\eta_\omega, \mathrm{Kn}_\omega)/g(\eta_\omega, \mathrm{Kn}_\omega)$. The exact approach taken is not important, what is important is that there is a first pass solution in order to get a sufficiently accurate result for at least the larger MFPs for the accumulation of thermal conductivity. Arguably for systems with a smaller range of MFPs, a gray suppression function approach would be more accurate. In our approach, we took the case of the suppression function as the kernel of the numerator as this is rigorously accurate in the large grating period limit, and we found the gray approach provided very poor reconstruction results for the accumulation of thermal conductivity for silicon as it has a broad range of MFPs. In the second pass through, the higher MFPs for the accumulation of thermal conductivity are left fixed, and the simultaneous reconstruction is performed for the accumulation of heat capacity and the lower portion of MFPs for the accumulation of thermal conductivity. The penalty function we take in this case is:

$$P = \left\| \begin{bmatrix} A & -B \\ C & -D \end{bmatrix} \begin{bmatrix} \vec{x} \\ \vec{y} \end{bmatrix} \right\|^2 + c_1 \left|\Delta^2 \vec{x}\right|^2 + c_2 \left|\Delta^2 \vec{y}\right|^2$$

$$x_j = \kappa_{acc}\left(\Lambda_j\right) \qquad y_j = \chi_{acc}\left(\Lambda_j\right)$$

$$A_{n,j} = -w_j \left[\frac{\partial}{\partial \Lambda} f\right]_{\substack{\lambda=\lambda_n \\ d=d_n \\ \Lambda=\Lambda_j}} \qquad B_{n,j} = -w_j \left[\kappa(\lambda,d)\frac{\partial}{\partial \Lambda} g\right]_{\substack{\lambda=\lambda_n \\ d=d_n \\ \Lambda=\Lambda_j}} \tag{4.12}$$

$$C_{n,j} = -w_j \left[\frac{\partial}{\partial \lambda}\frac{\partial}{\partial \Lambda} f\right]_{\substack{\lambda=\lambda_n \\ d=d_n \\ \Lambda=\Lambda_j}} \qquad D_{n,j} = -w_j \frac{\partial}{\partial \lambda}\left[\kappa(\lambda,d)\frac{\partial}{\partial \Lambda} g\right]_{\substack{\lambda=\lambda_n \\ d=d_n \\ \Lambda=\Lambda_j}}$$

Similar to the previous algorithm [37], smoothness is implemented by adding terms to the penalty function that aim to minimize the second derivative of the accumulation functions. The weights w_j appear due to the discretization of the integrals, and we utilize Gauss-Legendre quadrature. If one has a very accurate scheme for performing reconstruction of the thermal conductivity over the whole MFP range, then the reconstruction of heat capacity need only be performed with the input of the thermal conductivity accumulation from the previous pass, however neither the gray approximation nor the large grating approximation are capable of achieving this in general. Either way, once a first pass where the partial solution of the accumulation of thermal conductivity exists, the linear simultaneous reconstruction can be performed as the trivial zero solution is no longer outputted when one utilizes the partial solution of the higher MFPS of the thermal conductivity accumulation function as a constraint.

In order to achieve a successful reconstruction of the accumulation functions, experimental data is needed for short enough grating periods in order to probe the short MFPs that contribute to transport. As the heat capacity accumulation contribution comes from MFPs that are even shorter than the dominant MFPs that contribute to thermal conductivity, there is a need for even shorter grating periods. With recent extreme ultra violet (EUV) measurements, the possibility to reach grating periods down to 10 nm is achievable [77,78]. Utilizing the two-step reconstruction process outlined previously, we performed reconstruction for silicon as a test material. The data used to perform reconstruction is synthetic experimental data, generated by a forward calculation utilizing the variational method. As the variational method has demonstrated success in the forward calculation against exact Monte Carlo (MC) simulations [65], we utilize it here to generate effective thermal conductivities, inputting DFT-obtained silicon material properties

[64]. This allows us to test the capabilities of the reconstruction process itself without unknowns from experimental data and other uncertainties. We varied the number of measurements, and the grating periods utilized in the measurements to understand the sensitivity of the reconstruction to these parameters. We found that the reconstruction required small enough grating periods to be sensitive to reconstruct the accumulation functions for low MFPs. We also found that with 20 – 30 measurements, the reconstruction procedure was successful, but with too few measurements, again the sensitivity to reconstructing MFPs accurately over the broad range of 1 nm to 1000 micron was difficult. With a larger number of measurements, the results of the reconstruction shows negligible further improvement. Figure 4-3 shows the reconstruction process performed in two steps. The markers are the reconstructed material properties, while the solid lines are the reference DFT derived material properties to compare against. Here we assume having forward calculation effective thermal conductivities from 20 different gratings spaced logarithmically from 10nm up to 10 microns. The first pass through reconstruction with the suppression function shows good agreement for MFPs of around 100 nm and above, but shows inaccuracy at shorter MFPs. We note that the sharp feature around 10 nm is not reconstructed very well due to difficulties in reconstructing rapidly changing functions. The same sharp changes in the accumulation of heat capacity pose difficulty for the current method of dealing with smoothness in the algorithm. However, we see that the methodology does show promise in recovering the heat capacity accumulation, and shows improvement over the original scheme in the accuracy of the thermal conductivity accumulation for short MFPs. These results are in the large thickness limit where the one-dimensional limit of the TTG is achieved for simplicity, but the algorithm shown applies in general to the thin film TTG geometry.

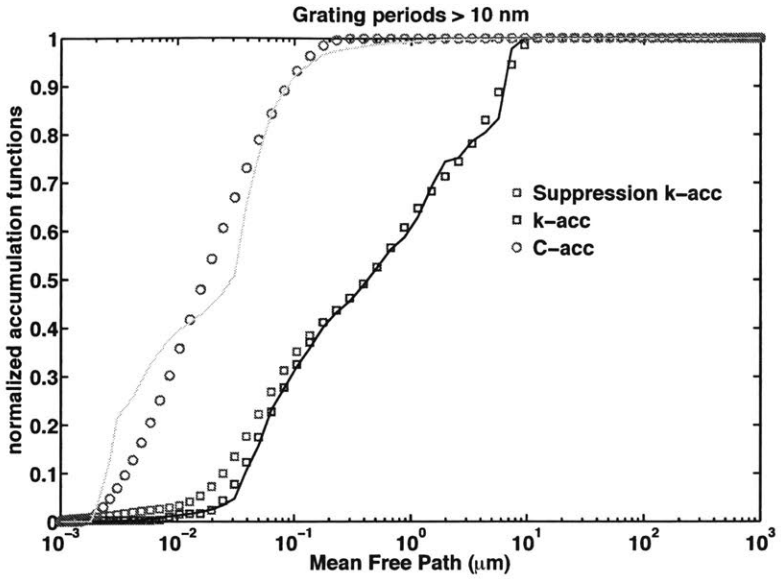

FIG. 4-3. Reconstruction of the accumulation of thermal conductivity and heat capacity simultaneously using the 1D TTG variational model.

In the future, we can also perform reconstruction with data from a 390nm thick silicon film, similar to the conditions of the experiment measured previously for silicon [16]. This is to demonstrate that the reconstruction process can be done with the full thin film geometry considered. The kernels in the thin film case [65] are generated numerically by calculating the necessary solid angle integrals using Gauss-Legendre quadrature. Of course we expect the exact same material properties to be reconstructed even if the configuration is different, but this extends the ability to do reconstruction beyond the simple one-dimensional transport limit and can handle cases closer to what is physically the case in the TTG experiment.

In summary, we have illuminated the physics of transport in transient heat transfer configurations with the new appearance of the accumulation of heat capacity, along with the known appearance of the accumulation of thermal conductivity. The analytical formula provided by the variational method has revealed not only this appearance, but also the opportunity for reconstruction of these two accumulation functions simultaneously. We have given a preliminary demonstration of reconstruction for silicon, which shows promising results in recovering both accumulation functions. We utilize the same linear, convex optimization routine

but use a two step process in order to simultaneously reconstruct the accumulation functions that uniquely characterize a material's transport in the nondiffusive regime. For those interested only in the reconstruction of thermal conductivity, the algorithm provides an improvement as the simultaneous reconstruction utilizes a formula valid much further into the nondiffusive regime than the traditional suppression function based approach.

4.3 Basis functions to achieve smoother reconstruction

A next step in improving the algorithm is enhancing its ability to deal with smoothness of the functions to not only boost efficiency of the algorithm but also deal with sharp kinks in the points. We can recast the integrals in terms of a basis rather than a direct discretization to deal with these smoothness conditions. Furthermore, with this current success of the algorithm, the opportunity will open up for reconstruction using experimental data from extreme ultra violet (EUV) measurements in TTG as the shortest grating periods achievable get pushed down to even lower spacings. The methodology outlined here can be applied to extract material property data using experimental measurements for materials for which numerical calculations of the properties are intractable.

Now let us go through the details of the standard reconstruction process [37], with the new approach of utilizing a basis as opposed to numerical discretization. For the 1D TTG, we have that $S_\omega = S(\eta_\omega)$ where $\eta_\omega = 2\pi\Lambda_\omega / \lambda$ and λ is the grating period. Utilizing the conversion from the phonon spectrum integration to MFP integration, we obtain:

$$\kappa(\lambda) = -\frac{2\pi}{\lambda}\int_0^\infty d\Lambda \kappa_{acc}(\Lambda) S'(\eta) \tag{4.13}$$

where we have normalized the effective and also accumulative conductivities by the bulk, $\kappa = k / k_b$. Previously, the linear problem is solved by discretizing the integral, and minimizing the error of the equation over those discrete values [37]. Constraints are imposed in order to ensure the accumulation function is monotonically increasing, and also a penalty is added to the objective function in order to ensure smoothness. However, the smoothing parameter has typically been treated like a fitting parameter, where it is tuned in order to avoid sharply varying

accumulation functions and also to best solve the equation. We seek to avoid this crude approach, as picking the smoothing parameter is difficult, especially given a material for which the accumulation of thermal conductivity is not a priori already known (i.e. through DFT). We choose to expand in terms of a polynomial basis in the logarithm of the MFP. Given that there is a minimum MFP Λ_1 and a maximum MFP Λ_2 in the system, we make the change of variables $\Lambda = \Lambda_1 \left(\frac{\Lambda_2}{\Lambda_1}\right)^y$ to rewrite the MFP as an exponential function of a non-dimensional variable y which only runs from 0 to 1, and expand the accumulation function as a polynomial in y. Doing this change of variables yields:

$$\kappa(\lambda) = -\frac{2\pi}{\lambda}\int_0^1 dy\, \kappa_{acc}\left(\Lambda = \Lambda_1\left(\frac{\Lambda_2}{\Lambda_1}\right)^y\right)\left\{\ln\left(\frac{\Lambda_2}{\Lambda_1}\right)\Lambda_1\left(\frac{\Lambda_2}{\Lambda_1}\right)^y S'\left(\eta = \frac{2\pi}{\lambda}\Lambda_1\left(\frac{\Lambda_2}{\Lambda_1}\right)^y\right)\right\} \quad (4.14)$$

The natural logarithm term has appeared due to the transformation of the integral in terms of Λ to y and the derivative of the exponential. Expanding the accumulation function as a polynomial of degree N, we have:

$$\kappa_{acc}\left(\Lambda = \Lambda_1\left(\frac{\Lambda_2}{\Lambda_1}\right)^y\right) = y^N + \sum_{n=1}^{N-1} a_n\left(y^n - y^N\right) \quad (4.15)$$

This polynomial starts at zero when y = 0, and equals unity when y = 1. Inserting this polynomial equation, we can now define a penalty function that we want to minimize over the m number of experimental measurements:

$$\begin{aligned} P &= \left|\vec{b} - A\vec{a}\right|^2 \\ b_j &= \kappa(\lambda_j) + \int_0^1 dy y^N \ln\left(\frac{\Lambda_2}{\Lambda_1}\right)\eta S'(\eta) \quad , j \in [m] \\ A_{j,n} &= -\int_0^1 dy\left(y^n - y^N\right)\ln\left(\frac{\Lambda_2}{\Lambda_1}\right)\eta S'(\eta) \quad , j \in [m], n \in [N-1] \end{aligned} \quad (4.16)$$

where we use $\eta = \frac{2\pi}{\lambda_j}\Lambda_1\left(\frac{\Lambda_2}{\Lambda_1}\right)^y$ for short-hand notation, and we impose the following constraints to require the function be monotonically increasing:

$$N\left(y_j\right)^{N-1}+\sum_{n=1}^{N-1}a_n\left(ny_j^{n-1}-Ny_j^{N-1}\right)\geq 0$$
$$y_j=\frac{j}{N_D+1}\ ,\ j\in\left[N_D\right] \tag{4.17}$$

The value N_D is the number of inequality constraints we choose to impose in order to ensure the polynomial expansion does not turn over and make the accumulation function decreasing over any of the MFP values. This particular problem is well suited for convex optimization.

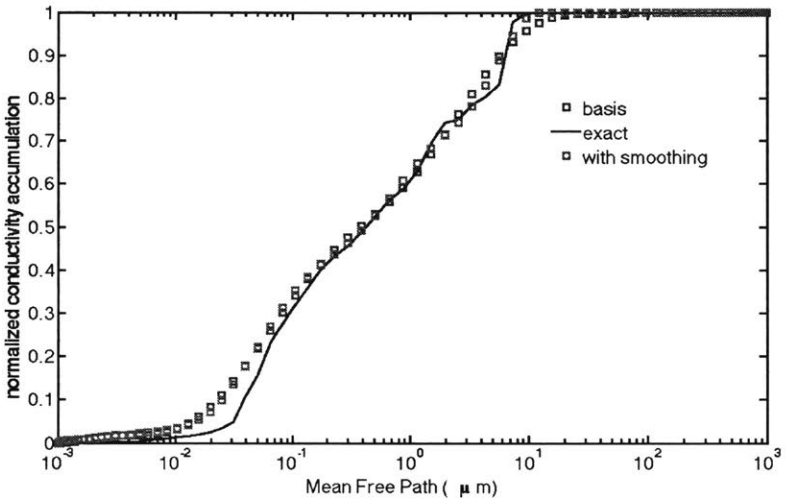

FIG. 4-4. The reconstruction for silicon's accumulation of thermal conductivity with a basis expansion. We assumed 30 synthetic experimental values of the effective thermal conductivity from 10nm to 100 microns. This is at the optimal limits of what we are capable of experimentally to see how well the reconstruction can perform under the best of conditions. This is for the standard reconstruction with a suppression function.

Going through and utilizing the convex optimization algorithm in Matlab, we see the reconstruction performs identically well compared to the previous method with a smoothing parameter. However, this time, there is no need to tune a smoothing parameter to achieve satisfactory results. We simply increase the number of terms in the basis expansion until we see convergence for the reconstruction output. The integrals in y are done utilizing Gauss quadrature and the suppression function of:

$$S(\eta)=\frac{3}{\eta^2}\left[1-\frac{\arctan(\eta)}{\eta}\right] \tag{4.18}$$

The results shown are in particular for the following parameter values:

$$\begin{aligned} N &= 40 \\ N_D &= 400 \\ N_I &= 200 \end{aligned} \tag{4.19}$$

The last value is the number of points we utilize in the Gauss quadrature. Note the derivative constraint number and the integration number are larger than necessary to be safely convergent for the integral and to avoid non-monotonic behavior. The value N was increased from 5 up until 60 at which point less than 1% variation was observed.

Since we have confidence this can work with the old algorithm with a suppression function as we compared against the previous discretized procedure [37], we can apply the same polynomial basis approach for the variational TTG to extend this algorithm as well to avoiding the smoothing parameter the discretization procedure utilizes. The effective thermal conductivity for the 1D TTG geometry was given by the variational method:

$$k(\lambda)=\frac{\frac{1}{3}\int \omega \ {}_{\omega}\mathrm{v}_{\omega}\Lambda_{\omega} \ (\eta_{\omega})}{\frac{1}{C}\int d\omega C_{\omega} g(\eta_{\omega})} \tag{4.20}$$

where $\eta_{\omega}=2\pi\Lambda_{\omega}/\lambda$ and the kernel functions are:

$$\begin{aligned} f(\eta) &= \frac{3}{\eta^2}\left[1-\frac{\arctan(\eta)}{\eta}\right] \\ g(\eta) &= \frac{\arctan(\eta)}{\eta} \end{aligned} \tag{4.21}$$

The goal is to set up similarly a penalty function with suitable constraints on the coefficients of the basis expansion so that the accumulation functions are monotonically increasing. First, converting the phonon spectrum summations into MFP integrations, we obtain:

$$\kappa(\lambda)=\frac{\int_0^{\infty} d\Lambda \kappa_{acc}(\Lambda) f'(\eta)}{\int_0^{\infty} d\Lambda \chi_{acc}(\Lambda) g'(\eta)} \tag{4.22}$$

where the accumulation functions are given by:

$$\kappa_{acc}(\Lambda)=\frac{1}{k_b}\frac{1}{3}\int d\omega C_\omega v_\omega \Lambda_\omega \Theta(\Lambda-\Lambda_\omega)$$
$$\chi_{acc}(\Lambda)=\frac{1}{C}\int d\omega C_\omega \Theta(\Lambda-\Lambda_\omega) \tag{4.23}$$

where we have utilized the Heaviside step function in order to only count the contributions for phonons up to a given MFP. We again utilize a change of variable as $\Lambda=\Lambda_1\left(\frac{\Lambda_2}{\Lambda_1}\right)^y$, and the expansions of:

$$\kappa_{acc}\left(\Lambda=\Lambda_1\left(\frac{\Lambda_2}{\Lambda_1}\right)^y\right)=y^N+\sum_{n=1}^{N-1}a_n\left(y^n-y^N\right)$$
$$\chi_{acc}\left(\Lambda=\Lambda_1\left(\frac{\Lambda_2}{\Lambda_1}\right)^y\right)=y^N+\sum_{n=1}^{N-1}b_n\left(y^n-y^N\right) \tag{4.24}$$

with the inequality constraints:

$$Ny_j^{N-1}+\sum_{n=1}^{N-1}a_n\left[ny_j^{n-1}-Ny_j^{N-1}\right]\geq 0$$
$$Ny_j^{N-1}+\sum_{n=1}^{N-1}b_n\left[ny_j^{n-1}-Ny_j^{N-1}\right]\geq 0 \tag{4.25}$$
$$y_j=\frac{j}{N_D+1}\quad,\ j\in[N_D]$$

By inserting the basis expansion into the effective thermal conductivity expression, we obtain a penalty function:

$$P=\sum_{j=1}^{m}\left[\kappa(\lambda_j)-\frac{\int_0^1 dyy^N\eta f'(\eta)+\sum_{n=1}^{N-1}a_n\int_0^1 dy\left(y^n-y^N\right)\eta f'(\eta)}{\int_0^1 dyy^N\eta g'(\eta)+\sum_{n=1}^{N-1}b_n\int_0^1 dy\left(y^n-y^N\right)\eta g'(\eta)}\right]^2 \tag{4.26}$$

where I have used $\eta=\frac{2\pi}{\lambda_j}\Lambda_1\left(\frac{\Lambda_2}{\Lambda_1}\right)^y$ for short hand notation. This optimization will not longer be linear as the coefficients b appear in the denominator. If we were to multiply the denominator over, we could generate a linear problem, but the difficulty here is that the trivial solution of zero for the accumulation functions becomes a strong attractor compared to the true solutions given

the linearized form we created and introduced this extraneous solution. Thus we proceed with the nonlinear form in order to avoid such numerical difficulties.

We define the following matrices for simplification:

$$
\begin{aligned}
P &= \sum_{j=1}^{m}\left[\kappa(\lambda_j) - \frac{c_j + \sum_{n=1}^{N-1} a_n A_{j,n}}{d_j + \sum_{n=1}^{N-1} b_n B_{j,n}}\right]^2 \\
c_j &= -\int_0^1 dy y^N \eta f'(\eta) \\
d_j &= -\int_0^1 dy y^N \eta g'(\eta) \\
A_{j,n} &= -\int_0^1 dy\left(y^n - y^N\right)\eta f'(\eta) \\
B_{j,n} &= -\int_0^1 dy\left(y^n - y^N\right)\eta g'(\eta)
\end{aligned}
\tag{4.27}
$$

where I have used the short-hand notation of $\eta = \frac{2\pi}{\lambda_j}\Lambda_1\left(\frac{\Lambda_2}{\Lambda_1}\right)^y$. The inequality constraints from before are quoted here:

$$
\begin{aligned}
N y_j^{N-1} + \sum_{n=1}^{N-1} a_n\left[n y_j^{n-1} - N y_j^{N-1}\right] &\geq 0 \\
N y_j^{N-1} + \sum_{n=1}^{N-1} b_n\left[n y_j^{n-1} - N y_j^{N-1}\right] &\geq 0 \\
y_j = \frac{j}{N_D+1} \quad &, j \in [N_D]
\end{aligned}
\tag{4.28}
$$

While we do not yet have an algorithm that can handle the nonlinear nature of this reconstruction, this procedure has now allowed for a more efficient approach at reconstruction for the two accumulation functions. We no longer utilize discretized meshes and require picking the arbitrary smoothing parameter, and we will no longer need to do a two-pass iteration scheme. The difficulty will be finding an extension to the CVX algorithm which can handle the nonlinear optimization due to the appearance of the *b* coefficients in the denominator.

4.4 Summary

To summarize, in this chapter we illuminated the need to go beyond the thermal conductivity accumulation in understanding the material properties that affect nondiffusive thermal transport. We suggest not using vague terms such as the MFP distribution to refer to the thermal conductivity accumulation, as we see that this is not the only accumulation function that matters. We demonstrated the importance of characterizing the heat capacity accumulation function, and provided an extension to the current reconstruction algorithm. There is still more work to be done, regarding a study of sensitivity to reconstruction. As the process is an ill-posed linear algebra problem, the reconstruction algorithm is imperfect, and an in-depth study of the sensitivity of the algorithm is necessary. However, the steps taken to extend the algorithm to include the thermal conductivity as well as the heat capacity reconstruction, as well as the step to insert smooth basis functions as opposed to a brute force discretization are steps in the right direction.

Furthermore, there is also a need to devise a nonlinear algorithm to reconstructing the two accumulation functions simultaneously. The current results with a two step iteration has the drawback of requiring an understanding of which MFP the suppression function first step is accurate, and this value is not straightforward to determine without prior knowledge of the material's exact distribution. With a nonlinear reconstruction with the basis expansion, the two functions can be reconstructed without the issue of the trivial solution which appears after linearizing, and its application to studying complex materials can be implemented in the future.

Chapter 5

TDTR / FDTR geometry and the thermal interface problem

In this chapter, we aim to illuminate the effect of the thermal interface on heat transport, in particular in the nondiffusive regime. The previous heat transfer configurations with a TTG all included a single homogeneous medium in which heat transfer occurs. However, most common applications of heat transfer, such as for heat management [22,79,80], often have multiple materials and the role of the thermal interface must be understood. As we have seen, the geometry of a heat transfer configuration can produce size effects when the lengths are comparable to the MFPs of a given material, and this results in a reduced thermal conductivity as compared to bulk. We wish to study how the interface conductance is affected by the geometry of the system, and how the interface spectral transmissivity comes into play in the output of the experiments.

Picosecond thermoreflectance techniques opened the way to study thermal transfer at the nano and microscale [25,81]. Cahill *et al.* popularized the use of the TDTR to characterize thermal transfer in terms of the thermal conductivity of the substrate as well as the interface conductance [22]. A schematic of the typical TDTR experimental set up is shown in Fig. 5-1.

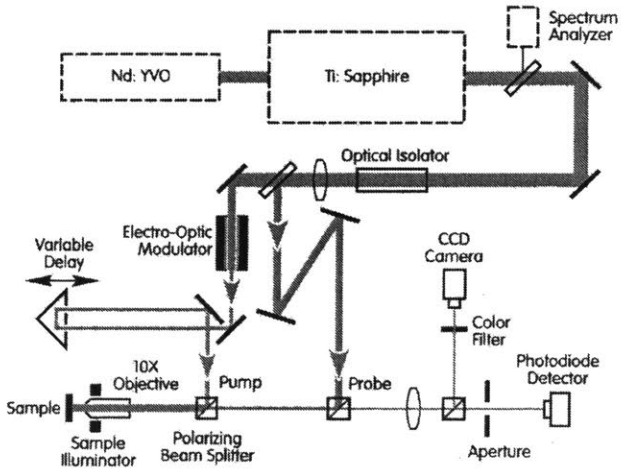

FIG. 5-1. Schematic of the TDTR experimental set up. Figure adapted from Ref. [22].

By modulating the pump laser beam, the thermal penetration depth of the heat into the substrate it altered, and by increasing the frequency of the modulation and thereby decreasing the thermal penetration depth, there is the hope to see size effects on the substrate thermal conductivity. The analysis to be able to study a metal layer on top of a substrate, and thus account for the layered structure thermal transport, allowed for the experimental fitting to be able to extract simultaneously the thermal conductivity and interface conductance [25,82]. Recently, the time-domain thermoreflectance [24–29] (TDTR) and frequency-domain thermoreflectance [30,31] (FDTR) have been utilized extensively in order to probe and observe nondiffusive transport by using ultrafast time scales or ultrashort length scales and gain key insight into the material's MFP spectrum. In particular, modulation frequency dependence of the thermal conductivity was observed with the FDTR [32] for certain materials like SiGe. Beyond the modulation frequency based length scale of the thermal penetration depth, there are also the in-plane length scales, and size effects from the beam spot, as depicted in Fig. 5-2, were observed for silicon [33], and nanostructured patterns such as line heaters and nanodots were fabricated to be able to push the length scales of the geometry to even smaller lengths to probe strongly nondiffusive transport [27,29].

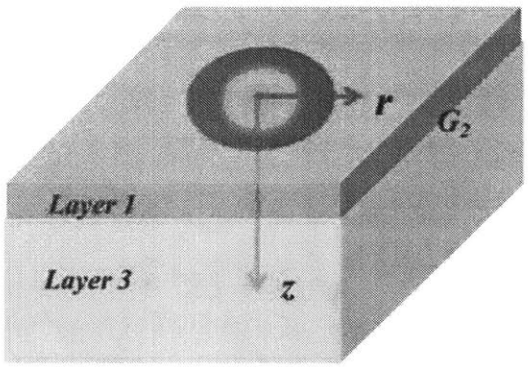

FIG. 5-2. Schematic of the layered structure of a metal (layer 1) on top of a substrate (layer 3), where the interface is considered as layer 2 with a conductance shown by G_2. Figure adapted from Ref. [82].

With the push to study size effects from short length scales by fabricating the line heaters and nanodots, there is a need to distinguish the difference in the type of signal that is observed in the TDTR/FDTR vs. the TTG. Given the sinusoidal grating in the TTG, and the fact that a diffraction pattern is how the temperature is extracted, the signal obtained is a difference between the peak and valley of the heating profile. Thus the signal is sensitive to the grating as it only includes the sinusoidal nature of the heating, and not the overall macroscopic uniform heating. However, with the TDTR, the signal obtained is a reflection from the metal surface, and theoretical/computational analysis has shown that fitting the experiment to the temperature profile from a peak or a peak-valley measurement can yield different trends for the effective thermal conductivity [26]. Given that the overall signal for the in-plane heating profile can be decomposed into various Fourier modes, it will include the macroscopic uniform heating behavior, and it is important to include all relevant terms for appropriate modeling of what the experiment outputs.

Furthermore, there have been many interesting questions left not fully answered for the size effects due to the modulation frequency. Given that the Fourier heat conduction equation under temporal modulation of linear frequency v results in exponential decay in a substrate with a penetration depth given by $L_p = \sqrt{\frac{k}{\pi v C}}$, this defines a length scale with which one would expect to see size effects. As mentioned previously, indeed, size effects were observed for certain materials [32] such as SiGe in the range of MHz. More recently, size effects on silicon were measured with the FDTR configuration [31] which clearly showed a reduction in the thermal conductivity of silicon in the range of one to hundreds of MHz. Furthermore, a frequency domain representation of data in the time domain from TDTR never revealed such size effects for the case of silicon [24,83]. Thus there is clearly the need to model fully and understand the possibilities of there being not only size effects possible in the MHz range of frequencies for silicon as an example material, but also to see whether this signature of nondiffusive transport is possible to be seen from the experimental observables of amplitude and phase from the surface of the metal.

On the theory side, there have been attempts to understand frequency dependence for simpler configurations, such as one without an interface [49], as well as one with fitting of the interface transmissivities to explain the effect of the modulation frequency in silicon [84].

However, there is no clear consensus in the literature of the role of the interface transmissivities and the modulation frequency in the nondiffusive regime of thermal transfer of a substrate under a metal layer heated by a laser. In this chapter, I will lay out an analysis of the thermoreflectance geometry of a metal layer on top of a substrate, taking into consideration the transmission/reflection of phonons at the interface, and study the size effects of both an in-plane length scale as well as the effect of the modulation frequency on thermal transport in the presence of an interface. By providing the variational solution, I provide deeper insight into the effect the interface has as well as the modulation frequency values at which size effects can be observed in this heat transfer configuration.

5.1 Modeling thermal transport with an interface

In order to understand the role of the interface in current experiments, we aim to model a metal transducer on top of a substrate using the variational approach. Consider a semi-infinite substrate, whose material properties we denote with a subscript of 2, with a metal film of thickness d on top, whose material properties we denote with a subscript of 1. To understand the behavior of the system in the nondiffusive regime, we considering a thermal grating for the surface heating profile. As any in-plane profile can be obtained with a superposition of such grating solutions, this provides a canonical starting point for analyzing the TDTR/FDTR geometry. We consider an isotropic substrate, but allow for an anisotropic metal. This will allow us to study the effect of heat dissipation in the in-plane vs. cross-plane directions in the metal, and study the sensitivity of the surface response of the metal to the substrate. The laser heating is absorbed only within the metal, and the heat is dissipated away both in the in-plane direction as well as across the interface into the substrate.

The volumetric heat generation rate in the metal is thus given by:

$$Q(x,y,z,t) = e^{i2\pi\nu t} e^{iq_x x} e^{iq_y y} Q_0 \frac{\beta \exp(-\beta z)}{1-\exp(-\beta d)} \tag{5.1}$$

where β is the inverse penetration depth of the heating profile. For the grating, $\boldsymbol{q}$ is the grating wavevector, whose magnitude is related to the grating period λ as $q = 2\pi / \lambda$. The magnitude q is also related to the x and y components as $q = \sqrt{q_x^2 + q_y^2}$. For the experimental conditions of a spatially periodic heating, the temperature is given by $T(x,y,z,t) = T_0 + e^{i2\pi\nu t} e^{iq_x x} e^{iq_y y} \Delta\tilde{T}(z)$ in complex form. The temperature T_0 is the background equilibrium temperature of the system, for example the room temperature. The temperature ΔT as shown here represents a peak-null difference temperature if we simulate a thermal grating. If we take the grating wavevector to zero, i.e. $q = 0$, then this temperature represents the absolute temperature due to uniform heating and yields the response to a one-dimensional cross plane heat transfer problem. Thus obtaining the functional form of ΔT allows us to then take an appropriate superposition to reconstruct the true response to any in-plane heating profile, whether it is uniform heating, a sinusoidal grating, a Gaussian beam spot, or square wave heating like with the metal line gratings.

The Fourier heat conduction equation for the metal and substrate simplify to:

$$\begin{aligned} \frac{\partial^2}{\partial z_1^2}\Delta\tilde{T}_1 &= \frac{i2\pi\nu C_1 + k_{1,i}q^2}{k_{1,c}}\Delta\tilde{T}_1 - \frac{Q_0}{k_{1,c}}\frac{\beta\exp(-\beta z_1)}{1-\exp(-\beta d)} \\ \frac{\partial^2}{\partial z_2^2}\Delta\tilde{T}_2 &= \frac{i2\pi\nu C_2 + k_2 q^2}{k_2}\Delta\tilde{T}_2 \end{aligned} \tag{5.2}$$

where $k_{1,i}$ and $k_{1,c}$ are the in-plane and cross-plane thermal conductivities of the metal, respectively. The boundary conditions are given by:

$$\begin{aligned} \Delta\tilde{T}_2(z_2 \to \infty) &= 0 \\ -k_{1,c}\left(\frac{\partial}{\partial z_1}\Delta\tilde{T}_1\right)\Big|_{z_1=0} &= 0 \\ -k_{1,c}\left(\frac{\partial}{\partial z_1}\Delta\tilde{T}_1\right)\Big|_{z_1=d} &= -k_2\left(\frac{\partial}{\partial z_2}\Delta\tilde{T}_2\right)\Big|_{z_2=0} \\ -k_2\left(\frac{\partial}{\partial z_2}\Delta\tilde{T}_2\right)\Big|_{z_2=0} &= G\left[\Delta\tilde{T}_1(z_1=d) - \Delta\tilde{T}_2(z_2=0)\right] \end{aligned} \tag{5.3}$$

These boundary conditions impose that the system is equilibrium deep into the substrate, that the top surface of the metal is adiabatic and the heating from the laser pulse is included in the

volumetric heat generation term, that there is heat flux continuity across the interface, and that there is an interface conductance G characterizing the interface.

We define for simplicity the complex lengths:

$$L_1 \equiv \sqrt{\frac{k_{1,c}}{i2\pi\nu C_1 + k_{1,i}q^2}}$$
$$L_2 \equiv \sqrt{\frac{k_2}{i2\pi\nu C_2 + k_2 q^2}} \tag{5.4}$$

In terms of these lengths, we are able to solve Eq. (5.2) and utilize the boundary conditions of Eq. (5.3) to obtain:

$$\Delta\tilde{T}_1(z_1) = \frac{Q_0}{1-\exp(-\beta d)}\frac{\beta^2}{\beta^2 - L_1^{-2}}\frac{L_1}{k_{1,c}}\left\{\frac{-\frac{1}{\beta L_1}\exp(-\beta z_1) + \sinh\left(\frac{d-z_1}{L_1}\right) + \frac{k_{1,c}}{L_1}\left(\frac{1}{G}+\frac{L_2}{k_2}\right)\cosh\left(\frac{d-z_1}{L_1}\right) + \exp(-\beta d)\cosh\left(\frac{z_1}{L_1}\right)\left[\frac{1}{\beta L_1} - \frac{k_{1,c}}{L_1}\left(\frac{1}{G}+\frac{L_2}{k_2}\right)\right]}{\cosh\left(\frac{d}{L_1}\right) + \frac{k_{1,c}}{L_1}\left(\frac{1}{G}+\frac{L_2}{k_2}\right)\sinh\left(\frac{d}{L_1}\right)}\right\}$$
$$\Delta\tilde{T}_2(z_2) = \frac{Q_0}{1-\exp(-\beta d)}\frac{\beta^2}{\beta^2 - L_1^{-2}}\frac{L_2}{k_2}\exp\left(-\frac{z_2}{L_2}\right)\frac{1-\exp(-\beta d)\left[\cosh\left(\frac{d}{L_1}\right) + \frac{1}{\beta L_1}\sinh\left(\frac{d}{L_1}\right)\right]}{\cosh\left(\frac{d}{L_1}\right) + \frac{k_{1,c}}{L_1}\left(\frac{1}{G}+\frac{L_2}{k_2}\right)\sinh\left(\frac{d}{L_1}\right)} \tag{5.5}$$

We will utilize the Fourier heat conduction temperature profile in our variational solution of the BTE. The temperature solution of Eq. (5.5) represents the temperature response with a modulation temporally as well as a sinusoidal grating. Any in-plane heating profile can be obtained by taking a superposition of the solution to a sinusoidal spatial profile. If we are interested in the case of a large beam spot heating the system uniformly, then by taking the $q = 0$ limit of Eq. (5.5), we obtain the temperature response to a large beam spot, which relates to just the absolute temperature and not a peak-valley difference as would occur with a grating in the TTG. If we are interested in other spatial profiles, we simply need to take a superposition of the temperature response with different values of the grating $\boldsymbol{q}$. The experiment outputs the surface temperature, thus one can obtain the particular case of the FDTR experimental response [30,31,85] to a frequency modulation of linear frequency ν. The surface amplitude and phase response is given by:

$$Re^{-i\phi} \equiv \frac{\Delta\tilde{T}_1(z_1=0)}{Q_0}$$

$$= \frac{1}{1-\exp(-\beta d)} \frac{\beta^2}{\beta^2 - L_1^{-2}} \frac{L_1}{k_{1,c}} \left\{ \frac{-\frac{1}{\beta L_1} + \sinh\left(\frac{d}{L_1}\right) + \frac{k_{1,c}}{L_1}\left(\frac{1}{G}+\frac{L_2}{k_2}\right)\cosh\left(\frac{d}{L_1}\right) + \exp(-\beta d)\left[\frac{1}{\beta L_1} - \frac{k_{1,c}}{L_1}\left(\frac{1}{G}+\frac{L_2}{k_2}\right)\right]}{\cosh\left(\frac{d}{L_1}\right) + \frac{k_{1,c}}{L_1}\left(\frac{1}{G}+\frac{L_2}{k_2}\right)\sinh\left(\frac{d}{L_1}\right)} \right\} \tag{5.6}$$

To solve for the thermal transport in the nondiffusive transport regime, we begin with the spectral Boltzmann transport equation under the relaxation time approximation:

$$\frac{\partial g_\omega}{\partial t} + \vec{v}_\omega \cdot \vec{\nabla} g_\omega = \frac{1}{\tau_\omega}\left[\frac{C_\omega}{4\pi}\Delta T - g_\omega\right] + \frac{Q_\omega}{4\pi} \tag{5.7}$$

We will solve the BTE for the metal layer and the substrate separately. For the metal, we assume diffusive thermal transport, so we will take the diffusive limit for the BTE for the metal. This means that we are essentially doing a Taylor expansion in the relaxation time of the metal, and only keeping up to linear order in the relaxation time. Doing so yields the solution for the BTE for the metal in terms of the temperature and heating profile:

$$g_{\omega,1} = \frac{C_{\omega,1}}{4\pi}\left[\Delta T_1 - \tau_{\omega,1}\frac{\partial}{\partial t}\Delta T_1 - \tau_{\omega,1}\vec{v}_{\omega,1}\cdot\vec{\nabla}\Delta T_1\right] + Q\frac{p_\omega \tau_{\omega,1}}{4\pi} \tag{5.8}$$

The thermal grating heating profile, given by the heating form $Q = e^{i2\pi\nu t}e^{iq_x x}e^{iq_y y}\tilde{Q}(z)$ means we can expect that the energy density to also obey a similar profile $g_\omega = e^{i2\pi\nu t}e^{iq_x x}e^{iq_y y}\tilde{g}_\omega(z)$ By inputting this in-plane sinusoidal profile and sinusoidal temporal profile simplifies the solution to:

$$\tilde{g}_{\omega,1}(z_1) = \frac{C_{\omega,1}}{4\pi}\left[\left(1 - i\varphi_{\omega,1} - i\vec{q}\cdot\vec{v}_{\omega,1}\tau_{\omega,1}\right)\Delta\tilde{T}_1 - \vec{e}_z\cdot\vec{v}_{\omega,1}\tau_{\omega,1}\frac{\partial}{\partial z_1}\Delta\tilde{T}_1\right] + \tilde{Q}(z_1)\frac{p_\omega\tau_{\omega,1}}{4\pi} \tag{5.9}$$

where we have defined the nondimensional parameter $\varphi_{\omega,1} = 2\pi\nu\tau_{\omega,1}$.

For the substrate, there is no heating in the substrate layer, so the BTE is given by:

$$\frac{\partial g_{\omega,2}}{\partial t} + \vec{v}_{\omega,2}\cdot\vec{\nabla} g_{\omega,2} = \frac{1}{\tau_{\omega,2}}\left[\frac{C_{\omega,2}}{4\pi}\Delta T_2 - g_{\omega,2}\right] \tag{5.10}$$

Given the sinusoidal spatial in-plane and temporal profiles, the BTE for the substrate simplifies to:

$$\frac{\partial \tilde{g}_{\omega,2}}{\partial z_2} + A_2 g_{\omega,2} = \frac{C_{\omega,2}}{4\pi\mu_z \Lambda_{\omega,2}} \Delta\tilde{T}_2 \tag{5.11}$$

where we have defined the following parameters:

$$\begin{aligned} A_2 &\equiv \frac{1 + i\varphi_{\omega,2} + iq_x\mu_x\Lambda_{\omega,2} + iq_y\mu_y\Lambda_{\omega,2}}{\mu_z\Lambda_{\omega,2}} \\ \varphi_{\omega,2} &\equiv 2\pi\nu\tau_{\omega,2} \end{aligned} \tag{5.12}$$

for the sake of compactness of the solutions. The BTE of Eq. (5.11) can now be solved easily to yield:

$$\tilde{g}_{\omega,2}(z_2) = \exp(-A_2 z_2)\tilde{g}_{\omega,2}(0) + \frac{C_{\omega,2}}{4\pi\mu_z\Lambda_{\omega,2}} \int_0^{z_2} dz_2' \exp\left(-A_2(z_2 - z_2')\right)\Delta T_2(z_2') \tag{5.13}$$

The energy density at the surface of the substrate will be calculated using the follow boundary conditions:

$$\begin{aligned} \tilde{g}_{\omega,2}(L)\Theta(-\mu_z) &= 0 \\ \tilde{g}_{\omega,2}(0)\Theta(\mu_z) &= \Theta(\mu_z)\frac{1}{\mathrm{v}_{\omega,2}}\left(\mathrm{T}_\omega J_{\omega,1} + \mathrm{R}'_\omega J_{\omega,2}\right) \end{aligned} \tag{5.14}$$

which utilize transmission and reflection coefficients from the metal into the substrate, T_ω and $\mathrm{R}_\omega = 1 - \mathrm{T}_\omega$, as well as the transmission and reflection coefficients from the substrate into the metal, T'_ω and $\mathrm{R}'_\omega = 1 - \mathrm{T}'_\omega$. These are related by the principle of detailed balance, which ensures no net flux across the interface at thermal equilibrium, given by $C_{\omega,1}\mathrm{v}_{\omega,1}\mathrm{T}_\omega = C_{\omega,2}\mathrm{v}_{\omega,2}\mathrm{T}'_\omega$ [38].

The fluxes approaching the interface denoted by J are given by:

$$\begin{aligned} J_{\omega,1} &= \frac{1}{\pi}\int d\Omega\Theta\left(\vec{\mathrm{v}}_{\omega,1}\cdot\vec{e}_z\right)\left(\vec{\mathrm{v}}_{\omega,1}\cdot\vec{e}_z\right)\tilde{g}_{\omega,1}(d) \\ J_{\omega,2} &= -\frac{1}{\pi}\int d\Omega\Theta(-\mu_z)\mu_z\tilde{g}_{\omega,2}(0) \end{aligned} \tag{5.15}$$

We have used the Heaviside step function Θ in order to restrict to phonons moving away or towards the interface. The first boundary condition of Eq. (5.14) represents the fact that far into the substrate, the system is at thermal equilibrium at the background reference temperature. To achieve this, the first boundary condition takes an imaginary blackbody wall at length L into the substrate at the background temperature to account for the semi-infinite substrate, and later we will take this length to infinity to achieve a true semi-infinite substrate. The second boundary condition represents transmission and reflection across the interface, assuming elastic, diffuse

scattering. Thus the flux at each given phonon frequency conserves energy across the interface, and the phonons are scattering completely diffusively so that they lose information about their direction of travel after scattering at the interface.

Solving the boundary conditions and taking the artificial length L to infinity yields the solution to the BTE for the substrate as a functional of the substrate temperature:

$$\begin{aligned}\tilde{g}_{\omega,2}(z_2) = \Theta(\mu_z)\left\{\exp(-A_2 z_2)\frac{1}{\mathrm{v}_{\omega,2}}\left(\mathrm{T}_\omega J_{\omega,1} + \mathrm{R}'_\omega J_{\omega,2}\right) + \frac{C_{\omega,2}}{4\pi\mu_z\Lambda_{\omega,2}}\int_0^{z_2} dz_2' \,\Delta\tilde{T}_2(z_2')\exp\left(-A_2(z_2 - z_2')\right)\right\} + \\ -\Theta(-\mu_z)\frac{C_{\omega,2}}{4\pi\mu_z\Lambda_{\omega,2}}\int_{z_2}^{\infty} dz_2' \,\Delta\tilde{T}_2(z_2')\exp\left(-A_2(z_2 - z_2')\right)\end{aligned} \tag{5.16}$$

where the fluxes approaching the interface are calculated to be:

$$\begin{aligned}J_{\omega,1} = \tilde{Q}(d)\frac{1}{(2\pi)^2}\int d\Omega\Theta\left(\vec{\mathrm{v}}_{\omega,1}\cdot\vec{e}_z\right)\left(\vec{\mathrm{v}}_{\omega,1}\cdot\vec{e}_z\right)p_\omega\tau_{\omega,1} + \\ \frac{1}{(2\pi)^2}\int d\Omega\Theta\left(\vec{\mathrm{v}}_{\omega,1}\cdot\vec{e}_z\right)\left(\vec{\mathrm{v}}_{\omega,1}\cdot\vec{e}_z\right)C_{\omega,1}\left[\left(1 - i\varphi_{\omega,1}\right)\Delta\tilde{T}_1(d) - \vec{e}_z\cdot\vec{\mathrm{v}}_{\omega,1}\tau_{\omega,1}\left(\frac{\partial}{\partial z_1}\Delta\tilde{T}_1\right)\Big|_{z_1=d}\right] \\ J_{\omega,2} = \frac{C_{\omega,2}}{2\pi\tau_{\omega,2}}\int_0^{\infty} dz_2' \,\Delta\tilde{T}_2(z_2')\frac{1}{2\pi}\int d\Omega\Theta(\mu_z)\exp\left(-A_2 z_2'\right)\end{aligned} \tag{5.17}$$

This completes the solution to the BTE as a functional of the temperatures. As demonstrated in chapters 2 and 3, one can solve the integral equation to obtain the exact temperature, but again we will proceed instead with a variational approach to solve for the temperature in the nondiffusive regime.

5.2 Variational approach to solving interfacial thermal transport

In previous applications of the variational method, we have only needed a single parameter, such as the thermal conductivity or thermal diffusivity, but in this case, given that we have two materials with an interface, we have three parameters that we treat as variational parameters: the thermal conductivity of the metal, the thermal conductivity of the substrate, and the interface conductance. Furthermore, in previous cases, we have only needed to obtain the effective conductivity as a function of the length scales in the geometry, such as the thermal grating period

and the film thickness [65]. In this case, there is also the need to understand the size effects on the substrate due to the modulation frequency ν. As the transport in the metal was assumed to be diffusive, we will solve and obtain the macroscopic value of the thermal conductivity for the metal. Furthermore, we assume the interface conductance depends only on the in-plane length scales, such as the grating period, and not on the modulation frequency. Only the substrate conductivity will be assumed to depend on the modulation frequency in addition to the in-plane length scales, as the frequency can affect the penetration of heat into the substrate.

As a first pass, we assume no frequency dependence for the substrate conductivity in order to derive the DC limit (i.e. $\nu = 0$) of the conductance and conductivities. Then the interface conductance and metal thermal conductivity will be inputted into a variational calculation to obtain the frequency dependence of the substrate conductivity. We proceed first with the frequency independent calculation. Given that we have 3 variational parameters in this system, we have 3 physical conditions that we can impose. We will impose energy conservation over the control volume of the metal, as well as energy conservation over the control volume of the substrate, and also an interface condition. The requirement of energy conservation taken over the control volume is similar to the condition utilized for the thin film TTG geometry [65]. More specifically, for the metal, we choose the control volume to be over the thickness d in the cross plane, and for convenience a width equal to half of the grating period in the in-plane direction. For the substrate, we take a control volume over the entire semi-infinite system in the cross plane, and again a width equal to half of the grating period in the in-plane direction. Rigorously, the choice of width in the in-plane direction within a grating period does not matter, which is a consequence of a perfectly sinusoidal heating. For periodic heating that is not comprised of a single sinusoid, the choice of width in the in-plane direction will affect the variational condition obtained.

Lastly, the interface condition we take is to enforce that the total heat flux across the interface in the steady state limit of $\nu = 0$ as predicted from the solution to the BTE match the prediction from the solution to the Fourier heat conduction equation. Mathematically, these three conditions can be expressed as:

$$\tilde{J}_1 = G\left[\Delta\tilde{T}_1(d) - \Delta\tilde{T}_2(0)\right]$$
$$Q_0 = iq_x\int_0^d \tilde{J}_{x,1}(z_1)dz_1 + iq_y\int_0^d J_{y,1}(z_1)dz_1 + \tilde{J}_1 \tag{5.18}$$
$$0 = iq_x\int_0^\infty \tilde{J}_{x,2}(z_2)dz_2 + iq_y\int_0^\infty J_{y,2}(z_2)dz_2 - \tilde{J}_1$$

These three physical conditions define three sets of equations to solve for the conductivities of the metal and the substrate, as well as the interface conductance G. By calculating the local fluxes in each material using the solutions of the BTE from Eq. (5.9) and Eq. (5.16), we obtain the result as a functional of the temperatures in each material. We input the temperature distributions from Fourier's law, given in Eq. (5.5), and then insert these expressions into the variational conditions of Eq. (5.18) above. When these three equations are utilized simultaneously, we obtain the expected result for the metal conductivity for diffusive transport in the isotropic case, $k_1 = \frac{1}{3}\int d\omega C_{\omega,1} v_{\omega,1}\Lambda_{\omega,1}$, and a linear matrix equation for $1/k_2$ and $1/G$. Solving these matrix equations yields the effective interface conductance and effective substrate thermal conductivity within this variational formalism as the first pass without frequency dependence:

$$k_2 = \frac{\left\{\left(\frac{1}{4}\int d\omega C_{\omega,2}v_{\omega,2}T'_\omega\right)\left(\frac{1}{6}\int d\omega C_{\omega,2}v_{\omega,2}\Lambda_{\omega,2}\left\{\frac{3}{\eta_{\omega,2}^2}\left[1-\frac{1}{\eta_{\omega,2}}\arctan(\eta_{\omega,2})\right]+R'_\omega\frac{2}{1+\sqrt{1+\eta_{\omega,2}^2}}\left[1-\frac{\left(1+\eta_{\omega,2}^2\right)^{\frac{1}{2}}-1-\frac{3}{2}\eta_{\omega,2}^2}{\eta_{\omega,2}^3}\right]\right\}\right)+\right.}{\left.\left(\frac{1}{4}\int d\omega C_{\omega,2}v_{\omega,2}T'_\omega\frac{2}{1+\sqrt{1+\eta_{\omega,2}^2}}\right)\left(\frac{1}{6}\int d\omega C_{\omega,2}v_{\omega,2}\Lambda_{\omega,2}T'_\omega\left[1-\frac{\left(1+\eta_{\omega,2}^2\right)^{\frac{1}{2}}-1-\frac{3}{2}\eta_{\omega,2}^2}{\eta_{\omega,2}^3}\right]\right)\right\}}$$
$$\left(1-\frac{1}{6k_1}\int d\omega C_{\omega,1}v_{\omega,1}\Lambda_{\omega,1}T_\omega\right)\left(\frac{1}{4}\int d\omega C_{\omega,2}v_{\omega,2}T'_\omega\frac{2}{1+\sqrt{1+\eta_{\omega,2}^2}}\right)+\left(\frac{1}{6k_1}\int d\omega C_{\omega,1}v_{\omega,1}\Lambda_{\omega,1}T_\omega\frac{2}{1+\sqrt{1+\eta_{\omega,2}^2}}\right)\left(\frac{1}{4}\int d\omega C_{\omega,2}v_{\omega,2}T'_\omega\right)$$

$$G = \frac{\left\{\left(\frac{1}{4}\int d\omega C_{\omega,2}v_{\omega,2}T'_\omega\right)\left(\frac{1}{6}\int d\omega C_{\omega,2}v_{\omega,2}\Lambda_{\omega,2}\left\{\frac{3}{\eta_{\omega,2}^2}\left[1-\frac{1}{\eta_{\omega,2}}\arctan(\eta_{\omega,2})\right]+R'_\omega\frac{2}{1+\sqrt{1+\eta_{\omega,2}^2}}\left[1-\frac{\left(1+\eta_{\omega,2}^2\right)^{\frac{1}{2}}-1-\frac{3}{2}\eta_{\omega,2}^2}{\eta_{\omega,2}^3}\right]\right\}\right)+\right.}{\left.\left(\frac{1}{4}\int d\omega C_{\omega,2}v_{\omega,2}T'_\omega\frac{2}{1+\sqrt{1+\eta_{\omega,2}^2}}\right)\left(\frac{1}{6}\int d\omega C_{\omega,2}v_{\omega,2}\Lambda_{\omega,2}T'_\omega\left[1-\frac{\left(1+\eta_{\omega,2}^2\right)^{\frac{1}{2}}-1-\frac{3}{2}\eta_{\omega,2}^2}{\eta_{\omega,2}^3}\right]\right)\right\}} \tag{5.19}$$
$$\left\{\left(1-\frac{1}{6k_1}\int d\omega C_{\omega,1}v_{\omega,1}\Lambda_{\omega,1}T_\omega\right)\left(\frac{1}{6}\int d\omega C_{\omega,2}v_{\omega,2}\Lambda_{\omega,2}\left\{\frac{3}{\eta_{\omega,2}^2}\left[1-\frac{1}{\eta_{\omega,2}}\arctan(\eta_{\omega,2})\right]+R'_\omega\frac{2}{1+\sqrt{1+\eta_{\omega,2}^2}}\left[1-\frac{\left(1+\eta_{\omega,2}^2\right)^{\frac{1}{2}}-1-\frac{3}{2}\eta_{\omega,2}^2}{\eta_{\omega,2}^3}\right]\right\}\right)+\right.$$
$$\left.-\left(\frac{1}{6k_1}\int d\omega C_{\omega,1}v_{\omega,1}\Lambda_{\omega,1}T_\omega\frac{2}{1+\sqrt{1+\eta_{\omega,2}^2}}\right)\left(\frac{1}{6}\int d\omega C_{\omega,2}v_{\omega,2}\Lambda_{\omega,2}T'_\omega\left[1-\frac{\left(1+\eta_{\omega,2}^2\right)^{\frac{1}{2}}-1-\frac{3}{2}\eta_{\omega,2}^2}{\eta_{\omega,2}^3}\right]\right)\right\}$$

where we defined the nondimensional variable $\eta_{\omega,2} = q\Lambda_{\omega,2}$. We note a few key properties about the expressions that appear for the steady state ($v = 0$) limit of the conductivity and interface conductance. First off, we note of course the dependence of the interface conductance on both

the properties of the metal, the substrate, as well as the transmission coefficients. Furthermore, the effective thermal conductivity of the substrate also shows dependence on not only the substrate material properties but also on the metal material properties as well as the transmission coefficients. Inherently, this is a coupled problem and there is little meaning alone to just one of the coefficients and both the conductivity and interface conductance together complete the picture of this model. Given that we took the limit of diffusive transport in the metal, we do not see dependence, as expected, upon the thickness of the metal for the substrate conductivity and interface conductance. Using these analytical formulas, we can also take the limit of very large gratings to look at the lowest order contributions in the nondiffusive limit. We obtain:

$$k_2(\lambda\to\infty)=\frac{1}{3}\int d\omega C_{\omega,2}v_{\omega,2}\Lambda_{\omega,2}\left(1-\frac{3}{16}\eta_{\omega,2}\right)$$

$$G(\lambda\to\infty)=\frac{\frac{1}{4}\int d\omega C_{\omega,2}v_{\omega,2}T'_{\omega}}{1-\frac{1}{2}\left(\frac{\int d\omega C_{\omega,1}v_{\omega,1}\Lambda_{\omega,1}T_{\omega}}{\int d\omega C_{\omega,1}v_{\omega,1}\Lambda_{\omega,1}}+\frac{\int d\omega C_{\omega,2}v_{\omega,2}\Lambda_{\omega,2}T'_{\omega}}{\int d\omega C_{\omega,2}v_{\omega,2}\Lambda_{\omega,2}}\right)}\left\{1-\frac{3}{16}\frac{\frac{\int d\omega C_{\omega,2}v_{\omega,2}\Lambda_{\omega,2}T'_{\omega}\eta_{\omega,2}}{\int d\omega C_{\omega,2}v_{\omega,2}\Lambda_{\omega,2}}-\frac{1}{2}\frac{\int d\omega C_{\omega,2}v_{\omega,2}\Lambda_{\omega,2}T'_{\omega}}{\int d\omega C_{\omega,2}v_{\omega,2}\Lambda_{\omega,2}}\frac{\int d\omega C_{\omega,2}v_{\omega,2}\Lambda_{\omega,2}\eta_{\omega,2}}{\int d\omega C_{\omega,2}v_{\omega,2}\Lambda_{\omega,2}}}{1-\frac{1}{2}\left(\frac{\int d\omega C_{\omega,1}v_{\omega,1}\Lambda_{\omega,1}T_{\omega}}{\int d\omega C_{\omega,1}v_{\omega,1}\Lambda_{\omega,1}}+\frac{\int d\omega C_{\omega,2}v_{\omega,2}\Lambda_{\omega,2}T'_{\omega}}{\int d\omega C_{\omega,2}v_{\omega,2}\Lambda_{\omega,2}}\right)}\right\} \tag{5.20}$$

The large grating period limit recovers the bulk values of the substrate conductivity as well as interface conductance, which properly accounts for the correct temperature at the two sides of the interface as opposed to an improper emission temperatures of phonons approaching the interface [38]. As there are phonons approaching the interface as well as leaving the interface on each side, the correct definition of a temperature is necessary for obtaining an accurate interface conductance. The lowest order nondiffusive correction is of the order of λ^{-1} due to the $\eta_{\omega,2}$ term that appears.

Given the particular substrate's material properties and the transmission coefficients, we can then do a forward calculation and obtain the effective substrate conductivity and interface conductance, and insert them into the Fourier surface temperature profile to show the amplitude and phase response to modulated heating. We will focus on showing the amplitude and phase response as a function of the modulation frequency as this is closer to the experimental output. Our interest is to see how sensitive the effective substrate conductivity and interface thermal conductance are to the grating period, and to the transmissivity across the interface. We consider the phonon properties of the metal, as we are interested in the transmission of phonons across the interface. First, given that the MFP of phonons or electrons in aluminum is over a relatively narrow range of values [86], we take a single average value for the spectral MFP in the metal,

and can pull it out of any frequency integrals. Second, as a simple crude approximation, we take the metal properties to be given by a simple speed of sound $v_1 \approx 6000$ m/s. In this case, the two terms in both the substrate conductivity as well as the interface conductance in which the metal material properties appear can be simplified and we utilize the principle of detailed balance to yield:

$$\frac{1}{6k_1}\int d\omega C_{\omega,1} v_{\omega,1} \Lambda_{\omega,1} T_\omega = \frac{\int d\omega C_{\omega,2} v_{\omega,2} T'_\omega}{2C_1 v_1} \tag{5.21}$$

which now only require the total heat capacity and speed of sound in the metal. Thus in the variational temperature profile, we insert the bulk values of conductivity and heat capacity for aluminum where k_1 and C_1 appear. We note that the transport we consider here though is only for phonons, and neglect the effect of electrons or coupling of electrons with phonons. Thus, the thermal transport is mediated by phonons with the transmission and reflection of phonons across the interface between the aluminum and silicon materials.

As a first pass we assume the transmission from substrate to metal to be a constant, independent of frequency, $T'_\omega = T'$. We will plug in various values of this transmission to get a quick, crude sense of the sensitivity of the substrate effective thermal conductivity and the interface conductance to the transmission value. This is by no means an accurate representation of the details of the transmission coefficients, but rather a quick check to understand the general role its average value may play. In Fig. 5-3, we plot the dependence of the normalized interface conductance on the in-plane grating period.

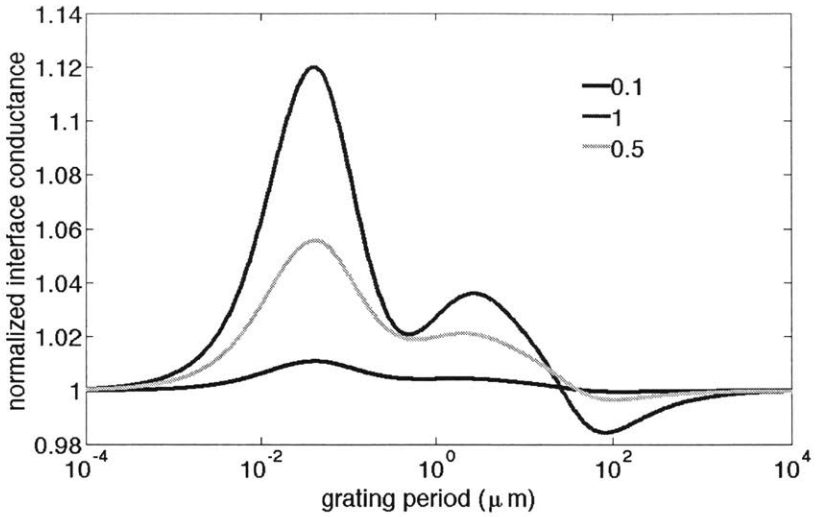

FIG. 5-3. Normalized effective interface thermal conductance for various values of the gray transmissivity. For low values of the transmissivity, the interface conductance is essentially the bulk value. For large values of the transmissivity, at most it varies by 10% relative to the bulk value.

We see that when the gray transmission value is low, it doesn't vary from the bulk value, but when the transmission is high, i.e. perfectly unity, the interface conductance varies by at most 10% from the bulk. This demonstrates that the in-plane length scale has a weak effect on the interface conductance. In Fig. 5-4, we plot the normalized effective thermal conductivity as a function of the grating period. We see that for a gray transmission, the value of the transmission chosen does not affect the conductivity. So while the mathematical expression from the variational result shows the appearance of the transmissivity, upon numerical calculation we find no dependence. The conductivity outputted matches the results from the variational solution of the 1D TTG (plotted as black markers for reference), indicating that the substrate conductivity is only affected by the in-plane length scale under the assumption of a gray transmission model.

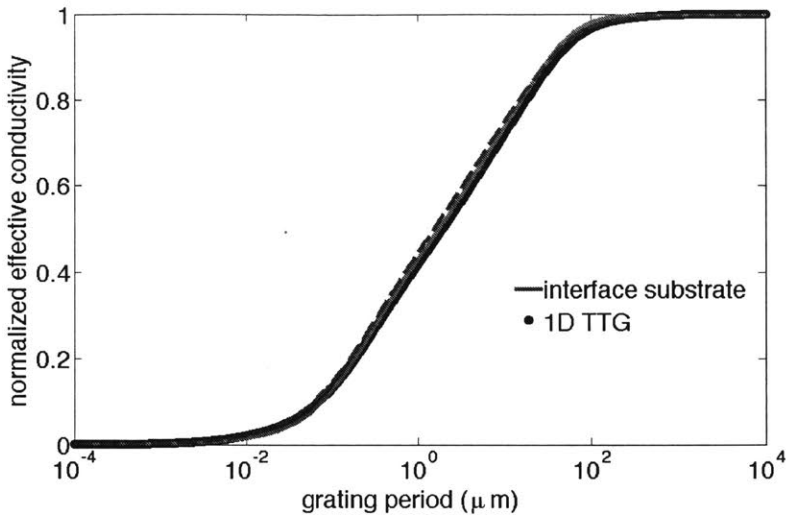

FIG. 5-4. Normalized effective conductivity of substrate as a function of the grating period. We are showing both the case with a transmission of 0.1 (dashed blue line) as well as 1 (solid red line), showing both a very low average transmissivity as well as the high to demonstrate that the effective thermal conductivity is not strongly dependent on the interface, and only upon the in-plane surface length scale.

A more interesting transmission function we can now explore is a spectral one to see if there is a strong effect from the interface on the substrate conductivity and interface conductance. One simple spectral model we will consider is that of a MFP filter. We can allow only phonons of very low MFP, or alternatively phonons of very high MFP to pass through the interface, and to see what effect this can have on the effective thermal conductance as well as the effective substrate thermal conductivity. The lowest MFPs for silicon we utilize are on the order of 1 nm, while the largest MFPs are on the order of 16 micron. We can create a high pass filter for the transmissivity, given by:

$$T'_{\omega,\text{high}} = \begin{cases} 1 & \Lambda_\omega \geq \Lambda_H \\ 0 & \Lambda_\omega < \Lambda_H \end{cases} \tag{5.22}$$

Similarly, we can create a low pass filter given by:

$$T'_{\omega,\text{low}} = \begin{cases} 1 & \Lambda_\omega \le \Lambda \\ 0 & \Lambda_\omega > \Lambda \end{cases} \tag{5.23}$$

where the low MFP cutoff is 2nm, while the high MFP cutoff is 16 micron. This is an artificial system as we would not be able to construct such a material that filters so perfectly, however from a theoretical standpoint, this provides the opportunity to study extreme behavior from the interface, and future studies can focus on more realistic filters. Figure 5-5 shows the behavior of the conductivity with the 1D TTG variational conductivity shown for reference. We see that there is a strong effect only for small enough grating periods, on the order of tens and hundreds of nanometers.

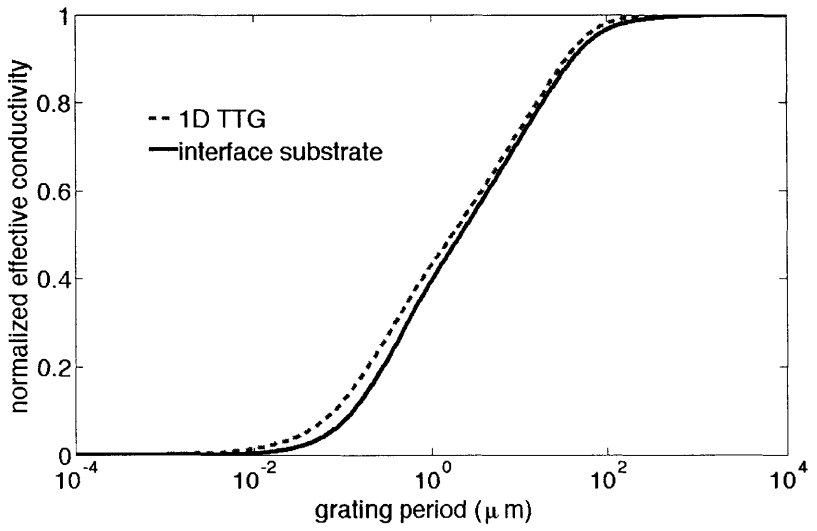

FIG. 5-5. Low MFP filter effective conductivity of the substrate. The effect of having only very short MFP phonons (2nms or less) transmit across the interface makes a noticeable difference for short grating periods as compared to simply the size effect observed from the one-dimensional limit of the TTG.

In Fig. 5-6, we show the results from the high MFP filter. We see here that this demonstrates a very different trend compared to that of a low MFP filter, and also very different than the results from the 1D TTG variational solution. We see non-monotonic behavior in the thermal

conductivity of the substrate, and in fact a strong enhancement when the grating period is on the order of 100 nm for this particular high MFP transmission function model.

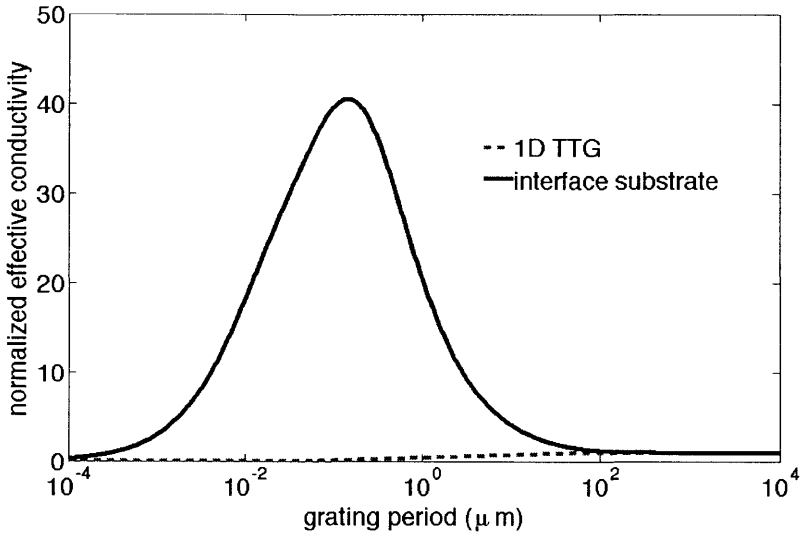

FIG. 5-6. High MFP filter effective conductivity as a function of grating period. Phonons with a MFP of 16 microns or larger are the only ones that transmit in this high MFP filter case. We note the remarkable enhancement of the thermal conductivity beyond that of bulk by over 40 times.

The result of altering the MFP filter from being perfectly unity to only a fraction, such as 0.1, makes no difference in the effective thermal conductivity. Thus, similar to the gray transmission results, the magnitude of the transmissivity of phonons does not affect the conductivity, however the selection of which phonons do transmit does play an effect. By only allowing phonons with short MFPs to filter through, the effective conductivity is smaller as those phonons contribute smaller to conductivity based on the kinetic picture than the consideration of all other phonons. Similarly, the phonons with only very high MFP contribute much larger to the conductivity, and thus by only allowing high MFPs to transmit across the interface, the system would respond as if the effective thermal conductivity is much higher, yielding a thermal conductivity even higher than that of bulk silicon. We will explore the exciting possibility of an enhancement of thermal conductivity as opposed to a reduction in the nanoscale regime in the next chapter, when we

consider the effect of the phonon distribution excited by heating of the system. Here, the interface acts essentially as a filter and we chose to introduce high MFP phonons into the system and noticed that there is indeed a strong enhancement by selecting the phonons which contribute more to the thermal conductivity than low MFP phonons. Thus we see that the exact value of the transmission, whether it is high or low, does not have as strong of an effect as the distribution of phonons which the transmission function considers passing into the substrate or not.

5.3 Effective thermal conductivity and size effects from modulation frequency

Given the understanding we have developed of the effect the grating period has and the interface transmissivity on the interface conductance and substrate conductivity, we now explore the frequency dependence of the substrate conductivity. In this case, we cannot satisfy energy conservation over the substrate control volume exactly, as the deviation from energy conservation will be a temporally oscillating term with both an amplitude and a phase. However, we can minimize the square error of the energy conservation of the substrate. Thus we define a penalty as a function of the substrate conductivity given by the energy conservation over the control volume of the substrate:

$$P(k_2)=\left|\int_0^\infty dz_2\left[i2\pi v\tilde{U}_2(z_2)+iq_x\tilde{J}_{x,2}(z_2)+iq_y\tilde{J}_{y,2}(z_2)\right]-\tilde{J}_1\right|^2 \tag{5.24}$$

As we are using the macroscopic value of the thermal conductivity for the metal (since the transport was assumed to be diffusive), as well as the interface conductance of Eq. (5.19) which does not depend on modulation frequency, we only need to minimize the penalty of Eq. (5.24) with respect to the substrate conductivity. This is why we needed to first solve the steady state limit of the interface conductance and substrate conductivity before moving onto this case which includes modulation frequency dependence for the substrate conductivity because the two variational parameters were needed as input into Eq. (5.24). Thus by finding the optimal effective conductivity for each given frequency which minimizes this square error penalty in the energy conservation of the control volume over the substrate, we obtain the variational thermal

conductivity. In the limit of zero modulation frequency, this conductivity will recover the result we obtained in Eq. (5.19).

Inserting the solution to the BTE and calculating the energy density, in-plane fluxes, and the interface flux this time as a function of modulation frequency, we obtain for the penalty function after simplifying some of the solid angle integrals:

$$P(k_2)=\left|\frac{Q_0}{1-\exp(-\beta d)}\frac{\beta^2}{\beta^2-L_1^{-2}}\frac{1-\exp(-\beta d)\left[\cosh\left(\frac{d}{L_1}\right)+\frac{1}{\beta L_1}\sinh\left(\frac{d}{L_1}\right)\right]}{\cosh\left(\frac{d}{L_1}\right)+\frac{k_{1,c}}{L_1}\left(\frac{1}{G}+\frac{L_2}{k_2}\right)\sinh\left(\frac{d}{L_1}\right)}\right|^2 \times$$

$$\left|-\left(\frac{1}{2C_1v_1}+\frac{1}{4G}\right)\int d\omega C_{\omega,2}v_{\omega,2}T'_{\omega}\frac{2}{1+i\varphi_{\omega,2}+\sqrt{\left(1+i\varphi_{\omega,2}\right)^2+\eta_{\omega,2}^2}}+\right.$$

$$\left.\frac{L_2}{k_2}\frac{1}{4}\int d\omega C_{\omega,2}v_{\omega,2}\left\{\begin{array}{l}\frac{2L_2}{\Lambda_{\omega,2}}\left[1-\frac{1}{2i\eta_{\omega,2}}\left(\ln\left(1+i\varphi_{\omega,2}+i\eta_{\omega,2}\right)-\ln\left(1+i\varphi_{\omega,2}-i\eta_{\omega,2}\right)\right)\right]+\\ -\frac{2}{1+i\varphi_{\omega,2}+\sqrt{\left(1+i\varphi_{\omega,2}\right)^2+\eta_{\omega,2}^2}}+\frac{2L_2}{\Lambda_{\omega,2}}\left[1-\frac{1}{2\pi}\int d\Omega\Theta(\mu_z)\frac{1}{\mu_z A_2\Lambda_{\omega,2}+\mu_z\Lambda_{\omega,2}/L_2}\right]+\\ R'_{\omega}\frac{2}{1+i\varphi_{\omega,2}+\sqrt{\left(1+i\varphi_{\omega,2}\right)^2+\eta_{\omega,2}^2}}\left[1-\frac{1}{\pi}\int d\Omega\Theta(\mu_z)\frac{\mu_z}{\mu_z A_2\Lambda_{\omega,2}+\mu_z\Lambda_{\omega,2}/L_2}\right]\end{array}\right\}\right|^2 \tag{5.25}$$

where the remaining solid angle integrals are calculated analytically to yield:

$$\frac{1}{2\pi}\int d\Omega\Theta(\mu_z)\frac{1}{\mu_z A_2\Lambda_{\omega,2}+\mu_z\Lambda_{\omega,2}/L_2}=\frac{1}{\sqrt{\left(\frac{\Lambda_{\omega,2}}{L_2}\right)^2-\eta_{\omega,2}^2}}\left\{\begin{array}{l}\ln\left[\sqrt{\left(\frac{\Lambda_{\omega,2}}{L_2}\right)^2-\eta_{\omega,2}^2}\left(1+i\varphi_{\omega,2}+\frac{\Lambda_{\omega,2}}{L_2}\right)+\left(\frac{\Lambda_{\omega,2}}{L_2}\right)^2-\eta_{\omega,2}^2+\frac{\Lambda_{\omega,2}}{L_2}\left(1+i\varphi_{\omega,2}\right)\right]+\\ -\ln\left[\sqrt{\left(\frac{\Lambda_{\omega,2}}{L_2}\right)^2-\eta_{\omega,2}^2}\sqrt{\left(1+i\varphi_{\omega,2}\right)^2+\eta_{\omega,2}^2}+\frac{\Lambda_{\omega,2}}{L_2}\left(1+i\varphi_{\omega,2}\right)\right]\end{array}\right\}$$

$$\frac{1}{\pi}\int d\Omega\Theta(\mu_z)\frac{\mu_z}{\mu_z A_2\Lambda_{\omega,2}+\mu_z\Lambda_{\omega,2}/L_2}=\frac{2}{\left(\frac{\Lambda_{\omega,2}}{L_2}\right)^2-\eta_{\omega,2}^2}\left\{\frac{\Lambda_{\omega,2}}{L_2}-\frac{\eta_{\omega,2}^2}{1+i\varphi_{\omega,2}+\sqrt{\left(1+i\varphi_{\omega,2}\right)^2+\eta_{\omega,2}^2}}\right\}+ \tag{5.26}$$

$$-\frac{2\frac{\Lambda_{\omega,2}}{L_2}\left(1+i\varphi_{\omega,2}\right)}{\left[\left(\frac{\Lambda_{\omega,2}}{L_2}\right)^2-\eta_{\omega,2}^2\right]\sqrt{\left(\frac{\Lambda_{\omega,2}}{L_2}\right)^2-\eta_{\omega,2}^2}}\left\{\begin{array}{l}\ln\left[\sqrt{\left(\frac{\Lambda_{\omega,2}}{L_2}\right)^2-\eta_{\omega,2}^2}\left(1+i\varphi_{\omega,2}+\frac{\Lambda_{\omega,2}}{L_2}\right)+\left(\frac{\Lambda_{\omega,2}}{L_2}\right)^2-\eta_{\omega,2}^2+\frac{\Lambda_{\omega,2}}{L_2}\left(1+i\varphi_{\omega,2}\right)\right]+\\ -\ln\left[\sqrt{\left(\frac{\Lambda_{\omega,2}}{L_2}\right)^2-\eta_{\omega,2}^2}\sqrt{\left(1+i\varphi_{\omega,2}\right)^2+\eta_{\omega,2}^2}+\frac{\Lambda_{\omega,2}}{L_2}\left(1+i\varphi_{\omega,2}\right)\right]\end{array}\right\}$$

The mathematical minimization of the penalty as a function of the substrate conductivity is not possible to do analytically due to the complex way in which the conductivity appears in the solid angle integrals through the thermal penetration depth, and thus will yield a transcendental equation. Instead, we numerically input various values of the conductivity over a broad range from 0 to twice the bulk value, and find the value which minimizes the penalty for every given value of the modulation frequency. We chose twice the bulk value as the upper limit to allow for

the possibility of seeing a conductivity which is larger than the macroscopic value, as we saw possible for the MFP filter transmission models previously. For simplicity, we present results in the limit of no in-plane length scale, such that the transport is strictly one-dimensional in the cross plane direction. In future work, we will explore the results with an in-plane length scale such as with a grating or with a superposition of gratings to create a Gaussian beam spot.

The choice of no in-plane length scale here is not only due to simplicity, but also for testing the strength of the size effect from the modulation frequency. For large values of the modulation frequency, this yields small values of the thermal penetration depth, and the expectation is that when it is on the order of the MFP of the phonons in silicon for the substrate, the thermal conductivity will be reduced. If there is also an in-plane length scale, the effective conductivity will already be reduced due to the effective reduction in the MFP of the phonons due to the in-plane length. Therefore, it will take even higher modulation frequencies to see size effects when there are in-plane length scales. Therefore, the onset of size effects due to the modulation frequency will be at the lowest frequency when the transport is one-dimensional in the cross plane direction and there are no in-plane length scales. So we take the limit of q to be zero to remove the grating. The interface conductance from Eq. (5.19) simplifies to:

$$G = \frac{\frac{1}{4}\int d\omega C_{\omega,2} \mathrm{v}_{\omega,2} \mathrm{T}'_{\omega}}{1 - \frac{\int d\omega C_{\omega,2} \mathrm{v}_{\omega,2} \mathrm{T}'_{\omega}}{2C_1 \mathrm{v}_1} - \frac{\int d\omega C_{\omega,2} \mathrm{v}_{\omega,2} \Lambda_{\omega,2} \mathrm{T}'_{\omega}}{2\int d\omega C_{\omega,2} \mathrm{v}_{\omega,2} \Lambda_{\omega,2}}} \tag{5.27}$$

The penalty function of Eq. (5.25) simplifies to:

$$P(k_2) = \left| \frac{Q_0}{1-\exp(-\beta d)} \frac{\beta^2}{\beta^2 - L_1^{-2}} \frac{1-\exp(-\beta d)\left[\cosh\left(\frac{d}{L_1}\right) + \frac{1}{\beta L_1}\sinh\left(\frac{d}{L_1}\right)\right]}{\cosh\left(\frac{d}{L_1}\right) + \frac{k_{1,c}}{L_1}\left(\frac{1}{G} + \frac{L_2}{k_2}\right)\sinh\left(\frac{d}{L_1}\right)} \right|^2 \times$$

$$\left| -\left(\frac{1}{2C_1 \mathrm{v}_1} + \frac{1}{4G}\right)\int d\omega C_{\omega,2} \mathrm{v}_{\omega,2} \mathrm{T}'_{\omega} \frac{1}{1+i\varphi_{\omega,2}} + \right.$$

$$\left. \frac{L_2}{k_2}\frac{1}{4}\int d\omega C_{\omega,2} \mathrm{v}_{\omega,2} \left\{ -\frac{\mathrm{T}'_{\omega}}{1+i\varphi_{\omega,2}} + \frac{2L_2}{\Lambda_{\omega,2}} \frac{\mathrm{T}'_{\omega} + 2i\varphi_{\omega,2}}{1+i\varphi_{\omega,2}} - 2\mathrm{T}'_{\omega}\left(\frac{L_2}{\Lambda_{\omega,2}}\right)^2 \ln\left(1 + \frac{\Lambda_{\omega,2}}{L_2}\frac{1}{1+i\varphi_{\omega,2}}\right) \right\} \right|^2 \tag{5.28}$$

Performing the numerical minimization yields the substrate conductivity as a function of modulation frequency. Figure 5-7 below shows effective conductivity normalized to the bulk value of silicon. We note that there are size effects that occur even starting around 100 kHz. For simplicity, we have taken a gray transmission value of unity to allow phonons to pass through the interface and not create an artificial filtered scenario. Furthermore, if we take too small of a value for the transmission, the surface temperature response will not be strongly sensitive to the transport in the substrate due to the lack of phonons passing through.

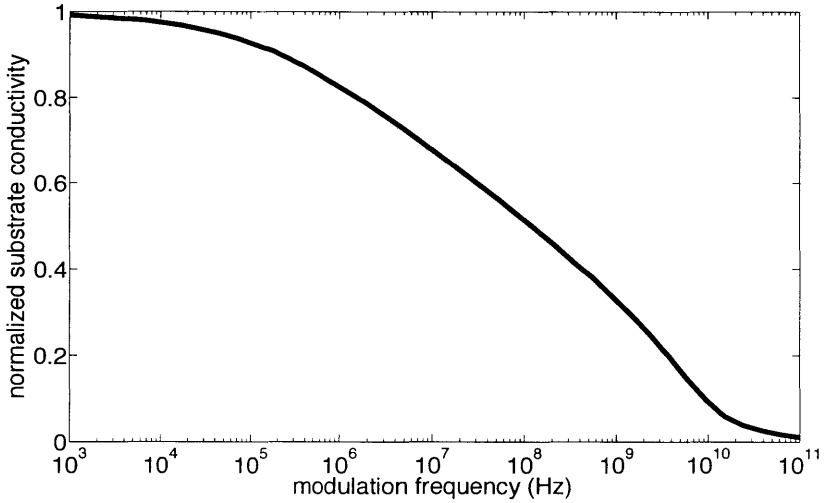

FIG. 5-7. Normalized effective conductivity of the substrate vs. modulation frequency.

We see that by 1 MHz, the effective conductivity is reduced by about 20%, and by 100 MHz, the conductivity is reduced by over 50%. This onset of the frequency occurs at frequencies that the experiment can access, as the FDTR frequencies measured can go as high as several hundred MHz. Of course, it is not enough to only observe the effective conductivity but the actual experimental observable of amplitude and phase to be able to see if this will be physically observed in an actual material. By calculating the thermal penetration depth, given by $\ell_2 = \sqrt{\frac{k_2}{\pi \nu C_2}}$, where k_2 is given by the effective substrate conductivity, not just the bulk value of silicon, we can also plot the effective conductivity as a function of the effective penetration depth in order to view the size effects in terms of a length scale. We see that the size effects in Fig. 5-8

below occur on the order of tens of microns, very similar to what we observed for the TTG in chapter 2 and chapter 3.

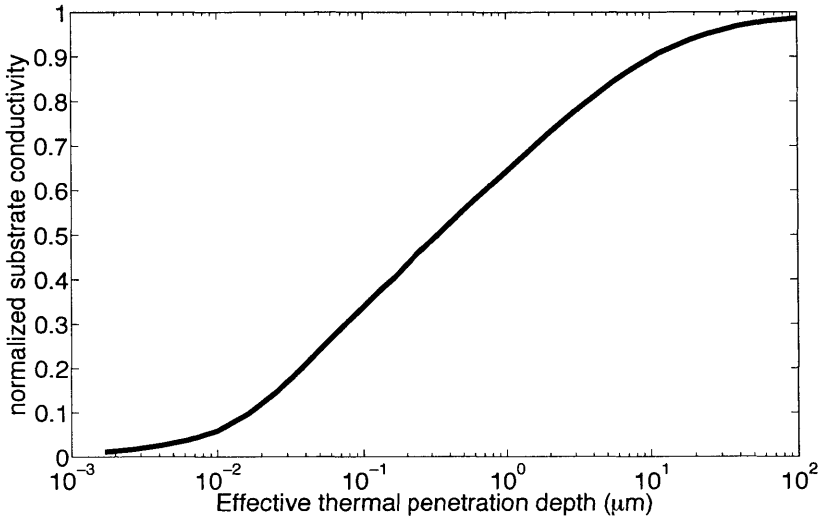

FIG. 5-8. Normalized effective conductivity of the substrate vs. penetration depth. The penetration depth utilizes the variational conductivity which is frequency dependent in it, as opposed to the bulk Fourier predicted penetration depth.

Utilizing this variational substrate conductivity, we also output the amplitude and phase response of the surface to see whether the experimental output is sensitive to the effect of the modulation frequency. Figure 5-9 shows the amplitude and phase response as a function of the modulation frequency.

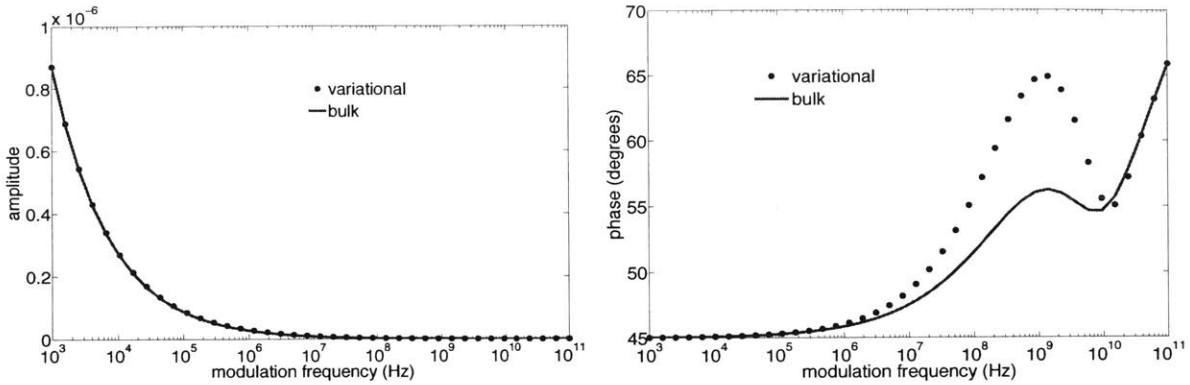

FIG. 5-9. Surface temperature response to the modulation frequency. The (a) amplitude and (b) phase are plotted to compare the variational solution vs. the bulk Fourier heat conduction equation solution.

We see that the amplitude is insensitive to the conductivity of the substrate, predicting negligibly different values whether we include the variational substrate conductivity or simply the bulk value of silicon conductivity. However, the phase shows strong effects starting at around 1 MHz, and showing the largest deviation around 1 GHz. With FDTR experiments on the order of tens and hundreds of MHz [31], it would seem that then it is possible to measure the size effect on the conductivity due to the modulation frequency by looking at the phase response of the metal surface.

5.4 Summary

In conclusion, in this chapter we extended the variational approach to be able to model the TDTR/FDTR geometry of a metal transducer on top of a substrate. By treating the interface conductance as well as the metal conductivity and substrate conductivity as variational parameters, we were able to approximately solve the BTE and study the effect of an in-plane thermal grating as well as the effect of a gray transmission vs. a MFP filter transmission on the interface conductance and substrate conductivity. We found that a spectral model of a filer for

the interface can yield very interesting behavior for the substrate conductivity, which we will explore in greater in the next chapter. Furthermore, we analyzed the effect of modulation frequency on the substrate conductivity as well as seeing the degree to which this is observed in the surface metal response for the simple gray transmission model. We found that the modulation frequency will result in size effects for the substrate conductivity so that the thermal penetration depth can be considered as a length scale for which at the micron scale, there should be size effects seen in silicon. Future work will include studying this for various transmission models that are more achievable in an actual interface between aluminum and silicon, and for a wider variety of materials, such as SiGe for which frequency dependence has been observed experimentally [32]. Then by comparing against the experimental data being reported in literature, we can really explain the different frequency dependence seen or not seen in certain materials and clarify the effect of the modulation frequency for nanoscale thermal transport. In the next chapter, we will explore in greater detail the effect of selecting which phonon are introduced into a system, as we saw with the interface acting as a filter in this chapter.

Chapter 6
Nonthermal phonon distributions and size effects

The previous chapter demonstrated that the interface can have a strong effect on the effective thermal conductivity of the substrate, especially when it can act as a filter for which phonons are introduced into the substrate. To study this effect in greater detail, we look at a simpler geometry for which this effect can be more easily characterized. We study the effect of the phonons contributing to transport by looking at what phonons are generated by a heating source. Thus far in literature, the distribution utilized has been the thermal distribution, which assumes that the heating emits phonons according to thermal equilibrium. This was the distribution utilized in Chapters 2 and 3, but we will explore nonthermal phonon distributions in this chapter to see what effect this can have on the effective thermal conductivity.

The one-dimensional sinusoidal thermal grating (TG) is one of the simplest geometries to study nondiffusive transport within the Boltzmann Transport equation. It served as a starting point for the variational approach [64] to demonstrate the ability to obtain an analytical effective thermal conductivity that allows for an accurate solution to the BTE over a wide range of grating periods., as was shown in chapter 2. It also demonstrated the need to characterize a material using not only the accumulation of thermal conductivity but also the accumulation of heat capacity, as we showed in chapter 4. Thus the simplicity of analysis as well as the richness of physics this geometry provides is invaluable. Here we study the one-dimensional grating in a steady state heating configuration. The beauty of this problem in the steady state in particular is that the BTE can be solved fully analytically with no approximations in this heat transfer configuration, allowing for a very efficient study of the system response. We aim to study the effect of the assumption of a thermal distribution for the heat pattern, compared to other spectral excitation of the phonons.

Utilizing the fundamental solution of the one-dimensional grating, an arbitrary steady-state heat source can be represented by a superposition of thermal gratings, and so we can construct any profile of interest. As an example, we will study a three-dimensional Gaussian source mimicking a "hot spot" that could be produced by osmic heating inside a microelectronic device

[79,80,87]. This will allow us to compare how the source heating phonon distribution affects thermal transport in a three-dimensional configuration, and how the size of a hot spot results in size effects on the thermal conductivity when the phonon distribution is far from the typical thermal distribution.

6.1 Thermal transport from a steady state 1D thermal grating with a general phonon source distribution

In this geometry, the volumetric heat generation profile is given by the functional form:

$$Q = \bar{Q} e^{iqx} \tag{6.1}$$

where q is the grating wavevector, and $\bar{Q}$ is the amplitude of the volumetric heat generation rate. In this case, the temperature profile will take on the function form:

$$T = T_0 + T_0 e^{iqx} \bar{h} \tag{6.2}$$

where $\bar{h}$ is a non-dimensional temperature amplitude we will use for convenience, and T_0 is the background reference temperature. The temperature amplitude $\bar{h}$ and heat generation amplitude $\bar{Q}$ are simply constants, so the differential equations will simply be algebraic equations to solve in this geometry. In this case, the Fourier heat conduction equation can be solved to obtain:

$$\bar{h} = \frac{\bar{Q}}{T_0} \frac{1}{kq^2} \tag{6.3}$$

We note that in a typical steady state heat transfer configuration without volumetric heat generation, the thermal conductivity doesn't appear in the heat conduction equation nor does it appear in the boundary conditions which are simply set temperatures at boundaries or for example adiabatic boundary conditions. In this case however, the thermal conductivity appears in a simple form and allows for the Fourier conduction solution to be matched to the solution of the BTE easily. This is due to the simplicity of a sinusoidal grating, which results in a sinusoidal temperature response both in the diffusive limit as well as in the BTE for any length scale.

To solve for the temperature response in the nondiffusive regime, we start with the isotropic BTE under the relaxation time approximation for this geometry:

$$\frac{\partial g_\omega}{\partial t} + \mathrm{v}_\omega \mu \frac{\partial g_\omega}{\partial x} = \frac{g_0 - g_\omega}{\tau_\omega} + \frac{Q_\omega}{4\pi} \tag{6.4}$$

The spectral volumetric heat generation term can be written as $Q_\omega = p_\omega Q$, where Q is the volumetric heat generation rate given previously, and p_ω if the fraction value that a given phonon is excited of that heat generation rate. The spatial and temporal distribution of Q_ω is given by the macroscopic heat generation rate Q, while p_ω only depends on the material properties and the details of the heating type, i.e. if it is with optical pumping. These fractions are normalized such that the sum over the branches and phonon frequencies add up to unity, i.e. $\int d\omega p_\omega = 1$. Given the sinusoidal pattern of the volumetric heating, the energy density will similarly be given by $g_\omega = \bar{g}_\omega(\mu) e^{iqx}$ and the equilibrium energy density can be given in terms of the temperature as $\bar{g}_0 = \frac{C_\omega T_0}{4\pi}\bar{h}$. Inserting these forms into the BTE yields an algebraic equation which can be solved to yield the non-equilibrium energy density in terms of the non-dimensional temperature analytically:

$$\bar{g}_\omega(\mu) = \frac{C_\omega T_0}{4\pi}\left(\bar{h} + \frac{\bar{Q}}{T_0}\frac{p_\omega \tau_\omega}{C_\omega}\right)\frac{1}{1 + i\eta_\omega \mu} \tag{6.5}$$

where we have defined the nondimensional number $\eta_\omega = q\Lambda_\omega$. We can also calculate the temperature equation from the BTE by integrating the BTE over the solid angle and phonon spectrum, yielding:

$$\int d\omega \int d\Omega \frac{g_0 - g_\omega}{\tau_\omega} = 0 \tag{6.6}$$

Inputting the solution to the BTE and utilizing the non-dimensional temperature, we obtain an algebraic equation for the temperature that can be analytically solved to yield:

$$\bar{h} = \frac{\bar{Q}}{T_0}\frac{1}{q^2}\frac{\int d\omega p_\omega g(\eta_\omega)}{\frac{1}{3}\int d\omega C_\omega \mathrm{v}_\omega \Lambda_\omega f(\eta_\omega)} \tag{6.7}$$

where the kernel functions are given by:

$$f(\eta_\omega)=\frac{3}{\eta_\omega^2}\left\{1-\frac{1}{\eta_\omega}\arctan(\eta_\omega)\right\}$$
$$g(\eta_\omega)=\frac{1}{\eta_\omega}\arctan(\eta_\omega) \tag{6.8}$$

Note these kernels are identical to that from the one-dimensional TTG with a delta pulse heating [64]. By matching the exact temperature solution of the BTE to that of the Fourier heat conduction equation, an effective conductivity can be extracted given by:

$$k=\frac{\frac{1}{3}\int d\omega C_\omega v_\omega \Lambda_\omega f(\eta_\omega)}{\int d\omega p_\omega g(\eta_\omega)} \tag{6.9}$$

The spectral heat generation fractions p_ω have been left arbitrary, but the specific form of a thermal distribution is given by $p_\omega = C_\omega / C$, which is weighted by the spectral heat capacity, and not the ratio of the spectral heat capacity to the relaxation time as given in literature [47]. We utilize the index ω as short hand notation to denote a phonon of a given branch and frequency. Thus for this simple steady state geometry, we demonstrate an exact matching of the Fourier and BTE temperature profiles, yielding an effective thermal conductivity given by the result from the one-dimensional limit of the TTG [64]. We note here that the appearance of the heat capacity has arisen for the thermal distribution not due to the fact that the configuration is transient, but due to the weighting of the spectral heat generation rate. Furthermore, with the denominator term depending on the differential heat capacity, we see the appearance of the accumulation of heat capacity even in a steady state heat transfer configuration once we convert the integration over the phonon modes into an integration over the MFPs. More accurately, we see that it is the accumulation of the source phonon distribution in the case of nonthermal distributions. Thus for proper reconstruction of the thermal conductivity accumulation, as outlined in Chapter 4, we require the accumulation of the source distribution as well from the denominator. The one-dimensional grating configuration demonstrates that the effective thermal conductivity depends on the accumulation of thermal conductivity as well as the accumulation of heat capacity, regardless of whether the heating is due to a delta pulse or due to steady state heating, so long as the heating is given by a thermal distribution.

6.2 The optical source distribution

Here we explore the assumptions of a thermal distribution, and compare to other forms of excitation of the phonons. Realistically, the excitation of phonons is due to optical pumping, and this heating profile will preferentially excite optical phonons. Thus two specific forms we can compare are:

$$p_{\omega}^{thermal} = \frac{C_{\omega}}{C}$$

$$p_{\omega}^{optical} = \begin{cases} 0 & \omega \in \text{acoustic branch} \\ \dfrac{C_{\omega}}{C_{optical}} & \omega \in \text{optical branch} \end{cases} \tag{6.10}$$

The thermal distribution considers all phonons to be excited according to their contribution to the spectral heat capacity. The optical distribution we take assumes a value of zero for all of the acoustic branches, and weights the modes in the optical branches by their corresponding spectral heat capacity. Both distributions are of course properly normalized to unity. Figure 6-1 shows the comparison between these two distributions.

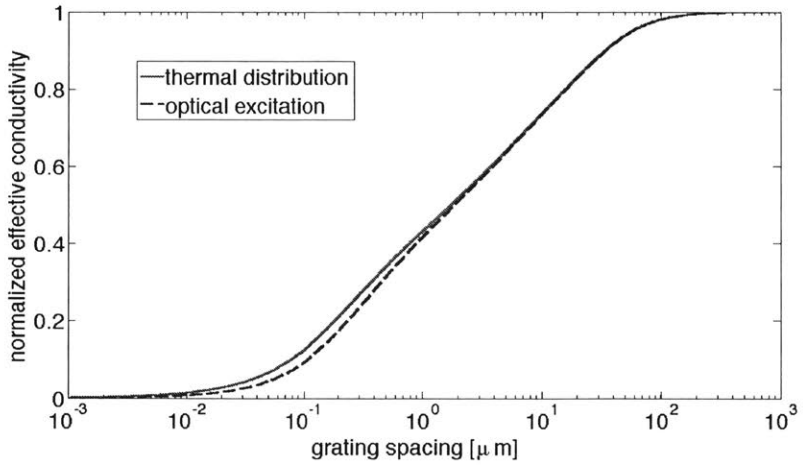

FIG. 6-1. Comparison of the normalized effective thermal conductivities for the thermal distribution vs. the optical excitation.

We see that the difference between the two is negligible are large grating spacings. However, below 1 micron, we see a deviation of the optical case vs. the thermal distribution. Also note that the optical excited distribution is always smaller than the thermal distribution, and thus for the typical case of laser heating, the assumption of a thermal distribution over-predicts the output compared to an optical distribution.

To more quantitatively demonstrate the deviation, we show in Fig. 6-2 the ratio of the optical distribution to the thermal distribution.

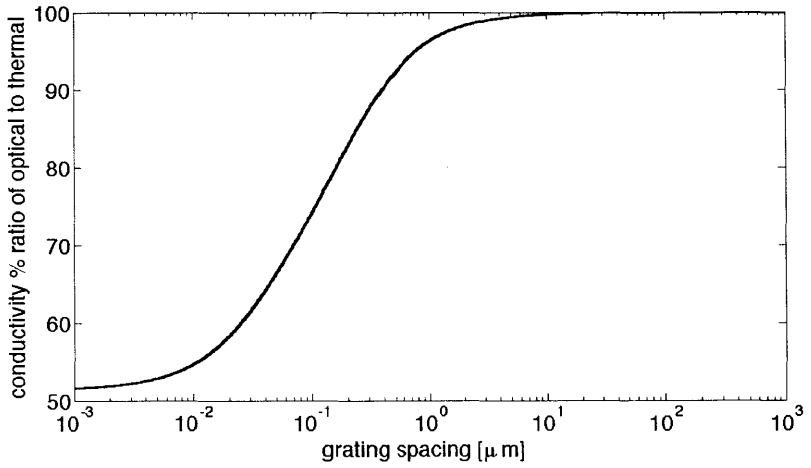

FIG. 6-2. Ratio of the optical distribution conductivity to the thermal distribution conductivity to quantitatively demonstrate at 1 micron and below, the difference is greater than 5% between the two conductivities.

Quantitatively, we can now see that the optical distribution deviates by more than 5% below a grating spacing of 1 micron. The difference between the optical distribution vs. the thermal distribution is bigger for shorter grating periods, which is when the denominator of the thermal conductivity has a stronger effect and the specific form of the heat generation fractions make a difference. Given that TTG experiments using extreme ultraviolet (EUV) excitation can now achieve gratings in the tens and hundreds of nanometer range, the consideration of optical excitation vs. assuming a thermal distribution is important for accurate modeling of the thermal transport [77,78].

To explore other forms of such excitations, we consider the following two additional heating distributions:

$$p_{\omega}^{uniform} = \frac{1}{\int d\omega}$$

$$p_{\omega}^{optical-uniform} = \begin{cases} 0 & \omega \in \text{acoustic branch} \\ \dfrac{1}{\int d\omega_{optical}} & \omega \in \text{optical branch} \end{cases} \tag{6.11}$$

These two forms are to see whether there is a large effect from the specific form for a given branch being uniformly excited for the phonons in that branch or whether they should be weighted by their spectral heat capacity. Figure 6-3 shows the effects of these additional distributions.

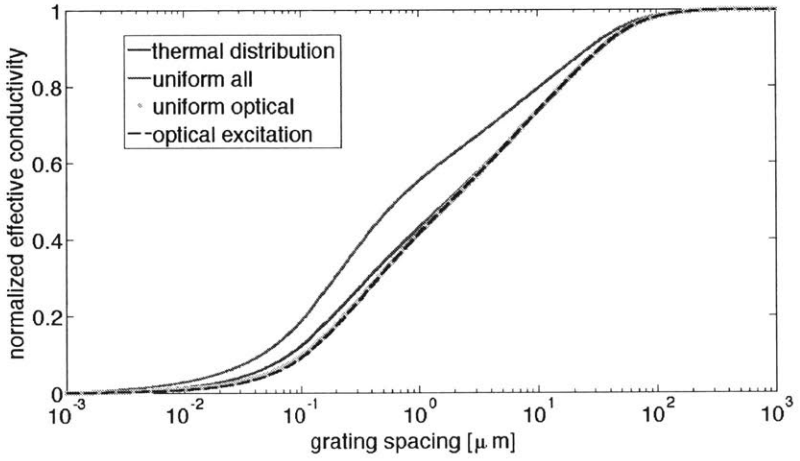

FIG. 6-3. Joint comparison of thermal, optical, and also the uniform excitations of all modes vs. only uniformly exciting optical modes.

We note that there does not seem to be a large difference between the cases of the optical distribution, which weights the optical phonons only by their spectral heat capacity, vs. the uniform optical distribution which just weights all optical phonons evenly (but gives zero for the fraction for acoustic branch phonons). However, when comparing the full phonon distribution using the thermal distribution, weighting all phonons by their spectral heat capacity, vs.

weighting all phonons uniformly, there is a very clear discrepancy. This can be explained easily utilizing the density of states (DOS). The phonons of low frequency near the zone center have large MFPs and also large group velocities. Due to the large group velocity of these acoustic branch phonons, their DOS is small, and thus by weighing these phonons by the DOS, their contribution is smaller. By utilizing a uniform distribution, their relative contribution is much higher than that of the thermal distribution, and so the uniform heating generates an effective thermal conductivity larger than that of the thermal distribution.

6.3 Nonthermal extremes and optimizing the effective thermal conductivity

In this section, we wish to explore what type of excitation can maximize or minimize the effective thermal conductivity. More specifically, for a given grating period, what should the values p_ω be in order to maximize or minimize the effective thermal conductivity k. The denominator of the effective thermal conductivity is the only term we need to consider, shown in Eq. (6.9). Given that the kernel g is a monotonically decreasing function of the ratio of MFP to grating period, essentially the maximum thermal conductivity is achieved with the minimum denominator, which is the case for which the phonon modes with the largest MFP are excited. The minimum effective thermal conductivity is achieved for the largest denominator, which is the case when the phonon modes with the smallest MFP are excited. This is intuitive in the kinetic picture of thermal conductivity, where a phonon with the larger MFP contributes greater to the thermal conductivity, and thus a large MFP phonon that is excited will yield a higher prediction than the thermal excited distribution, while a small MFP phonon that is excited will yield a smaller prediction than the thermal excitation. Mathematically, these low and high MFP filter distributions are given by:

$$p_{\omega}^{\text{low filter}}(\Lambda) = \frac{C_{\omega}\Theta(\Lambda - \Lambda_{\omega})}{\int d\omega' C_{\omega'}\Theta(\Lambda - \Lambda_{\omega'})}$$
$$p_{\omega}^{\text{high filter}}(\Lambda) = \frac{C_{\omega}\Theta(\Lambda_{\omega} - \Lambda)}{\int d\omega' C_{\omega'}\Theta(\Lambda_{\omega'} - \Lambda)} \tag{6.12}$$

By filtering and selecting out the single phonon of highest MFP and lowest MFP, we compare against the thermal distribution. Fig. 6-4 shows the comparison of the lowest MFP being excited compared to the thermal distribution and the optical distribution excited proportional to the spectral heat capacity.

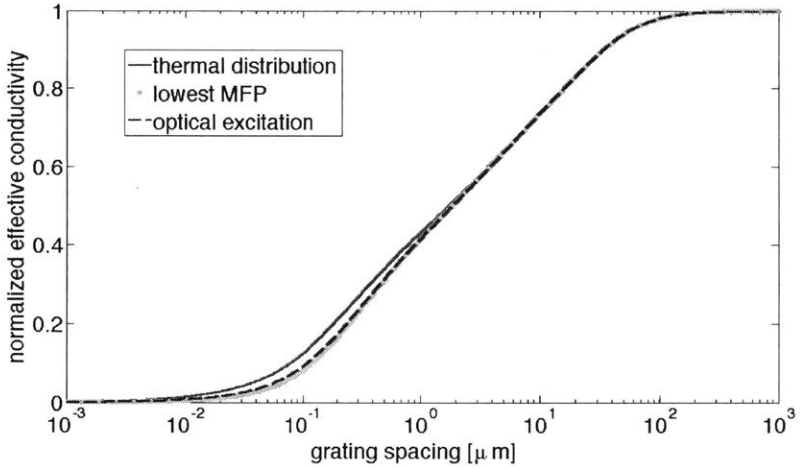

FIG. 6-4. The comparison of the cases for thermal distribution, optical excitation, and just the lowest MFP mode excited. We see that there is negligible difference between the excitation of only the lowest MFP phonon mode vs. exciting all optical modes according to their contribution to the spectral heat capacity.

The lowest MFP for silicon was approximately 1.8 nm, and so for that single phonon mode excited, we see negligible difference compared to that of just the optical excitation.

The results for the high MFP show far more interesting behavior. Figure 6-5 shows the effective thermal conductivity for filtering for high MFPs, and only exciting those above a threshold value of MFP.

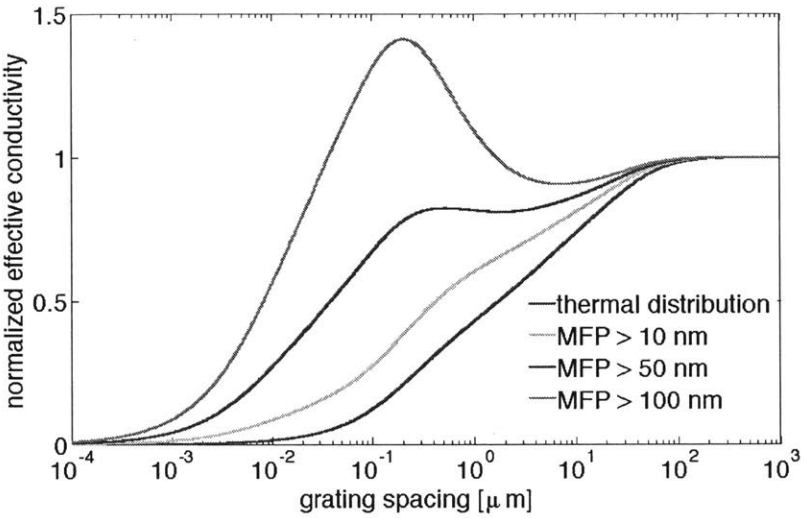

FIG. 6-5. Comparison for exciting phonons above a threshold MFP. All phonons above 10 nm, 50 nm, and 100 nm threshold cases are considered. At 50 nm, we see the appearance of non-monotonic behavior in the effective thermal conductivity. For 100 nm, we see not only non-monotonic behavior, but also an enhancement of the thermal conductivity beyond bulk.

We note that indeed the effective thermal conductivities of these distributions are always greater than the thermal distribution. The case of only exciting MFPs greater than 10 nm shows an increase, but then for higher threshold MFPs, more interesting behavior is revealed. For above 50 nm, we start to see non-monotonic behavior in the effective thermal conductivity as a function of the grating period. Furthermore, for larger than 100nm, we see not only non-monotonic behavior, but an effective thermal conductivity larger than the bulk thermal conductivity. The peak value of the effective conductivity consistently appears around 100 – 200nm for the grating period, no matter the value of the threshold MFP cutoff.

Taking this to the extreme, we excite only the phonon of the largest MFP, of approximately 16.7 micron value. Figure 6-6 shows this extreme scenario which optimizes the effective thermal conductivity for silicon in this heat transfer geometry.

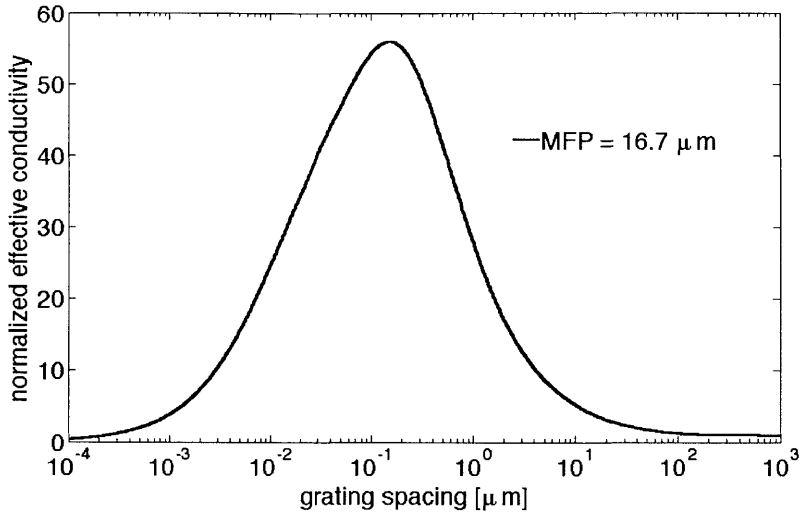

Fig. 6-6. The normalized effective thermal conductivity when only the largest MFP phonon mode is excited of approximately 16.7 micron.

A maximum value of 56 times the bulk thermal conductivity is capable of being achieved, around a grating period of 100 nm. The intuitive reason why this enhancement is possible can also be explained within a kinetic picture. Only the phonon of largest MFP is excited, and so this phonon propagates and the Fourier temperature profile that would mimic this effect in the BTE will be one with a thermal conductivity that is predicted far higher than that of the of the thermal distribution when phonons of both low and high MFPs are excited.

6.4 Pseudo temperature vs. real temperature

One of the flaws of the RTA is that it doesn't strictly conserve energy. Thus, the temperature provided by Eq. (6.7) is not the only definition of temperature in this case. One can also define another definition of temperature based on the energy density. Given the volumetric energy density, obtained from the non-equilibrium spectral energy density, $U = \int d\omega \int d\Omega g_\omega$, we define the real temperature, h_U, by taking the ratio of this energy density to the heat capacity. This

temperature also has a spatially sinusoidal dependence as $h_U = \bar{h}_U e^{iqx}$. By integrating over the phonon modes and the solid angle the non-equilibrium spectral energy density of Eq. (6.5), we obtain:

$$\bar{h}_U = \bar{h}\int d\omega \frac{C_\omega}{C}\frac{1}{\eta_\omega}\arctan(\eta_\omega) + \frac{\bar{Q}}{T_0}\int d\omega p_\omega \frac{\tau_\omega}{C}\frac{1}{\eta_\omega}\arctan(\eta_\omega) \tag{6.13}$$

Inserting the solution solved for the pseudo temperature from Eq. (6.7), we obtain for the real temperature:

$$\bar{h}_U = \frac{\bar{Q}}{T_0}\frac{1}{q^2}\frac{\left\{\int d\omega \frac{C_\omega}{C}\frac{\arctan(\eta_\omega)}{\eta_\omega}\right\}\left\{\int d\omega p_\omega \frac{\arctan(\eta_\omega)}{\eta_\omega}\right\} + \left\{\int d\omega \frac{C_\omega}{\tau_\omega}\left[1-\frac{\arctan(\eta_\omega)}{\eta_\omega}\right]\right\}\left\{\int d\omega p_\omega \frac{\tau_\omega}{C}\frac{\arctan(\eta_\omega)}{\eta_\omega}\right\}}{\frac{1}{3}\int d\omega C_\omega v_\omega \Lambda_\omega \frac{3}{\eta_\omega^2}\left[1-\frac{\arctan(\eta_\omega)}{\eta_\omega}\right]} \tag{6.14}$$

An effective thermal conductivity, k_U, is identified by matching this temperature to the Fourier temperature of Eq. (6.3), to obtain:

$$k_U = \frac{\frac{1}{3}\int d\omega C_\omega v_\omega \Lambda_\omega \frac{3}{\eta_\omega^2}\left[1-\frac{\arctan(\eta_\omega)}{\eta_\omega}\right]}{\left\{\int d\omega \frac{C_\omega}{C}\frac{\arctan(\eta_\omega)}{\eta_\omega}\right\}\left\{\int d\omega p_\omega \frac{\arctan(\eta_\omega)}{\eta_\omega}\right\} + \left\{\int d\omega \frac{C_\omega}{\tau_\omega}\left[1-\frac{\arctan(\eta_\omega)}{\eta_\omega}\right]\right\}\left\{\int d\omega p_\omega \frac{\tau_\omega}{C}\frac{\arctan(\eta_\omega)}{\eta_\omega}\right\}} \tag{6.15}$$

In the limit of a gray medium, where the group velocities and relaxation times are assumed to be independent of the phonon dispersion and take on a single value, then the pseudo-temperature based thermal conductivity of Eq. (6.9) and the real-temperature based thermal conductivity of Eq. (6.15) match exactly. However, for the full spectral consideration, these have different functional forms.

Figure 6-7 shows the comparison between the thermal conductivity obtained from matching the temperature obtained from the equilibrium energy density, denoted the pseudo-temperature, and the 'real' temperature based on the nonequilibrium energy definition. We see that for the case of a thermal distribution, the two temperatures are quite similar.

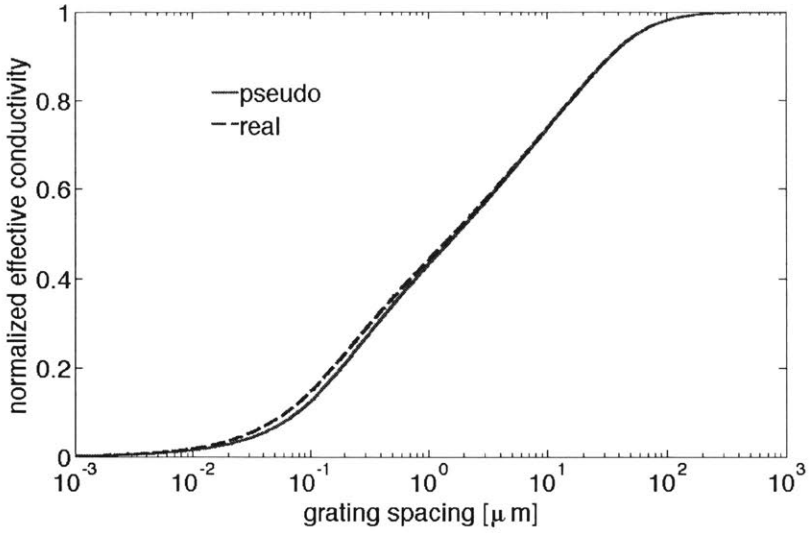

Fig. 6-7. Comparison between the effective thermal conductivities based on matching the pseudo temperature to the Fourier temperature and also matching the 'real' temperature (based on the non-equilibrium energy density) to the Fourier temperature. The deviation of the pseudo based conductivity is at most 20% from the real temperature based conductivity, occurring around 10 to 100 nm.

We also look at the extremal conductivities, obtained by exciting the phonons with the largest MFP, and smallest MFP, respectively. While the MFP filter distribution is no longer rigorously the distribution which optimizes the effective conductivity of Eq. (6.15) from the energy density, we observe the effect it has nonetheless. Figure 6-8 shows the excitation of only the shortest MFP phonon with both definitions of the temperature. Again, they show comparable predictions for the thermal conductivity.

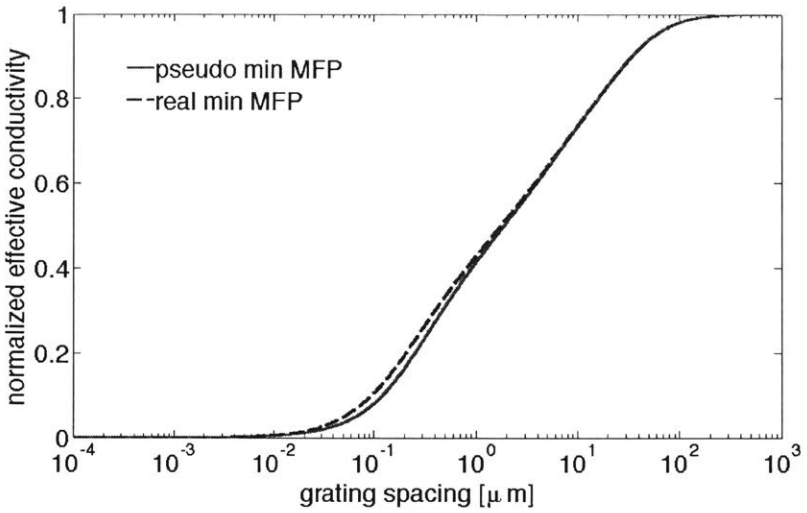

Fig. 6-8. The effective thermal conductivity from the pseudo temperature as well as the real temperature when only the shortest MFP phonon is excited by the heating.

Lastly, we show the scenario of only the maximum MFP phonon being excited. Figure 6-9 shows that the effective thermal conductivity demonstrates non-monotonic behavior, as well as enhancement beyond the bulk thermal conductivity for the real temperature as well. However, the real temperature based effective thermal conductivity does not show as high of an enhancement, indicating that the pseudo temperature predicts a lower temperature compared to the real temperature defined from the non-equilibrium energy density.

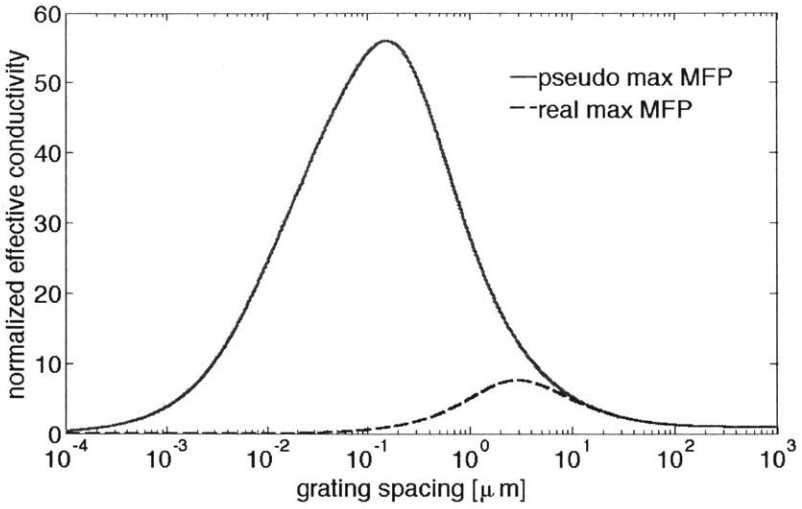

Fig. 6-9. Comparison of the effective thermal conductivities for the excitation of only the phonon mode with the largest MFP in silicon, of value 16.7 micron. Both definitions of the temperature show an enhancement beyond bulk and non-monotonic behavior in the effective thermal conductivity. The pseudo temperature predicts a maximum enhancement of 56 times that of the bulk thermal conductivity, while the real temperature based effective conductivity predicts a maximum of nearly 8 times that of bulk.

The difference between the two definitions of the thermal conductivity are much larger for the maximum MFP thermal conductivities than for the thermal distribution for the thermal conductivities as shown in Fig. 6-9. Furthermore, the grating period for which this maximum occurs is at approximately 200 nm for the pseudo temperature based effective conductivity, but around 3 micron for the real temperature based effective conductivity. This highlights the importance of using the physical observable of energy density to understand thermal transport as opposed to a pseudo temperature, especially when the phonon source distribution is a non-thermal extreme.

6.5 3D hotspot thermal transport with nonthermal phonon distributions

The thermal grating provides a simple one-dimensional geometry with which we could quantify the effect of the various phonon source distributions. Furthermore, an arbitrary steady state source can be represented as a superposition of gratings via the Fourier transform. As an example, we now consider a three-dimensional steady state hot spot, which can be produced, for example, by ohmic heating inside a microelectronic device. We consider a heat source described by a radial Gaussian, given by $Q = \bar{Q}\frac{1}{R^3(2\pi)^{\frac{3}{2}}}\exp\left(-\frac{r^2}{2R^2}\right)$ in 3D space. R defines the size of the hot spot, and $\bar{Q}$ represents the power being deposited into the system. We will use the energy density at the center of the hot spot, i.e. $r = 0$ to compare the predictions of the BTE and Fourier heat conduction equations. Utilizing the spatial Fourier transform of the radial Gaussian, the heat generation rate can be written as a superposition of 1D thermal gratings as $Q = \frac{1}{(2\pi)^3}\int e^{i\vec{q}\cdot\vec{r}}\bar{Q}\exp\left(-\frac{q^2R^2}{2}\right)d^3q$. Taking a superposition of the one-dimensional grating solution, weighted by the coefficients of the Fourier transform for the radial Gaussian, we obtain the energy density at the center of the Gaussian hot spot:

$$U_{\text{BTE}}(r=0) = \bar{Q}\frac{1}{2\pi^2}\frac{1}{R^3}\int_0^\infty dt\exp\left(-\frac{t^2}{2}\right)t^2\left\{\frac{\int d\omega p_\omega \tau_\omega \frac{\arctan(t\eta_\omega)}{t\eta_\omega} + \left[\int d\omega p_\omega \frac{\arctan(t\eta_\omega)}{t\eta_\omega}\right]\left[\int d\omega C_\omega \frac{\arctan(t\eta_\omega)}{t\eta_\omega}\right]}{\int d\omega \frac{C_\omega}{\tau_\omega}\left[1-\frac{\arctan(t\eta_\omega)}{t\eta_\omega}\right]}\right\} \quad (6.16)$$

$$U_{\text{Fourier}}(r=0) = \bar{Q}\frac{1}{\alpha R}\frac{1}{(2\pi)^{\frac{3}{2}}}$$

The isotropy of the system allowed us to analytically compute the integral over the solid angle, reducing the 3D inverse Fourier transform integral into an integral over the radial variable. We defined the nondimensional variables $t = qR$ and $\eta_\omega = \Lambda_\omega / R$ to simplify the expression.

Figure 6-10 shows the energy density from the Fourier heat conduction equation as well as from the BTE for several source distributions. The energy density is taken at the center of the hot spot as a function of the size of the hot spot R, with a given input power of $\bar{Q} = 1\,\mu\text{W}$. While the energy density at the center increases with decreasing spot size as the energy is more concentrated at the center, for spot sizes near 300 nanometers, the high MFP filter distribution with the 16 micron threshold yields an energy density an order of magnitude lower than that of the thermal distribution, and 5 times lower than predicted by the heat equation.

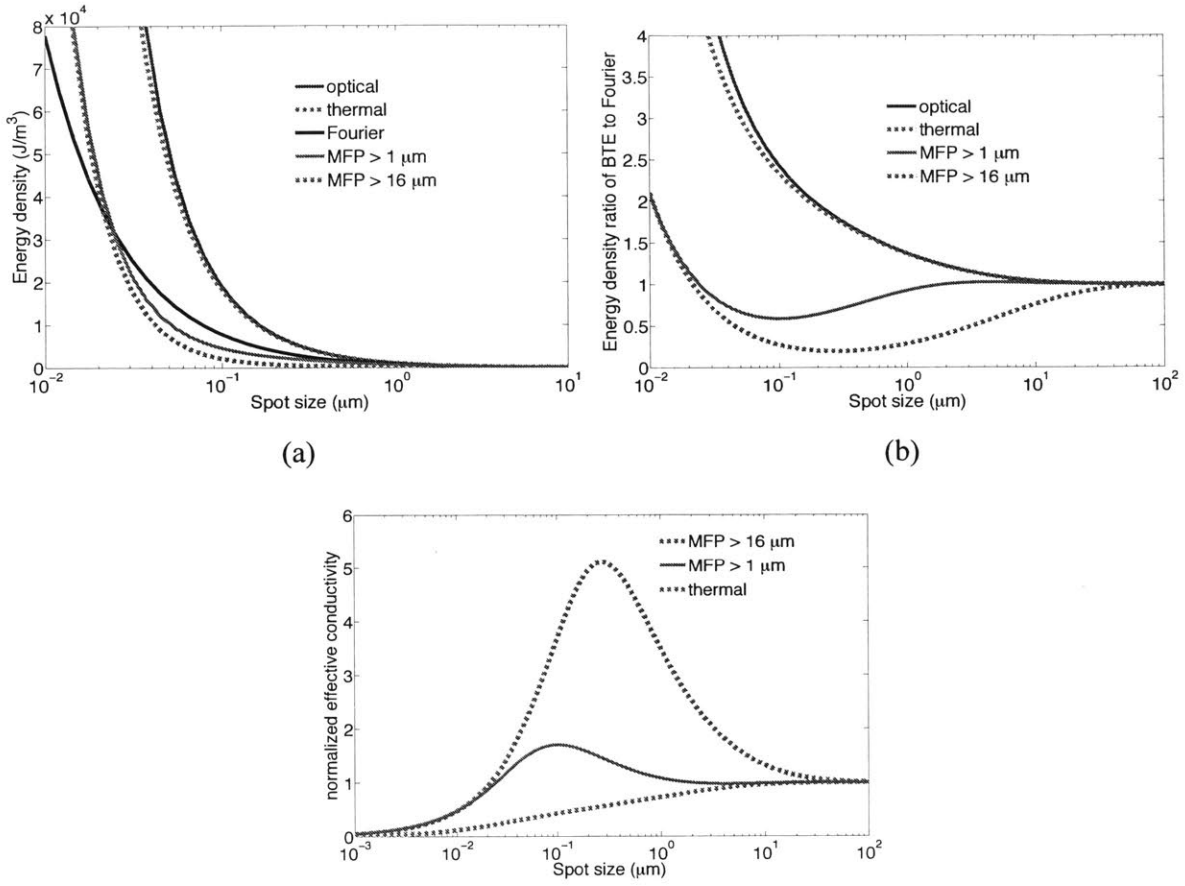

Fig. 6-10. Heat transport from a 3D Gaussian hot spot for different phonon source distributions vs. the size of the hot spot. Plotted are (a) the energy density for a given input power, (b) the energy density relative to that given by Fourier's law, and (c) the effective conductivity relative to that given by Fourier's law.

By matching the energy densities at the center of the hot spot $r = 0$, we define a normalized effective thermal conductivity for the 3D Gaussian hot spot, obtained by taking the ratio of the Fourier energy density to the BTE energy density from Eq. (6.16), i.e. $\kappa_{\text{hot spot}} \equiv U_{\text{Fourier}}(r=0)/U_{\text{BTE}}(r=0)$. We see a factor of 5 times enhancement in the effective thermal conductivity at 300nm in Fig. 6-10. The high MFP distribution predicts an energy

density that is lower than the prediction from the Fourier heat conduction equation for spot sizes of approximately 20nm and larger.

6.6 Summary

In conclusion, we have investigated the effect of the phonon distribution produced by a small heat source on nondiffusive thermal transport. By comparing the energy density in response to volumetric heating from the BTE and from the Fourier heat conduction equation for a 1D thermal grating as well as for a 3D Gaussian hot spot, we have dispelled the notion that the size effect always leads to a reduction in thermal transport compared to the prediction of Fourier's law. Depending on the source phonon distribution, the size effect can reduce or enhance thermal transport; in the latter case, the effective micro/nanoscale thermal conductivity can become larger than the regular macroscale conductivity, similar to what we see in chapter 5 with an interface that only allows transmission of high MFP phonons into the substrate. We believe that a source predominantly generating long-MFP phonons and thus yielding enhanced thermal transport could be realized in practice. For example, in ohmic heating of a semiconductor device, the distribution of phonons excited is determined by the electron-phonon interaction. Intraband electron-phonon scattering, which typically plays a dominant role in the resistivity of semiconductors at room temperature, involves small-wavevector phonons at the center of the Brillouin zone, which will include long-MFP acoustic phonons [88]. If the predominant emission of such long-MFP phonons could enhance thermal transport from nanoscale hot spots, this would have significant implications for the thermal management of microelectronic devices.

Chapter 7
Conclusions and future outlook

This thesis has provided a new, variational framework with which to understand thermal transport in the nanoscale regime, especially related to recent efforts to extract phonon mean free path distributions based on TTG and TDTR/FDTR experiments. This approach has provided the ability to obtain analytical effective thermal conductivities in various geometries of interest for experimental work, by utilizing insight that the experimental output can be represented by the same Fourier temperature distribution, but with an effective thermal conductivity that differs from the bulk, macroscopic value of the conductivity. Furthermore, the analytical expressions obtained have given insight beyond that which a numerical approach could provide: it has allowed insight into the importance of the accumulation of heat capacity in addition to the accumulation of thermal conductivity as the material properties that comprise the effective thermal conductivity in a nanostructured material.

The variational framework has provided not only the ability to explain experimental output, but the ability to predict it. This approach utilizes no arbitrary fitting parameters and can provide insight into what we would expect a material would produce in experimental output. This provides the ability to not only verify with experiment, but also validate generated DFT material properties as shown in Chapter 3. Yet there is always deeper understanding that we can pursue! One future step would be to expand the analysis of the thermal interface problem beyond that of just a sinusoidal thermal grating, but with nanofabricated pillars [27,29]. These nanofabricated structures have allowed for experimental geometries that are much shorter than the table-top TTG capabilities of 1 micron.

For the analysis of the TTG, recent experiments with the FEL in the Elettra Sincrotrone facilities in Trieste, Italy are pushing the lowest thermal gratings possible. This will allow the ability to observe nondiffusive transport in materials with much shorter MFP as the grating periods with extreme UV light is much shorter, on the order of hundreds of nanometers. In fact, recent experiments 280 nm are shown in Fig. 7-1, demonstrating the success of the variational framework in predicting the experimental temperature decay for silicon.

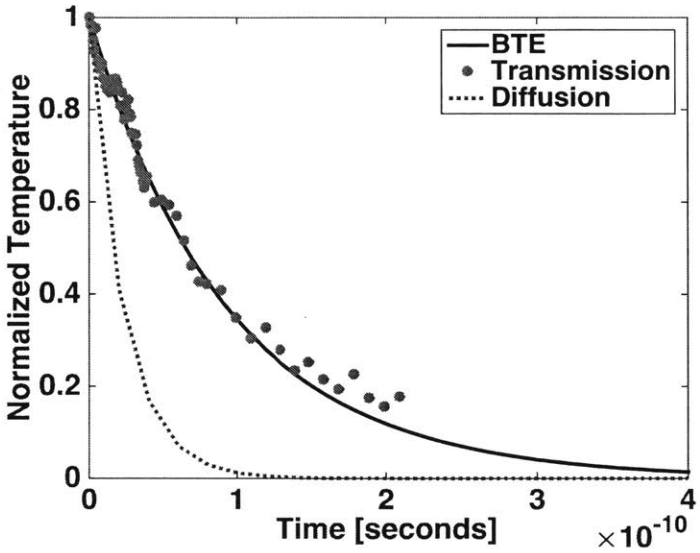

FIG. 7-1. EUV temperature decay of TTG. The decay of a 280 nm thermal grating is observed with excellent agreement with the variational approach in solving the BTE. The effective thermal conductivity is nearly 25% that of bulk, demonstrating a marked difference compared to that of the bulk silicon thermal decay.

Furthermore, some theoretical next steps include expanding the solutions for the BTE beyond some of the assumptions of this formalism. Recently, the ability to understanding thermal transport and scattering in materials such as graphite and diamond are possible with the full scattering matrix included in the BTE [57,60]. The full scattering matrix included in the BTE makes the system much harder to solve as compared to the simplification of the RTA, but is a necessary step to study nondiffusive thermal transport in materials for which the RTA is a poor approximation.

Lastly, the possibility of achieving thermal transport that is enhanced compared to the prediction of the Fourier heat conduction equation by controlling the phonon source distribution is quite exciting. As size effects have only been known to reduce the thermal conductivity of a material in the nano/micro scale, the ability to enhance the thermal transport will have strong implications for microelectronics cooling. Further work to be able to design an experiment in which this effect can be directly observed will be critical in order to take these theoretical

predictions to a practical level, especially in considering the thermal management of processors in electronic devices.

References

[1] Schelling, P. K., Shi, L., and Goodson, K. E., 2005, "Managing Heat for Electronics," Mater. Today, **8**(6), pp. 30–35.

[2] Cahill, D. G., Braun, P. V., Chen, G., Clarke, D. R., Fan, S., Goodson, K. E., Keblinski, P., King, W. P., Mahan, G. D., Majumdar, A., Maris, H. J., Phillpot, S. R., Pop, E., and Shi, L., 2014, "Nanoscale Thermal Transport. II. 2003–2012," Appl. Phys. Rev., **1**(1), p. 11305.

[3] Zebarjadi, M., Esfarjani, K., Dresselhaus, M. S., Ren, Z. F., and Chen, G., 2012, "Perspectives on Thermoelectrics: From Fundamentals to Device Applications," Energy Environ. Sci., **5**(1), pp. 5147–5162.

[4] Minnich, A. J., Dresselhaus, M. S., Ren, Z. F., and Chen, G., 2009, "Bulk Nanostructured Thermoelectric Materials: Current Research and Future Prospects," Energy Environ. Sci., **2**(5), p. 466.

[5] Majumdar, A., 1993, "Microscale Heat Conduction in Dielectric Thin Films," J. Heat Transfer, **115**(1), p. 7.

[6] Dames, C., and Chen, G., 2005, *Thermal Conductivity of Nanostructured Thermoelectric Materials*, CRC Press, Boca Raton.

[7] Volz, S. G., and Chen, G., 1999, "Molecular Dynamics Simulation of Thermal Conductivity of Silicon Nanowires," Appl. Phys. Lett., **75**(14), pp. 2056–2058.

[8] Li, D., Wu, Y., Kim, P., Shi, L., Yang, P., and Majumdar, A., 2003, "Thermal Conductivity of Individual Silicon Nanowires," Appl. Phys. Lett., **83**(14), pp. 2934–2936.

[9] Guyer, R. A., and Krumhansl, J. A., 1966, "Thermal Conductivity, Second Sound, and Phonon Hydrodynamic Phenomena in Nonmetallic Crystals," Phys. Rev., **148**(2), pp. 778–788.

[10] Ju, Y. S., and Goodson, K. E., 1999, "Phonon Scattering in Silicon Films with Thickness of Order 100 Nm," Appl. Phys. Lett., **74**(20), pp. 3005–3007.

[11] Asheghi, M., Kurabayashi, K., Kasnavi, R., and Goodson, K. E., 2002, "Thermal Conduction in Doped Single-Crystal Silicon Films," J. Appl. Phys., **91**(8), pp. 5079–5088.

[12] Asheghi, M., Touzelbaev, M. N., Goodson, K. E., Leung, Y. K., and Wong, S. S., 1998, "Temperature-Dependent Thermal Conductivity of Single-Crystal Silicon Layers in SOI

Substrates," J. Heat Transfer, **120**(1), p. 30.

[13] Liu, W., and Asheghi, M., 2004, "Phonon–boundary Scattering in Ultrathin Single-Crystal Silicon Layers," Appl. Phys. Lett., **84**(19), pp. 3819–3821.

[14] Mazumder, S., and Majumdar, A., 2001, "Monte Carlo Study of Phonon Transport in Solid Thin Films Including Dispersion and Polarization," J. Heat Transfer, **123**(4), p. 749.

[15] Goodson, K. E., 1996, "Thermal Conduction in Nonhomogeneous CVD Diamond Layers in Electronic Microstructures," J. Heat Transfer, **118**(2), p. 279.

[16] Johnson, J. A., Maznev, A. A., Cuffe, J., Eliason, J. K., Minnich, A. J., Kehoe, T., Torres, C. M. S., Chen, G., and Nelson, K. A., 2013, "Direct Measurement of Room-Temperature Nondiffusive Thermal Transport Over Micron Distances in a Silicon Membrane," Phys. Rev. Lett., **110**(2), p. 25901.

[17] Cuffe, J., Eliason, J. K., Maznev, A. A., Collins, K. C., Johnson, J. A., Shchepetov, A., Prunnila, M., Ahopelto, J., Sotomayor Torres, C. M., Chen, G., and Nelson, K. A., 2015, "Reconstructing Phonon Mean-Free-Path Contributions to Thermal Conductivity Using Nanoscale Membranes," Phys. Rev. B, **91**(24), p. 245423.

[18] Maznev, A. A., Johnson, J. A., and Nelson, K. A., 2011, "Onset of Nondiffusive Phonon Transport in Transient Thermal Grating Decay," Phys. Rev. B, **84**(19), p. 195206.

[19] Johnson, J. A., Eliason, J. K., Maznev, A. A., Luo, T., and Nelson, K. A., 2015, "Non-Diffusive Thermal Transport in GaAs at Micron Length Scales," J. Appl. Phys., **118**(15), p. 155104.

[20] Zeng, L., Chiloyan, V., Huberman, S., Maznev, A. A. A., Peraud, J.-P. M. J.-P. M., Hadjiconstantinou, N. G. N. G., Nelson, K. A. K. A., and Chen, G., 2016, "Monte Carlo Study of Non-Diffusive Relaxation of a Transient Thermal Grating in Thin Membranes," Appl. Phys. Lett., **108**(6), p. 63107.

[21] Young, D. A., Thomsen, C., Grahn, H. T., Maris, H. J., and Tauc, J., 1986, "Heat Flow in Glasses on a Picosecond Timescale," Springer, Berlin, Heidelberg, pp. 49–51.

[22] Cahill, D. G., Ford, W. K., Goodson, K. E., Mahan, G. D., Majumdar, A., Maris, H. J., Merlin, R., and Phillpot, S. R., 2003, "Nanoscale Thermal Transport," J. Appl. Phys., **93**(2), p. 793.

[23] Paddock, C. A., and Eesley, G. L., 1986, "Transient Thermoreflectance from Thin Metal Films," J. Appl. Phys., **60**(1), pp. 285–290.

[24] Collins, K. C., Maznev, A. A., Cuffe, J., Nelson, K. A., and Chen, G., 2014, "Examining Thermal Transport through a Frequency-Domain Representation of Time-Domain Thermoreflectance Data.," Rev. Sci. Instrum., **85**(12), p. 124903.

[25] Cahill, D. G., 2004, "Analysis of Heat Flow in Layered Structures for Time-Domain Thermoreflectance," Rev. Sci. Instrum., **75**(12), pp. 5119–5122.

[26] Zeng, L., and Chen, G., 2014, "Disparate Quasiballistic Heat Conduction Regimes from Periodic Heat Sources on a Substrate," J. Appl. Phys., **116**(6), p. 64307.

[27] Hu, Y., Zeng, L., Minnich, A. J., Dresselhaus, M. S., and Chen, G., 2015, "Spectral Mapping of Thermal Conductivity through Nanoscale Ballistic Transport.," Nat. Nanotechnol., **10**(8), pp. 701–6.

[28] Hoogeboom-Pot, K. M., Hernandez-Charpak, J. N., Gu, X., Frazer, T. D., Anderson, E. H., Chao, W., Falcone, R. W., Yang, R., Murnane, M. M., Kapteyn, H. C., and Nardi, D., 2015, "A New Regime of Nanoscale Thermal Transport: Collective Diffusion Increases Dissipation Efficiency," Proc. Natl. Acad. Sci., **112**(16), pp. 4846–4851.

[29] Zeng, L., Collins, K. C. K. C., Hu, Y., Luckyanova, M. N. M. N., Maznev, A. A. A. A., Huberman, S., Chiloyan, V., Zhou, J., Huang, X., Nelson, K. A. K. A., and Chen, G., 2015, "Measuring Phonon Mean Free Path Distributions by Probing Quasiballistic Phonon Transport in Grating Nanostructures.," Sci. Rep., **5**, p. 17131.

[30] Regner, K. T., Majumdar, S., and Malen, J. A., 2013, "Instrumentation of Broadband Frequency Domain Thermoreflectance for Measuring Thermal Conductivity Accumulation Functions.," Rev. Sci. Instrum., **84**(6), p. 64901.

[31] Regner, K. T., Sellan, D. P., Su, Z., Amon, C. H., McGaughey, A. J. H., and Malen, J. A., 2013, "Broadband Phonon Mean Free Path Contributions to Thermal Conductivity Measured Using Frequency Domain Thermoreflectance.," Nat. Commun., **4**, p. 1640.

[32] Koh, Y., and Cahill, D., 2007, "Frequency Dependence of the Thermal Conductivity of Semiconductor Alloys," Phys. Rev. B, **76**(7), p. 75207.

[33] Minnich, A. J., Chen, G., Mansoor, S., and Yilbas, B. S., 2011, "Quasiballistic Heat Transfer Studied Using the Frequency-Dependent Boltzmann Transport Equation," Phys. Rev. B, **84**(23), p. 235207.

[34] Ziman, J., 1960, *Electrons and Phonons: The Theory of Transport Phenomena in Solids (Oxford Classic Texts in the Physical Sciences)*, Oxford University Press, London.

[35] Henry, A. S., and Chen, G., 2008, "Spectral Phonon Transport Properties of Silicon Based on Molecular Dynamics Simulations and Lattice Dynamics," J. Comput. Theor. Nanosci., **5**(12), pp. 141–152.

[36] Yang, F., and Dames, C., 2013, "Mean Free Path Spectra as a Tool to Understand Thermal Conductivity in Bulk and Nanostructures," Phys. Rev. B, **87**(3), p. 35437.

[37] Minnich, A. J., 2012, "Determining Phonon Mean Free Paths from Observations of Quasiballistic Thermal Transport," Phys. Rev. Lett., **109**(20), p. 205901.

[38] Chen, G., 2005, *Nanoscale Energy Transport and Conversion: A Parallel Treatment of Electrons, Molecules, Phonons, and Photons: A Parallel Treatment of Electrons, Molecules, Phonons, and Photons*, Oxford University Press, New York.

[39] Chen, G., 1996, "Nonlocal and Nonequilibrium Heat Conduction in the Vicinity of Nanoparticles," J. Heat Transfer, **118**(3), p. 539.

[40] Esfarjani, K., and Stokes, H. T., 2008, "Method to Extract Anharmonic Force Constants from First Principles Calculations," Phys. Rev. B, **77**(14), p. 144112.

[41] Esfarjani, K., Chen, G., and Stokes, H. T., 2011, "Heat Transport in Silicon from First-Principles Calculations," Phys. Rev. B, **84**(8), p. 85204.

[42] Fuchs, K., and Mott, N. F., 2008, "The Conductivity of Thin Metallic Films according to the Electron Theory of Metals," Math. Proc. Cambridge Philos. Soc., **34**(1), p. 100.

[43] Sondheimer, E. H., 1952, "The Mean Free Path of Electrons in Metals," Adv. Phys., **1**(1), pp. 1–42.

[44] Regner, K. T., McGaughey, A. J. H., and Malen, J. A., 2014, "Analytical Interpretation of Nondiffusive Phonon Transport in Thermoreflectance Thermal Conductivity Measurements," Phys. Rev. B, **90**(6), p. 64302.

[45] Hua, C., and Minnich, A. J., 2015, "Semi-Analytical Solution to the Frequency-Dependent Boltzmann Transport Equation for Cross-Plane Heat Conduction in Thin Films," J. Appl. Phys., **117**(17), p. 175306.

[46] Minnich, A. J., 2015, "Multidimensional Quasiballistic Thermal Transport in Transient Grating Spectroscopy," Phys. Rev. B, **92**(8), p. 85203.

[47] Hua, C., and Minnich, A. J., 2014, "Analytical Green's Function of the Multidimensional Frequency-Dependent Phonon Boltzmann Equation," Phys. Rev. B, **90**(21), p. 214306.

[48] Hua, C., and Minnich, A. J., 2014, "Transport Regimes in Quasiballistic Heat

Conduction," Phys. Rev. B, **89**(9), p. 94302.

[49] Yang, F., and Dames, C., 2015, "Heating-Frequency-Dependent Thermal Conductivity: An Analytical Solution from Diffusive to Ballistic Regime and Its Relevance to Phonon Scattering Measurements," Phys. Rev. B, **91**(16), p. 165311.

[50] Péraud, J.-P. M., and Hadjiconstantinou, N. G., 2011, "Efficient Simulation of Multidimensional Phonon Transport Using Energy-Based Variance-Reduced Monte Carlo Formulations," Phys. Rev. B, **84**(20), p. 205331.

[51] Péraud, J.-P. M., and Hadjiconstantinou, N. G., 2012, "An Alternative Approach to Efficient Simulation of Micro/nanoscale Phonon Transport," Appl. Phys. Lett., **101**(15), p. 153114.

[52] Collins, K. C., Maznev, A. A., Tian, Z., Esfarjani, K., Nelson, K. A., and Chen, G., 2013, "Non-Diffusive Relaxation of a Transient Thermal Grating Analyzed with the Boltzmann Transport Equation," J. Appl. Phys., **114**(10), p. 104302.

[53] Ravichandran, N. K., and Minnich, A. J., 2016, "Role of Thermalizing and Nonthermalizing Walls in Phonon Heat Conduction along Thin Films," Phys. Rev. B, **93**(3), p. 35314.

[54] Forghani, M., Hadjiconstantinou, N. G., and Péraud, J.-P. M., 2016, "Reconstruction of the Phonon Relaxation Times Using Solutions of the Boltzmann Transport Equation," Phys. Rev. B, **94**(15), p. 155439.

[55] Peraud, J.-P. M., Landon, C. D., and Hadjiconstantinou, N. G., 2014, "Monte Carlo Methods for Solving the Boltzmann Transport Equation," Annu. Rev. Heat Transf., **17**(N/A), pp. 205–265.

[56] Kittel, C., 2004, *Introduction to Solid State Physics*, Wiley.

[57] Cepellotti, A., and Marzari, N., 2016, "Thermal Transport in Crystals as a Kinetic Theory of Relaxons," Phys. Rev. X, **6**(4), p. 41013.

[58] Allen, P. B., 2013, "Improved Callaway Model for Lattice Thermal Conductivity," Phys. Rev. B, **88**(14), p. 144302.

[59] Krumhansl, J. A., 1965, "Thermal Conductivity of Insulating Crystals in the Presence of Normal Processes," Proc. Phys. Soc., **85**(5), p. 921.

[60] Cepellotti, A., and Marzari, N., 2016, "Transport Waves as Crystal Excitations," arXiv:1612.04317.

[61] Ward, A., and Broido, D. A., 2010, "Intrinsic Phonon Relaxation Times from First-Principles Studies of the Thermal Conductivities of Si and Ge," Phys. Rev. B, **81**(8), p. 85205.

[62] Broido, D. A., Malorny, M., Birner, G., Mingo, N., and Stewart, D. A., 2007, "Intrinsic Lattice Thermal Conductivity of Semiconductors from First Principles," Appl. Phys. Lett., **91**(23), p. 231922.

[63] Esfarjani, K., Chen, G., and Stokes, H. T., 2011, "Heat Transport in Silicon from First Principles Calculations," Phys. Rev. B, **84**(8), pp. 1–11.

[64] Chiloyan, V., Zeng, L., Huberman, S., Maznev, A. A., Nelson, K. A., and Chen, G., 2016, "Variational Approach to Extracting the Phonon Mean Free Path Distribution from the Spectral Boltzmann Transport Equation," Phys. Rev. B, **93**(15), p. 155201.

[65] Chiloyan, V., Zeng, L., Huberman, S., Maznev, A. A., Nelson, K. A., and Chen, G., 2016, "Variational Approach to Solving the Spectral Boltzmann Transport Equation in Transient Thermal Grating for Thin Films," J. Appl. Phys., **120**(2), p. 25103.

[66] Sakurai, J., 1993, *Modern Quantum Mechanics*, Addison Wesley, New York.

[67] Griffiths, D. J., 2005, *Introduction to Quantum Mechanics*, Pearson Education, Upper Saddle River, NJ.

[68] Allen, P. B., 2013, "Heat Conduction by Phonons across a Film," arXiv:1308.2890.

[69] Ah-Sam, L. E. G., Jensen, H. H., and Smith, H., 1971, "On the Use of Variational Methods for Solving Boltzmann Equations Involving Non-Hermitian Operators," J. Stat. Phys., **3**(1), pp. 17–34.

[70] Hindley, N. K., and Garcia-Moliner, F., 1965, "Variational Treatment of High-Frequency Transport Problems in Solids," Phys. Rev., **140**(1A), pp. A343–A352.

[71] Abramowitz, M., and Stegun, I., 1972, *Handbook of Mathematical Functions with Formulas, Graphs, and Mathematical Tables*, Dover, New York.

[72] Johnson, J. A., Maznev, A. A., Bulsara, M. T., Fitzgerald, E. A., Harman, T. C., Calawa, S., Vineis, C. J., Turner, G., and Nelson, K. A., 2012, "Phase-Controlled, Heterodyne Laser-Induced Transient Grating Measurements of Thermal Transport Properties in Opaque Material," J. Appl. Phys., **111**(2), p. 23503.

[73] Huberman, S., Chiloyan, V., Duncan, R. A., Zeng, L., Jia, R., Maznev, A. A., Fitzgerald, E. A., Nelson, K. A., and Chen, G., 2017, "Unifying First-Principles Theoretical

Predictions and Experimental Measurements of Size Effects in Thermal Transport in SiGe Alloys," Phys. Rev. Mater., **1**(5), p. 54601.

[74] Ohno, K., Esfarjani, K., and Kawazoe, Y., 1999, *Computational Materials Science: From Ab Initio to Monte Carlo Methods*, Springer Science & Business Media.

[75] Ashcroft, N., and Mermin, D., 1976, *Solid State Physics*, Thomson Learning.

[76] Wilson, R. B., and Cahill, D. G., 2014, "Anisotropic Failure of Fourier Theory in Time-Domain Thermoreflectance Experiments," Nat Commun, **5**, p. 5075.

[77] Bencivenga, F., Cucini, R., Capotondi, F., Battistoni, A., Mincigrucci, R., Giangrisostomi, E., Gessini, A., Manfredda, M., Nikolov, I. P., Pedersoli, E., Principi, E., Svetina, C., Parisse, P., Casolari, F., Danailov, M. B., Kiskinova, M., and Masciovecchio, C., 2015, "Four-Wave Mixing Experiments with Extreme Ultraviolet Transient Gratings.," Nature, **520**(7546), pp. 205–8.

[78] Bencivenga, F., Calvi, A., Capotondi, F., Cucini, R., Mincigrucci, R., Simoncig, A., Manfredda, M., Pedersoli, E., Principi, E., Dallari, F., Duncan, R. A., Izzo, M. G., Knopp, G., Maznev, A. A., Monaco, G., Di Mitri, S., Gessini, A., Giannessi, L., Mahne, N., Nikolov, I. P., Passuello, R., Raimondi, L., Zangrando, M., and Masciovecchio, C., 2016, "Four-Wave-Mixing Experiments with Seeded Free Electron Lasers," Faraday Discuss., **194**(0), pp. 283–303.

[79] Pop, E., 2010, "Energy Dissipation and Transport in Nanoscale Devices," Nano Res., **3**(3), pp. 147–169.

[80] Tonapi, S. S., Fillion, R. A., Schattenmann, F. J., Cole, H. S., Evans, J. D., and Sammakia, B. G., "An Overview of Thermal Management for next Generation Microelectronic Devices," *Advanced Semiconductor Manufacturing Conference and Workshop, 2003 IEEEI/SEMI*, IEEE, pp. 250–254.

[81] Cahill, D. G., Goodson, K., and Majumdar, A., 2002, "Thermometry and Thermal Transport in Micro/Nanoscale Solid-State Devices and Structures," J. Heat Transfer, **124**(2), pp. 223–241.

[82] Liu, J., Zhu, J., Tian, M., Gu, X., Schmidt, A., and Yang, R., 2013, "Simultaneous Measurement of Thermal Conductivity and Heat Capacity of Bulk and Thin Film Materials Using Frequency-Dependent Transient Thermoreflectance Method," Rev. Sci. Instrum., **84**(3), p. 34902.

[83] Collins, K. C. (Kimberlee C., 2015, "Studies of Non-Diffusive Heat Conduction through Spatially Periodic and Time-Harmonic Thermal Excitations," Massachusetts Institute of Technology.

[84] Hua, C., Chen, X., Ravichandran, N. K., and Minnich, A. J., 2017, "Experimental Metrology to Obtain Thermal Phonon Transmission Coefficients at Solid Interfaces," Phys. Rev. B, **95**(20), p. 205423.

[85] Schmidt, A. J., Cheaito, R., and Chiesa, M., 2009, "A Frequency-Domain Thermoreflectance Method for the Characterization of Thermal Properties.," Rev. Sci. Instrum., **80**(9), p. 94901.

[86] Jain, A., and McGaughey, A. J. H., 2016, "Thermal Transport by Phonons and Electrons in Aluminum, Silver, and Gold from First Principles," Phys. Rev. B, **93**(8), p. 81206.

[87] Shi, L., Dames, C., Lukes, J. R., Reddy, P., Duda, J., Cahill, D. G., Lee, J., Marconnet, A., Goodson, K. E., Bahk, J.-H., Shakouri, A., Prasher, R. S., Felts, J., King, W. P., Han, B., and Bischof, J. C., 2015, "Evaluating Broader Impacts of Nanoscale Thermal Transport Research," Nanoscale Microscale Thermophys. Eng., **19**(2).

[88] Liao, B., Qiu, B., Zhou, J., Huberman, S., Esfarjani, K., and Chen, G., 2015, "Significant Reduction of Lattice Thermal Conductivity by the Electron-Phonon Interaction in Silicon with High Carrier Concentrations: A First-Principles Study," Phys. Rev. Lett., **114**(11), p. 115901.